Experimental Investigation of Turbulent Channel Flow Over Superhydrophobic Surfaces

by

Wagih Abu Rowin

A thesis submitted in partial fulfillment of the requirements for the degree of

Doctor of Philosophy

Department of Mechanical Engineering
University of Alberta

Abstract

A reduction in skin-friction drag can lead to lower energy consumption in variety of transportation vehicles, and consequently results in a smaller environmental impact. Several methods have been presented to reduce the skin-fiction and one of these methods is to introduce an air layer at the solid-liquid interface. A technique to introduce this air layer is to use a superhydrophobic surface (SHS), which consists of nano/micro structures covered with a thin layer of water-repellent coating. As a result of the trapped air pockets, a boundary condition is formed where the liquid flow can partially slip, relaxing the no-slip boundary condition of solid surfaces. This research begins by advancing the current understanding of skin-friction reduction over the SHSs. For this purpose, measurements of the slip velocity and its effect on the turbulent structures are performed. This thesis then identifies the effect of several parameters, including Reynolds number, hydrostatic pressure, and surface roughness, on the SHSs performance.

The inner and outer layers of a turbulent channel flow over an SHS were first characterized using simultaneous long-range microscopic particle tracking velocimetry (micro-PTV) and particle image velocimetry (PIV), respectively. The micro-PTV showed larger mean streamwise velocity at the SHS, indicating the existence of slip velocity at the wall. The quadrant analysis of turbulent fluctuations showed attenuation of stronger sweep motions near the wall, while ejections were attenuated in the buffer layer.

Three-dimensional lagrangian PTV was also used to study the near-wall turbulent flow over an SHS. The measurements confirmed an isotropic slip (comparable streamwise and spanwise effective slip length) over an SHS with low surface roughness. When Reynolds stresses over the SHS are normalized by the inner scaling of the smooth surface, large

streamwise and spanwise Reynolds stresses were observed near the wall compared with that over the no-slip surface. The wall-normal Reynolds stress over the SHS and no-slip surface were comparable near the wall. A small increase of Reynolds shear stress of the SHS was also seen at the wall relative to that of the no-slip surface. Away from the wall, all components of Reynolds stresses over the SHS were smaller than those over the no-slip surface. When normalized by the corresponding inner scaling, the near-wall Reynolds stresses over the SHS were larger and shifted towards the wall.

The effect of Reynolds number (Re) on the slip boundary condition and the near-wall turbulence statistics over an SHS was also investigated. It was observed that the slip velocity over the SHS increases linearly with increasing Re, while the effective slip length reduces. The latter was associated with an increase of test-section pressure, which enhanced the solubility of air in the water and reduced the plastron thickness. The difference between Reynolds stresses over the no-slip surface, and the SHS, increased with increasing Re.

Finally, the effects of SHS roughness was investigated in a turbulent channel flow at a constant flow rate. The results showed that slip velocity over the SHSs increased with increasing SHSs roughness. The effective slip length followed the trend of larger effective slip length for larger surface roughness. The increase of the SHS roughness increased streamwise, spanwise, and shear Reynolds stresses in the vicinity of the wall. The drag reduction over the SHS increased linearly with increasing the surface roughness. It was also found that the increase of the surface roughness has a larger effect on the slip velocity than on the Reynolds shear stress.

Preface

Chapter 5 has been published in the *Physics of Fluids* and reproduced from [*W.* Abu Rowin, J. Hou, and S. Ghaemi. Inner and outer layer turbulence over a superhydrophobic surface with low roughness level at low Reynolds number. Physics of Fluids, 29(9):095106, 2017.], with the permission of AIP Publishing.

Chapter 6 has been published in the *Journal of Fluid Mechanics* and reproduced from [*W.* Abu Rowin and S. Ghaemi. Streamwise and spanwise slip over a superhydrophobic surface. Journal of Fluid Mechanics, 870:1127–1157, 2019], with the permission of the copyright holder.

Chapter 7 has been submitted to the *Experiments in Fluids*

Chapter 8 has not been submitted to a journal for peer-review; however the author expects to submit it later this year. The superhydrophobic surfaces used in this chapter were fabricated at the University of Texas at Dallas by Abhijeet Singh and Venkata Pillutla under the supervision of Dr. Wonjae Choi.

All of the experiments, data analysis, and interpretation for these papers are conceived by the author under the supervision of Dr. Sina Ghaemi.

Dedicated to my family

Acknowledgements

Foremost, I would like to express my deepest gratitude and appreciation to my advisor Dr. Sina Ghaemi for the patient guidance, mentorship, and support over the years.

I am forever thankful for my parents for their constant care and consideration, and my wife Salma, who has been a constant support and strength through all of life's adventures.

I would like to thank my friends/colleagues Sadek Shaban, Jianfeng Hou, Daren Wilkinson, and Masoud Ebrahimian who supported me through this research. I am also thankful for the unconditional help from the members in my research group who provided guidance throughout my research.

Contents

List of Tables

List of Figures

List of Nomenclature

Abbreviations

2D-PTV	two-dimensional particle tracking velocimetry
3D-PTV	three-dimensional particle tracking velocimetry
CCD	charge-coupled device
CMOS	complementary metal oxide semiconductor
DHM	digital holographic microscopy
DI	drag increase
DNS	direct numerical simulation
DOF	depth of field
DR	drag reduction
EOC	ensemble of correlations
FOV	field of view
IPR	iterative particle reconstruction
IW	interrogation window
LDS	linear spectral density
MART	multiplicative algebraic reconstruction technique
micro-PTV	microscopic particle tracking velocimetry
OTF	optical transfer function
PDF	probability density function

PIV	particle image velocimetry
PTFE	polytetrafluoroethylene
PTV	particle tracking velocimetry
SHS	superhydrophobic surface
STB	shake-the-box

Greek Letters

κ	von Kármán constant
λ	wall unit
μ	fluid dynamic viscosity
ν	fluid kinematic viscosity
ρ	fluid density
ρ_T	tracers density
τ_e	characteristic time of energy containing eddies
τ_R	Reynolds shear stress
τ_T	tracer response time
τ_t	total shear stress
τ_v	viscous shear stress
τ_w	wall shear stress
ε	difference between the weighted integrals of Reynolds shear stress over the smooth and SHS

Superscripts

$^+$	normalized by the corresponding inner scaling
$^-$(overbar)	averaged quantity

Symbols

Δt	laser pulse separation

$\langle u_i u_j \rangle$	Reynolds stresses
$\langle u^2 \rangle$	streamwise Reynolds stress
$\langle uv \rangle$	Reynolds shear stress
$\langle v^2 \rangle$	wall-normal Reynolds stress
$\langle w^2 \rangle$	spanwise Reynolds stress
a	acceleration
B	intercept of the logarithmic profile
c	sensitivity coefficient
C_f	skin-friction coefficient
d_t	tracer diameter
f	frequency
f_N	Nyquist frequency
H	channel height
I	the weighted integrals of Reynolds shear stress
I_{max}	intensity peak
k	root-mean-square of surface roughness
L	channel length
l_s	effective slip length
l_x	streamwise effective slip length
l_z	spanwise effective slip length
N	total number of data points
n	number of data points
P_a	static pressure inside the test section
R	surface roughness
Re	Reynolds number

Re_τ	friction Reynolds number
S	surface profile in the wall-normal direction
S_l	surface length
St	Stokes number
t_k	kernel size of the polynomial filter
U_b	bulk channel velocity
U_s	streamwise slip velocity
u_τ	friction velocity
U_{max}	maximum velocity
W_s	spanwise slip velocity
Wi	channel width
x	cartesian coordinate for the streamwise direction
y	cartesian coordinate for the wall-normal direction; wall-normal distance
z	cartesian coordinate for the spanwise direction

Subscripts

0	normalized by the inner scaling of the no-slip surface
b	normalized by the bulk velocity
rms	root-mean-square component
s	slip component at the wall

Chapter 1

Introduction

1.1 Motivation

The increase in the use of transportation systems is leading to concerning levels of energy consumption. For instance, imports to Canada increase 1.5% every month reaching a record of 470 million tons of goods in 2017 (International Trade Administration, 2017; Trading Economics, 2019). Most of these goods are transported through the ocean using water-borne transportation. In the transportation systems, skin-friction force is one of the primary components of resistance to the motion of a solid in a fluid. Therefore, the scientific community focuses on developing efficient systems to reduce skin-friction and lower energy consumption. Various control methods to reduce the skin-friction have been proposed over the years. The flow control methods have been classified into two categories: active and passive (Gad-el Hak, 2000).

Active control methods require an external source of energy to operate a series of actuators and sensors. In the last few decades, numerical simulations and laboratory experiments have shown that active control methods are effective in reducing skin-friction; however, these methods remain impractical in real applications due to technical challenges such as the difficulty of oscillating an entire body or installing a dense array of actuators (Choi et al., 2008). Passive control methods, on the other hand, require no external energy. These methods work through modifying the surface structure or the fluid properties. The former includes riblets and permeable surfaces and the latter includes polymer additives and bubble injec-

tion. Introducing a shear free boundary condition at the wall has recently become a topic of interest due to its potential in reducing the skin-friction, and a superhydrophobic surface is one of these techniques to introduce this slip.

The recent developments in microfabrication processes have made it possible to manufacture superhydrophobic surfaces as a passive technique for reducing skin friction. Initial studies have confirmed the existence of significant skin-friction reduction using the superhydrophobic surfaces (Rothstein, 2010). The combination of chemical hydrophobicity and surface texture of a superhydrophobic surface can trap small air pockets (i.e., a plastron) in micro- and nano-scale pores when submerged in water. The existence of the air-layer introduces a new interface with the liquid known as the air-water interface. The air-water interface relaxes the no-slip boundary condition by reducing the contact area between the liquid and the solid substrate. As a result, the liquid flow appears to "slip" over the superhydrophobic surface with the potential of reducing skin-friction drag (Rothstein, 2010). Solid surfaces exhibiting the slip boundary condition, if applicable in turbulent flows, can potentially reduce skin-friction drag in the transportation industry.

Experiments in controlled laboratory conditions have shown up to 75% drag reduction over the superhydrophobic surface in turbulent wall flows (Park et al. 2014), nevertheless the mechanism of drag reduction of superhydrophobic surfaces is still unclear. Measurement of the slip velocity and its effect on the mean velocity and turbulence structures were not reported since most of the previous laboratory observations on SHSs in turbulent flow (Daniello et al., 2009; Woolford et al., 2009a; Zhang et al., 2015; Vajdi Hokmabad and Ghaemi, 2016) have been mostly carried out in the outer layer. To the author's best of knowledge, Ling et al. (2016) was the only experiment that studied the inner layer of a turbulent boundary layer over large roughness superhydrophobic surfaces. Moreover, in turbulent flows, laboratory investigations over superhydrophobic surfaces have demonstrated scattered results (different values of drag reduction and occasional drag increases).

This thesis aims to advance our understanding of the mechanism of skin-friction reduction using low roughness superhydrophobic surfaces. For this purpose, the role of the slip

velocity over the superhydrophobic surfaces in reducing the skin-friction and modifying the turbulent structures in channel flows is experimentally scrutinized. This thesis also aims to provide practical guidelines required for the development of superhydrophobic surfaces for use in turbulent flows. These guidelines include the effect of pressure on the superhydrophobic surface performance, the impact of free-stream velocity on the superhydrophobic surface performance, and the optimum surface roughness that can provide the highest skin-friction reduction.

1.2 Thesis Overview

This thesis includes 9 chapters and an appendix. Chapter 5, 6, 7, and 8 include literature review and discussion necessary to drive the motivations of each chapter. The thesis is organized as following:

Chapter 2 provides essential background information and basic concepts about the slip boundary condition over the superhydrophobic surface. This chapter also includes a literature review to summarize and discuss the reduction of skin-friction by superhydrophobic surfaces.

Chapter 3 provides details of the experimental setup, including the flow facilities and superhydrophobic surfaces fabrication processes and characterization methods.

Chapter 4 describes the measurement techniques used in this thesis including planer particle tracking velocimetry, long-range microscopic particle tracking velocimetry, time-resolved three-dimensional particle tracking velocimetry, time-resolved two-dimensional particle tracking velocimetry, and pressure drop measurement. The chapter also evaluates the uncertainty of the measurements.

Chapter 5 examines the effect of a low roughness randomly textured superhydrophobic surface on the mean velocity and Reynolds stresses of turbulent channel flow. The streamwise slip velocity and length are also measured in this chapter.

Chapter 6 advances the understanding of the effect of the superhydrophobic surface on the two wall parallel directions (streamwise and spanwise) of turbulent channel flow. The

streamwise and spanwise slip velocity and all components of Reynolds stresses are studied in this chapter.

Chapter 7 investigates the impact of the change of Reynolds number on the superhydrophobic surface performance. The change of the skin-friction, slip velocity, and Reynolds stresses over the superhydrophobic surface are studied versus Reynolds number.

Chapter 8 studies the effect of the superhydrophobic surface roughness on the effective slip over the superhydrophobic surface. Measurement of the reduction of the skin-friction is also included as a function of the surface roughness.

Chapter 9 summarizes the conclusion of present thesis and states its contributions. The chapter is concluded with a discussion of future work.

Appendix A shows the front panel of the developed LabView program and appendix B shows the block diagram for the LabView program.

Chapter 2

Background

Fluid flow has different characteristics depending on whether the fluid is flowing over a surface (external flow) or is enclosed by solid walls (internal flow). Examples of the external flow are: flow over a flat plate or an open channel, and examples of the internal flows are: flow through pipes or channels. For external flows, the boundary layer (the distance away from the wall at which the velocity component becomes parallel to the wall) will increase freely along the flow direction. In contrast, for internal flows, the boundary layers from the bounded solid walls grow and meet at the core of the bounded geometry. The current investigation focuses on internal flows, specifically channel flows. Most of the material included in this chapter is adopted from Bernard and Wallace (2002); Çencel and Cimbala (2006)

2.1 Turbulent Channel flow

A channel consists of two parallel long (L) and wide (Wi) plates separated by a small distance (H) relative to L and Wi. The coordinate system used here is defined as x, y, and z for the streamwise, wall-normal, and spanwise directions, respectively, as shown in Figure 2.1. The components of the instantaneous velocity vector are shown by U, V, and W and the components of the fluctuating velocity are shown by u, v, and w are in the $x-, y-$, and $z-$directions, respectively. The ensemble average of the velocity in time is denoted by $\overline{U}$. The flow is fully developed and independent of x when $L/H > 90$ (Coulson et al., 1999).

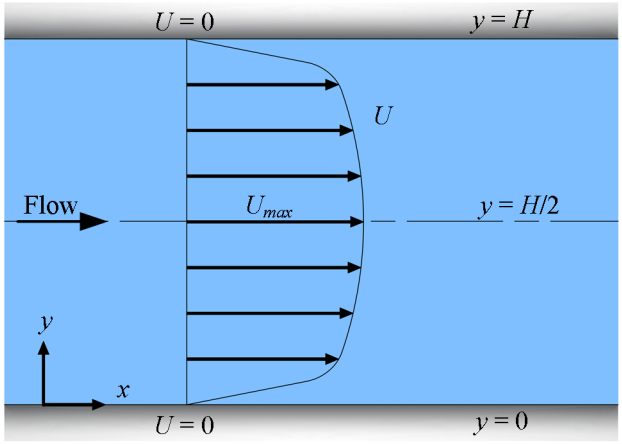

Figure 2.1: Schematic of flow travels in a two-dimensional fully developed channel flow.

The flow is also assumed to be two-dimensional when the width-to-height ratio (Wi/H) (i.e., aspect ratio) is larger than 7 as suggested by Dean (1978); Vinuesa et al. (2014). The flow regime (laminar or turbulent) in the channel flow is typically evaluated by Reynolds number (Re), which can be expressed as:

$$Re = \frac{\rho U_b H}{\mu}, \tag{2.1}$$

here ρ is the fluid density, U_b is the bulk velocity (i.e., the mean velocity), and μ is the fluid dynamic viscosity. Turbulent flow free of transitional effects occurs in channel flow at $Re > 3000$. Due to the no-slip boundary condition at a stationary solid surface, which will be discussed in more detail in Section 2.2 on page 10, the fluid velocity at $y = 0$ and $y = H$ is zero ($U = 0$) as shown in Figure 2.1. At the center of the channel ($y = H/2$) the fluid reaches the maximum velocity (U_{max}) .

2.1.1 Turbulent shear stress

It is found that near the wall, the total shear stress, τ_t, in the turbulent flow is much larger than the shear stress in the laminar flow, known as the viscous shear stress ($\tau_v = \mu\frac{\partial \overline{U}}{\partial y}$). In turbulent flow, swirling eddies cause significant fluctuations in velocity. The instantaneous value of the velocity fluctuations can be estimated from the difference between the instantaneous velocity, U, and $\overline{U}$. The shear stress due to the eddy motion of a fluid

particle is $\tau_R = -\rho\overline{uv}$. Here $\overline{uv}$ is the average of the velocity fluctuation and known as Reynolds shear stress. Thus, τ_t in the turbulent flow is the summation of τ_v and τ_R as shown in Figure 2.2a and can be expressed as

$$\tau_t = \tau_v + \tau_R, \text{or} \tag{2.2}$$

$$\tau_t = \mu\frac{\partial\overline{U}}{\partial y} - \rho\overline{uv}. \tag{2.3}$$

2.1.2 Velocity profile

The adjacent layers of moving fluid slow down close to a fixed solid boundary until reach a complete stop due to the no-slip boundary condition (see Section 2.2). As a result, a velocity gradient develops at the wall. The consequent velocity profile, in turbulent flow, is divided into four layers based on the distance from the wall as shown in Figure 2.2b. The first layer next to the wall, where the viscous effects are dominant, is known as the viscous or laminar sublayer. The following layer is called the buffer layer where the viscous effects are still dominant but the turbulent motion starts to appear. A transitional region which is known as the transition layer or the overlap layer exists where the turbulent effects are more dominant than the viscous effects. Beyond these layers is the outer layer where the effect of molecular viscosity is negligible.

The viscous sublayer is typically very small compared with the channel height, and it is observed to have a linear behavior. It is found that the velocity gradient, $\frac{\partial\overline{U}}{\partial y}$, in this region remains constant. Thus the viscous shear stress or wall shear stress, τ_w, can be expressed as follows

$$\tau_v = \tau_w = \mu\frac{\partial\overline{U}}{\partial y}. \tag{2.4}$$

Since the velocity gradient is constant in the vicinity of the wall, thus $\frac{\partial\overline{U}}{\partial y} = \frac{\overline{U}}{y}$. Then Equation 2.4 can be written as

$$\frac{\tau_w}{\rho} = \nu\frac{\overline{U}}{y}. \tag{2.5}$$

Here $\nu = \mu/\rho$ is the kinematic viscosity. The square-root of the left hand side of Equation 2.5 has the unit of velocity and is known by the friction velocity ($u_\tau = \sqrt{\tau_w/\rho}$).

By using the expression of u_τ, Equation 2.5 can be written as

$$u_\tau^2 = \nu \frac{\overline{U}}{y}, \text{or} \tag{2.6a}$$

$$\frac{\overline{U}}{u_\tau} = \frac{y u_\tau}{\nu}. \tag{2.6b}$$

The inverse of u_τ/ν in the right hand side of Equation 2.6b has a unit of length and is called the viscous length scale or the wall unit ($\lambda = \nu/u_\tau$). The parameters u_τ and λ are used in turbulent boundary layer studies to nondimensionalize the velocities and distance, respectively. In this thesis, the superscript '+' denotes parameters normalized using inner scaling, i.e., velocities are normalized by u_τ and the coordinate system is normalized by λ. Using this normalization, Equation 2.6b can be simplified as

$$u^+ = y^+. \tag{2.7}$$

Equation 2.7 is the law-of-the-wall where $u^+ = \overline{U}/u_\tau$ is the normalized velocity and $y^+ = y/\lambda$ is the normalized wall-normal distance. The law-of-the-wall is valid in the viscous sublayer at $y^+ < 3.5$.

In the overlap layer, viscous effects are insignificant and the velocity is a function of the large eddies. The velocity gradient can be written as

$$\frac{\partial \overline{U}}{\partial y} = f(y, \tau_w, \rho). \tag{2.8}$$

Using the dimensional analysis, the combination of τ_w and ρ will result in u_τ, then Equation 2.8 becomes

$$\frac{\partial \overline{U}}{\partial y} \sim \frac{u_\tau}{y}. \tag{2.9}$$

Dimensional analysis for Equation 2.9 leads to a dimensionless constant known as the von Kármán constant, $\kappa = 0.41$.

$$\frac{\partial \overline{U}}{\partial y} = \frac{u_\tau}{\kappa y}. \tag{2.10}$$

Integrating Equation 2.10 and writing it in wall units results in an equation known as the logarithmic law of the wall expressed as

$$u^+ = \frac{1}{\kappa} ln(y^+) + B, \tag{2.11}$$

where $B = 5.2$ is the intercept of the logarithmic profile.

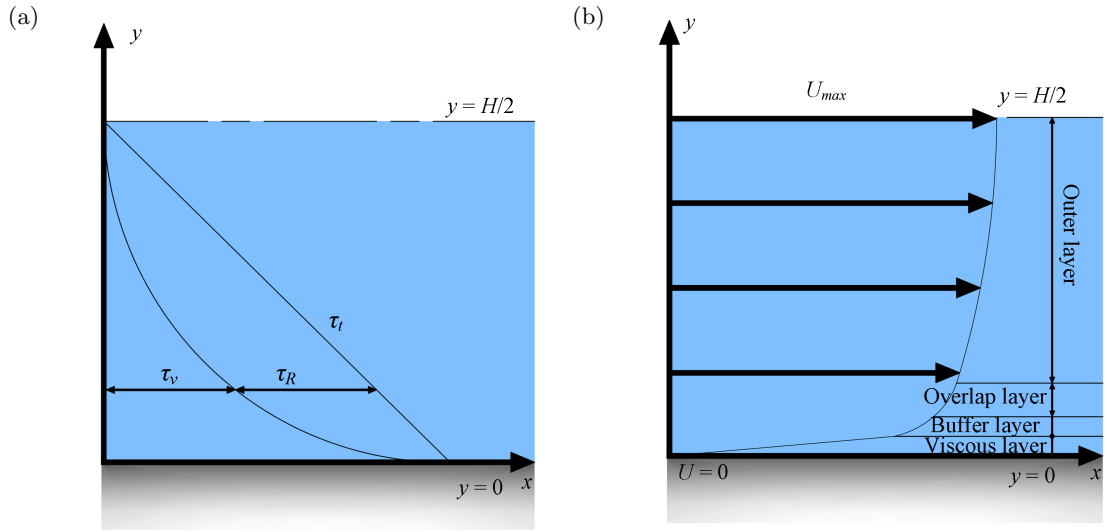

Figure 2.2: (a) Profiles of the shear stresses across the half channel. (b) The adjacent layers of the mean streamwise velocity across the half channel.

2.1.3 Governing equations

The general form of the continuity equation is

$$\frac{\partial \rho}{\partial t} + \frac{\partial(\rho\overline{U})}{\partial x} + \frac{\partial(\rho\overline{V})}{\partial y} + \frac{\partial(\rho\overline{W})}{\partial z} = 0. \tag{2.12}$$

Here t is the time. When an incompressible steady fully developed flow travels through a two-dimensional channel, Equation 2.12 is reduced to

$$\frac{\partial \overline{V}}{\partial y} = 0. \tag{2.13}$$

By applying the no-slip boundary condition as previously specified, Equation 2.13 becomes $\overline{V} = 0$ indicating that the mean flow normal to the plane is zero. Since the flow is only in the $x-$direction, the equations of motion for $x-$ and $y-$directions are respectively

$$0 = -\frac{\partial \overline{P}}{\partial x} + \frac{d}{dy}\left(\mu\frac{d\overline{U}}{dy} - \rho\overline{uv}\right), \tag{2.14}$$

$$0 = -\frac{\partial \overline{P}}{\partial y} - \rho\frac{d\overline{v^2}}{dy^2}. \tag{2.15}$$

By applying the boundary condition of $\overline{v^2} = 0$ at the wall ($y = 0$), Equation 2.15 can be integrated about $y-$direction as

$$P_w = \overline{P} + \rho\overline{v^2}, \tag{2.16}$$

here P_w is the mean pressure at the wall. Since $\overline{v^2}$ is independent of x, $dP_w/dx = \partial P/\partial x$. Equation 2.14 can be written in terms of the total shear stress (τ) as expressed in Equation 2.3.

$$\frac{d\tau}{dy} = \frac{dP_w}{dx}, \tag{2.17}$$

2.2 Slip Boundary Condition

At a solid-liquid interface, the liquid molecules and the surfaces molecules stick together owing to the viscous effects. As a result, the relative velocity between the solid surface and the fluid is zero as shown in Figure 2.3. This phenomenon is referred to as the no-slip boundary condition. The no-slip condition was first introduced by Bernoulli in 1738 (Elger et al., 2013). In the 19th century, Navier proposed the first concept of the slip boundary condition (Navier, 1823). Navier believed that the slip condition is proportional to the rate of strain, (or shear rate) at the interface. The model that Navier proposed is known as the linear Navier boundary condition:

$$\Delta U|_{wall} = U_{liquid} - U_{surface} = l_s \frac{\partial U}{\partial y}|_{wall}, \tag{2.18}$$

here $\Delta U|_{wall}$ is the velocity difference at the interface, U_{liquid} is the velocity of the fluid at the wall which will be referred to later as U_s, $U_{surface}$ is the surface velocity and equal to zero for stationary surfaces, and l_s is the effective slip length. In Equation 2.18, l_s is interpreted as the distance where the no-slip boundary condition is met as presented in Figure 2.3. Equation 2.18 satisfies the no-slip condition if l_s is zero.

2.3 Superhydrophobic surfaces

Introducing a gas layer over a solid surface can reduce skin-friction in liquid flows, and a superhydrophobic surface (SHS) is one of the ways to introduce this layer. The SHSs were

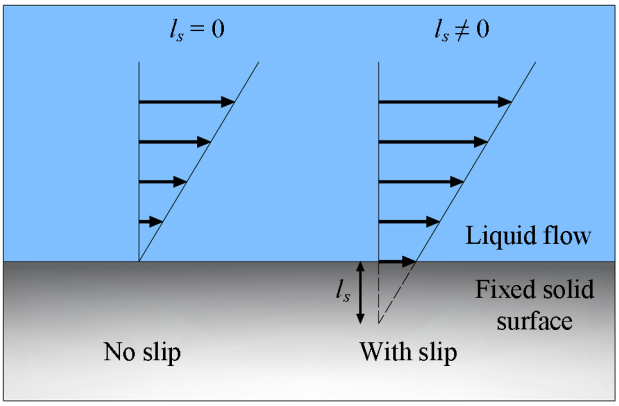

Figure 2.3: Schematic of the no-slip and slip boundary conditions.

first inspired by the water repellent structures (i.e., hydrophobic) of lotus leaves (Rothstein, 2010). It was found that the structure on lotus leaves enhances the self-cleaning feature by rolling the rain droplets over the leaves without wetting them. The recent development of micro-fabrication techniques has made it possible to mimic the structures of these leaves. The fabricated SHSs consist of nano/micro-scale hydrophobic features that can hold small gas bubbles when exposed to a liquid generating the Cassie-Baxter state of wetting (Cassie and Baxter, 1944). Under this state, the surface is covered with an air layer (or a plastron) that prevents liquid from reaching the surface. The thin air layer over the SHS increases the contact angle to higher than 150°. Also, this air layer results in a slip boundary condition at the gas-liquid interface.

The air layer over an SHS can be removed (i.e., depleted), due to several reasons as will be discussed in Section 2.3.5, forming a transition from Cassie-Baxter state to the Wenzel state of wetting (Wenzel, 1936). Under the Wenzel state, the SHS will lose its ability to generate the slip boundary condition and will act as a regular no-slip surface (denoted as smooth surface). The duration that an SHS takes to transfer from the Cassie state to Wenzel state is known as the SHS longevity.

2.3.1 Skin-friction reduction

Skin-friction is a force that appears when a moving fluid comes in contact with a stationary surface or vice versa. It is found that relaxing the no-slip boundary condition of solid surfaces can sufficiently reduce the skin-friction, and the presence of the air layer over the SHSs can satisfy this condition (Vinogradova, 1999).

In laminar flows, the reduction of the skin-friction by SHS has been more straightforward than in turbulent flow. An extensive number of investigations showed that drag reduction (DR) over SHSs in laminar flows depends directly on the slip velocity, which is a function of the surface area covered by air. In laminar flows, several pioneering investigations by Balasubramanian et al. (2004); Ou et al. (2004); Choi et al. (2006); Joseph et al. (2006) confirmed DR over the SHSs. In turbulent flows, however, experiments over SHSs have demonstrated scattered results (different values of DR and occasional drag increases). The early experiment of Watanabe et al. (1999) did not result in any DR in a turbulent pipe coated with a water-repellent layer. Aljallis et al. (2013) observed a 30% DR in transitional flows followed by drag increase in turbulent flows over a flat plate coated with superhydrophobic particles. Later, Bidkar et al. (2014) obtained up to 30% turbulent DR by direct force measurement over SHSs with random texture. The DR variations are not only associated with the superhydrophobicity level of the surface, which can be best characterized by contact-angle hysteresis (Gose et al., 2018). Several experiments have shown that the efficacy of the surfaces also depends on surface roughness (Aljallis et al., 2013; Ling et al., 2016), the level of dissolved air in water (Ling et al., 2017), wall shear stress (Vajdi Hokmabad and Ghaemi, 2017), and hydrostatic pressure (Lei et al., 2009; Dilip et al., 2014).

Owing to the complexity of the mechanism of reduction of skin-friction of SHS in turbulent flow, the investigation of Rastegari and Akhavan (2015) developed a theoretical expression to estimate DR over a wall with a slip-free boundary. They decomposed the drag into a term due to slip velocity and another term due to modifications of the Reynolds shear stress based on the original formulation of Fukagata et al. (2002). To obtain this expression, they started with the Reynolds-averaged streamwise momentum equation for

fully developed steady flow as

$$\frac{1}{\rho}\frac{\partial \overline{P}}{\partial x} = \frac{\partial}{\partial x}\left(\nu\frac{\partial \overline{U}}{\partial x} - \overline{uu} - \overline{UU}\right) + \frac{\partial}{\partial y}\left(\nu\frac{\partial \overline{U}}{\partial y} - \overline{uv} - \overline{UV}\right) + \frac{\partial}{\partial z}\left(\nu\frac{\partial \overline{U}}{\partial z} - \overline{uw} - \overline{UW}\right). \tag{2.19}$$

Averaging Equation 2.19 in the streamwise and spanwise directions and integrating in the $y-$directions result in

$$\frac{1}{\rho}\frac{\partial \langle P\rangle}{\partial x}(h-y) = \nu\frac{\partial \langle U\rangle}{\partial y} - \langle uv\rangle - \langle UV\rangle. \tag{2.20}$$

Here, $\langle\rangle$ indicates averaging in time and the streamwise and spanwise directions. Equation 2.20 can also be written as

$$\frac{1}{\rho}\frac{\partial \langle P\rangle}{\partial x}h\left(1-\frac{y}{h}\right) = \nu\frac{\partial \langle U\rangle}{\partial y} - \langle uv\rangle - \langle UV\rangle. \tag{2.21}$$

From the definition of $u_\tau = \sqrt{\tau/\rho}$ and from Equation 2.17, the wall friction velocity can be expressed as

$$u_\tau = \sqrt{-\frac{\partial \overline{P}}{\partial x}\frac{h}{\rho}}. \tag{2.22}$$

Using the expression of the wall friction velocity in Equation 2.21 gives

$$\langle u_\tau^2\rangle\left(1-\frac{y}{h}\right) = \nu\frac{\partial \langle U\rangle}{\partial y} - \langle uv\rangle - \langle UV\rangle. \tag{2.23}$$

To obtain the friction coefficient (C_f), Equation 2.23 is integrated twice from 0 to y and from 0 to h as described before by Fukagata et al. (2002). The integration of the first term of Equation 2.23 and using the expression of the friction velocity and the friction coefficient ($C_f = \tau_w/\frac{1}{2}\rho U_b^2$) result in

$$\int_0^h\int_0^y \langle u_\tau^2\rangle\left(1-\frac{y}{h}\right)dydy = \frac{C_f U_b^2 h^2}{6}. \tag{2.24}$$

The integration of the second term with considering a slip velocity at the wall ($y=0$) (or the velocity at $y=0$ is U_s) yields

$$\int_0^h\int_0^y \nu\frac{\partial \langle U\rangle}{\partial y}dydy = \nu h U_b\left(1-\frac{U_s}{U_b}\right). \tag{2.25}$$

Integrating the third and fourth terms by parts results in

$$\int_0^h \int_0^y \left[-\langle uv\rangle - \langle U\rangle\langle V\rangle\right] dydy = h\int_0^1 \left[-\langle uv\rangle - \langle UV\rangle\right](1-\delta)d\delta. \tag{2.26}$$

Where $\delta = y/h$. Combining Equations 2.24, 2.25, and 2.26 gives

$$\frac{C_f U_b^2 h^2}{6} = \nu h U_b\left(1 - \frac{U_s}{U_b}\right) + h\int_0^1 \left[-\langle uv\rangle - \langle UV\rangle\right](1-\delta)d\delta. \tag{2.27}$$

By rearranging Equation 2.27 to solve for C_f gives

$$C_f = \frac{6}{Re}\left(1 - \frac{U_s}{U_b}\right)\left(\frac{1}{1-3I^+}\right). \tag{2.28}$$

Where I^+ is

$$I^+ = \int_0^1 (1-\delta)\left[-\langle uv\rangle - \langle UV\rangle\right]^+ d\delta. \tag{2.29}$$

Here $\langle U\rangle\langle V\rangle$ is the average quantity of the Reynolds shear stress. The magnitude of $\langle U\rangle\langle V\rangle$ over the no-slip surface is zero, however, over the SHS or surfaces with roughness, it is not zero since $\langle U\rangle\langle V\rangle$ is finite at the peaks of the surface micro-textures. The reduction of skin-friction (i.e., DR) over the SHSs can be estimated from the difference between C_{f0} over the no-slip surface and C_f over the SHS and can be expressed as

$$DR = \frac{C_{f0} - C_f}{C_{f0}}. \tag{2.30}$$

The coefficient C_{f0} over the no-slip surface can be obtained from Equation 2.28 and using the no-slip boundary condition ($U_s = 0$) as follows

$$C_{f0} = \frac{6}{Re}\left(\frac{1}{1-3I_0^+}\right), \tag{2.31}$$

where $I_0^+ = \int_0^1 (1-\delta)\left[-\langle uv\rangle\right]^+ d\delta$. By substituting Equation 2.28 and 2.31 in Equation 2.30 gives

$$DR = \frac{U_s}{U_b} + \left(1 - \frac{U_s}{U_b}\right)\left(\frac{3\varepsilon}{1-3I^+}\right), \tag{2.32}$$

here $\varepsilon = I^{+0} - I^+$. The first term of Equation 2.32 (U_s/U_b) shows the contribution of the effective slip in reducing drag, while the second term of Equation 2.32 reflect the DR due to the change in the turbulence structure over the SHS.

2.3.2 Slip over superhydrophobic surfaces

As discussed previously in Section 2.2, a finite velocity at a solid-liquid interface is known as the Navier slip boundary condition. It was showed numerically first by Min and Kim (2004) that the slip velocity over the SHS can be generated in the wall parallel directions (streamwise and spanwise directions). The expression of the slip velocities in these directions for a stationary wall ($u_{surface} = 0$) can be written from Equation 2.18 as

$$U_s = l_x \left.\frac{\partial \overline{U}}{\partial y}\right|_{y=0}, W_s = l_z \left.\frac{\partial \overline{W}}{\partial y}\right|_{y=0}. \tag{2.33}$$

Here U_s and W_s are the slip velocity and l_x and l_z are the effective slip length in the streamwise and spanwise directions, respectively. As seen in these equations, the slip velocity is linearly proportional to slip length in both directions.

The direct numerical simulation (DNS) of Min and Kim (2004) assumed a homogeneous surface while imposing independent values of effective slip length in the streamwise and spanwise directions (i.e., $l_x \neq 0$ and $l_z \neq 0$). Their investigation showed that an imposed l_x reduces the drag, while l_z results in a drag increase. However, DR due to l_x was larger than the increase of drag due to a similar value of l_z. They attributed the increase of drag by l_z to the intensification of the near-wall streamwise vortices. Busse and Sandham (2012) mapped contours of drag versus l_x and l_z from a DNS of turbulent channel flow to study the effect of an anisotropic boundary condition. They reported that the drag increase due to l_z reaches an asymptote of approximately 50% drag increase when l_z increases beyond 10λ. However, for large l_x exceeding 10λ, DR is independent of l_z. Busse and Sandham (2012) also observed that a finite value of l_x makes the near-wall streaks more organized, while l_z disrupts the coherence of the streaks. These numerical simulations have shed light on the effect of slip anisotropy on DR.

2.3.3 Superhydrophobic surface effects on the mean velocity

In the near-wall region, mean velocity over the SHS increases because of the slip velocity, while the mean velocity reduces away from the wall to maintain the same mass flow rate

(Min and Kim, 2004). To the author's knowledge, the experiment of Ling et al. (2016) was the only work that measured the slip velocity over SHSs in the turbulent regime. Ling et al. (2016) measured the slip velocity over SHSs with a wide range of roughnesses in a turbulent boundary layer using digital holographic microscopy. They reported up to $U_s = 0.73$m/s ($U_s/U_b = 0.36$) over an SHS with 36% DR at a free-stream velocity of 2.0 m/s.

2.3.4 Superhydrophobic surface effects on Reynolds stresses

The effect of slip velocity on the Reynolds stresses has been typically evaluated by comparison with a surface with a no-slip boundary condition (smooth surface) under the same bulk flow conditions. If the Reynolds stresses are normalized with the friction velocity of the smooth surface, reductions in the streamwise, wall-normal, and shear Reynolds stresses are observed in the outer layer as seen in the experiments of Woolford et al. (2009a); Vajdi Hokmabad and Ghaemi (2016); Ling et al. (2016). However, closer to the wall at $y^+ < 10$, the streamwise Reynolds stress, $\langle u^2 \rangle$, and the shear Reynolds stress, $\langle uv \rangle$, are larger than those over the smooth surface (Ling et al., 2016). The increase of $\langle u^2 \rangle$ is associated with the increase of fluctuations by relaxing the no-slip boundary condition. The near-wall wall-normal Reynolds stress, $\langle v^2 \rangle$, is higher than those over the smooth surface in the near-wall (Ling et al., 2016). A near-wall increase of spanwise Reynolds stress, $\langle w^2 \rangle$, was observed in the DNS of Min and Kim (2004) when a spanwise slip was imposed. Rastegari and Akhavan (2015) observed an increase of $\langle w^2 \rangle$ over SHSs with spanwise and streamwise microgrooves. The latter case suggests the presence of spanwise slip over streamwise microgrooves.

2.3.5 Surface longevity

The longevity of the air layer over an SHS indicates the duration of transfer from the Cassie state to Wenzel state. Lei et al. (2009) observed that this transfer is reversible when an SHS with a polydimethylsiloxane (PDMS) substrate is immersed in water under 50-60 mbar followed by pressure release. However, they observed permanent collapse of the air pockets due to an irreversible transfer to the Wenzel state at higher pressures. Samaha et al. (2012) used a technique based on total internal reflection of a laser beam to detect the presence of

the air layer over an SHS in contact with a wall jet. Their results show that the depletion of the air layer is a function of flow rate. Vajdi Hokmabad and Ghaemi (2017) also applied a similar technique to an SHS in a laminar boundary layer. They observed intensified dissolution of the plastron into the water due to convection by the flow and the presence of a particulate phase. In general, the thickness and morphology of the air plastron and the DR of the SHS are functions of time, flow rate, and level of dissolved air.

Chapter 3

Experimental setup

This chapter is organized into three sections. The first section introduces all components of the flow facility that was used for Experiment 1 presented in Chapter 5. This flow facility will be referred to as the flow facility 1. The second section of this chapter introduces flow facility 2 which is used for the experiments in Chapters 6, 7, and 8. The third section describes the SHSs fabrication process. The latter also includes characterization of the fabricated surfaces including scanning electron microscope (SEM), profilometer, and contact angle measurements.

3.1 Flow facility 1

3.1.1 Water tunnel

The turbulent channel flow is obtained by submerging a rectangular test section in a large open-top water tunnel (water flume) in the Laboratory of Turbulent Flows at the University of Alberta. The water tunnel consists of two large reservoirs and a transparent open-top tunnel connecting the two reservoirs (see Figure 3.1). Each reservoir volume is 2,200 liters. The transparent section can hold up to 1,700 liters. The transparent section of the water tunnel has dimensions of 5 m long, 0.65 m width, and 0.52 m height. The water in the tunnel is circulated through two centrifugal pumps (#401140810031 DEMING). Each pump is equipped with a 3 horsepower motor with a maximum speed of 1760 revolutions per minute (131504 WATTSAVER). The maximum achievable velocity in the tunnel is 0.15 m/s.

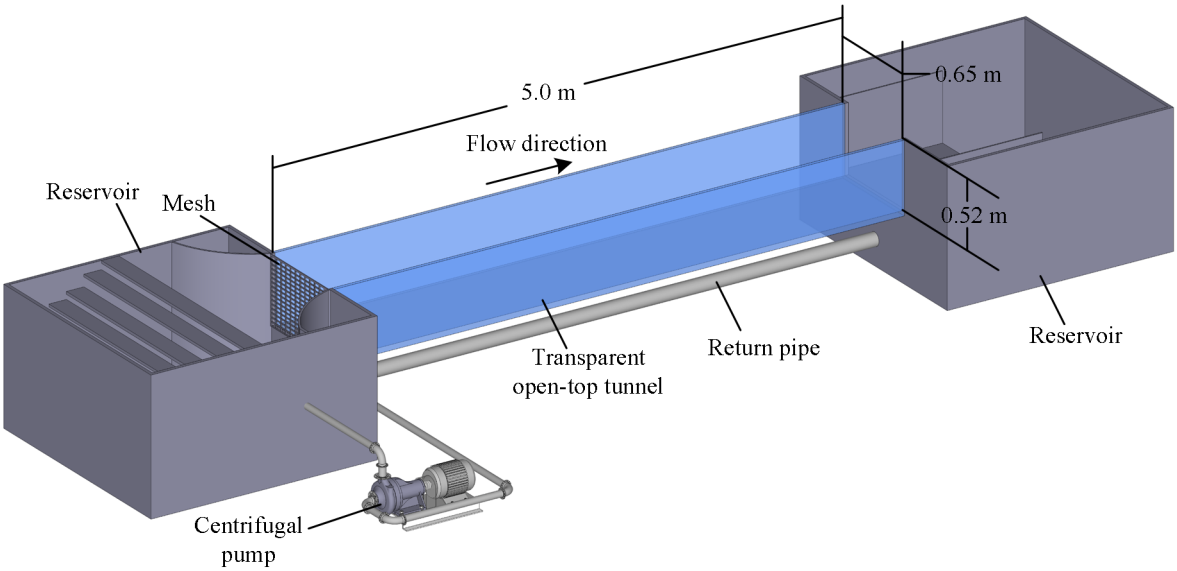

Figure 3.1: Schematic of the main components of the water tunnel including the two reservoirs, transparent channel, and a centrifugal pump.

3.1.2 Turbulent channel flow

The submerged rectangular test section (turbulent channel flow) has a 3 m length (L) in the streamwise direction (x), 25 mm height (H) in the wall-normal direction (y), and 540 mm width (Wi) in the spanwise direction (z). The bottom wall of the submerged channel is a large glass sheet placed 5 cm above the bottom wall of the flume to avoid entrance of the flume boundary layer. A honeycomb flow straightener was placed at the entrance of the submerged channel as shown in Figure 3.2. The side of the embedded channel has a viewing window to provide optical access for the cameras. The top wall is made from acrylic sheets 1 in to accommodate a flush-mounted insert plate for testing the SHS. The insert plate is machined from an acrylic sheet (baseline surface), and located 1.9m ($76H$) downstream of the entrance. It is 570 mm ($22.8H$) long and 320 mm wide. The long flow development length ($85H$ prior to the measurement location) and the large aspect ratio ($Wi/H = 21.6$) ensure two-dimensional fully developed turbulent channel flow at the measurement location.

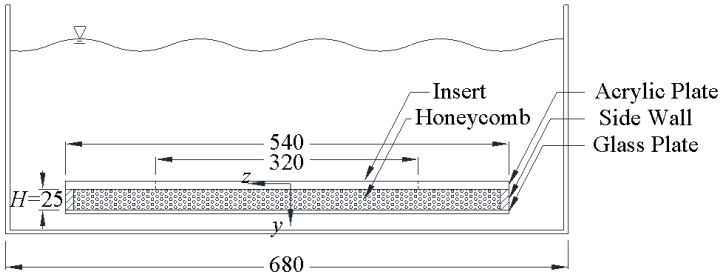

Figure 3.2: Schematic of the submerged rectangular test section showing the channel flow consisting of a glass bottom wall, a top acrylic wall, honeycomb at the entrance, and side walls. The top wall has an insert plate to flush-mount the test surfaces. All dimensions are in mm

3.2 Flow facility 2

The closed-circuit turbulent channel flow is shown in Figure 3.3. The test section had a rectangular cross-section with a height of $H = 6$mm, width of $Wi = 40$mm, and total length of 1.2 m ($200H$). The aspect ratio (Wi/H) of the channel cross-section was 6.7. This aspect ratio is close to the minimum recommended aspect ratio of 7 by Dean (1978) to maintain a two-dimensional (2D) flow in the center of the channel. The investigation of Vinuesa et al. (2014) also showed a negligible effect ($\sim 1\%$) on centreline Reynolds stresses for a channel with an aspect ratio of 7. The top and bottom walls of the channel were made of transparent acrylic, while the sidewalls were made of glass. The coordinate system in the streamwise, wall-normal and spanwise directions is indicated with x, y, and z as displayed in Figure 3.3. The settling chamber upstream of the test section had a diameter of 82.5 mm and included a honeycomb structure to break down the large eddies. The chamber was connected to the test section through a 3D contraction, which was manufactured by 3D printing and coated with epoxy. The contraction ratio with respect to the diameter of the chamber was 14:1 in the y-direction and 2:1 in the z-direction. The loop was equipped with a centrifugal pump controlled by a variable frequency driver (VFD). An electromagnetic flow meter (FLR6305D, Omega Engineering Inc., USA) was used to monitor the mass flow rate. A proportional-integral-derivative (PID) controller was developed with commercial software (LabView 2016,

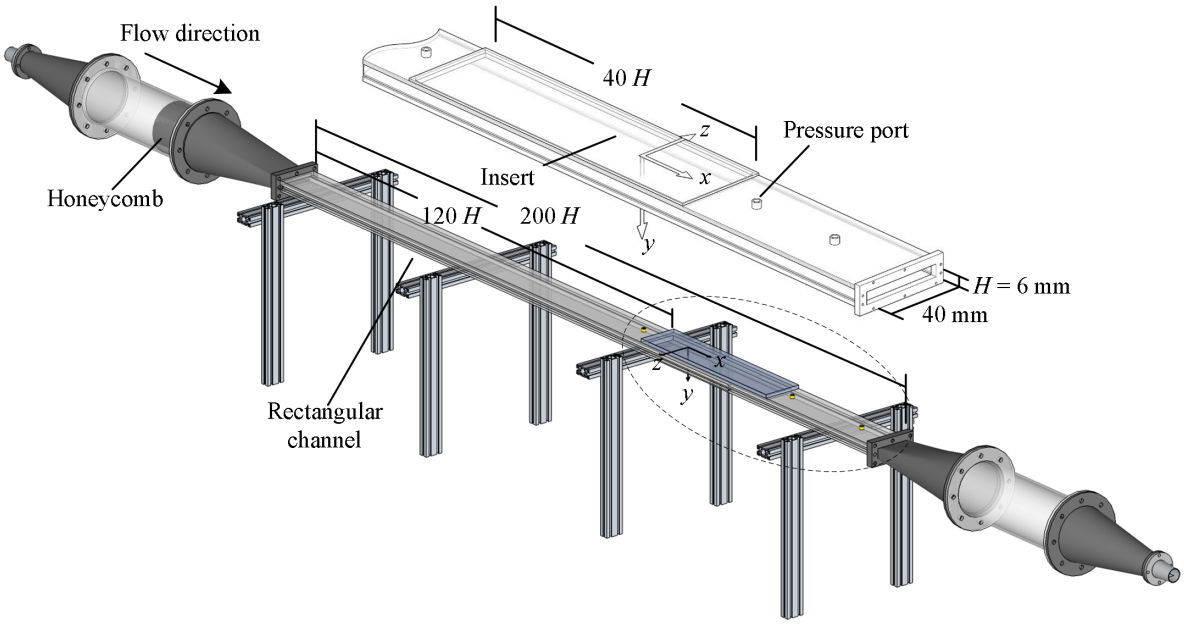

Figure 3.3: Schematic of the experimental set-up. The inset shows a closer view of the test section and the replaceable insert to mount the SHS.

National Instruments) to control the flow rate. The PID controller communicated with the VFD to control the pump revolutions per minute through an input/output card (NI USB-6001, National Instruments). The front panel and the block diagram of this code are attached in Appendix A and B, respectively.

3.3 Superhydrophobic surfaces fabrication and characterization

The recent developments in microfabrication processes have made it possible to generate surfaces with a variety of textures, however, the processes are still expensive and limited to small sizes and flat surfaces. Inexpensive and less complicated fabrication processes can generate large and non-flat SHSs. Examples of these processes are coating and sandblasting. In this thesis, two types of fabrication processes were used to generate the SHSs. The first type is a superhydrophobic coating and the other fabrication process is sandblasting. Details about the fabrications processes and the characterizations for the final surfaces are discussed in the following sections.

3.3.1 Superhydrophobic coating

It was found that coating a surface with a water repellent layer can generate SHS with short fabrication time, inexpensive cost, and large scale. The commercial spray coating NeverWet (Rust-Oleum USA), is an aerosol-based superhydrophobic coating, which consists of two coating layers. This spray coating was used in previous experiments (Aljallis et al., 2013; Zhang et al., 2015; Vajdi Hokmabad and Ghaemi, 2016; Abu Rowin et al., 2018). The first layer is a silicone-based coating of methyl isobutyl ketone and butyl acetate (Liu et al., 2016; Gupta et al., 2016). This layer is hydrophilic and enhances surface adhesion before spraying the microparticles of the next layer. One pass of the silicone-based coating was applied, the surface was left to dry for about 30 minutes, and then two passes of the second coating were applied. The surface was then left for 12 hours to dry before submerging in water. As shown in the SEM images in Figure 3.4, the produced SHS has a random distribution of protrusions, which can be as large as 50μm. Contact-angle measurements were performed by characterizing the three-phase contact line using the Young–Laplace fitting method (Young, 1805). Measurements were carried out using a droplet shape analyzer (DSA-100 KRÜSS GmbH) by placing a 10 μm droplet at three locations over eight SHSs. The surfaces had an average contact angle of 149°, with a standard deviation of 2.2° as shown in Figure 3.4. The contact-angle hysteresis was 2.8°, with a standard deviation of 1.8°, estimated as the difference between the advancing and receding contact angles. The roll-off angle over the current SHS was relatively small and equal to 1.4°, with a standard deviation of 0.6°.

A step profiler (XP-300, Ambios Technology, USA) with 2.5 μm stylus tip radius and 30 μm/s scanning speed was used to measure the variation of the SHS roughness heights as shown in Figure 3.5a. The measurement uncertainty was estimated to be approximately 0.1 μm based on measurements on a microscope slide (i.e., flat surface). The stylus force was set to 1 mg, since higher forces resulted in scratching the surface and peeling the hydrophobic coating. The surface roughness, R, in Figure 3.5a, estimated from Equation 3.1 (Farshad

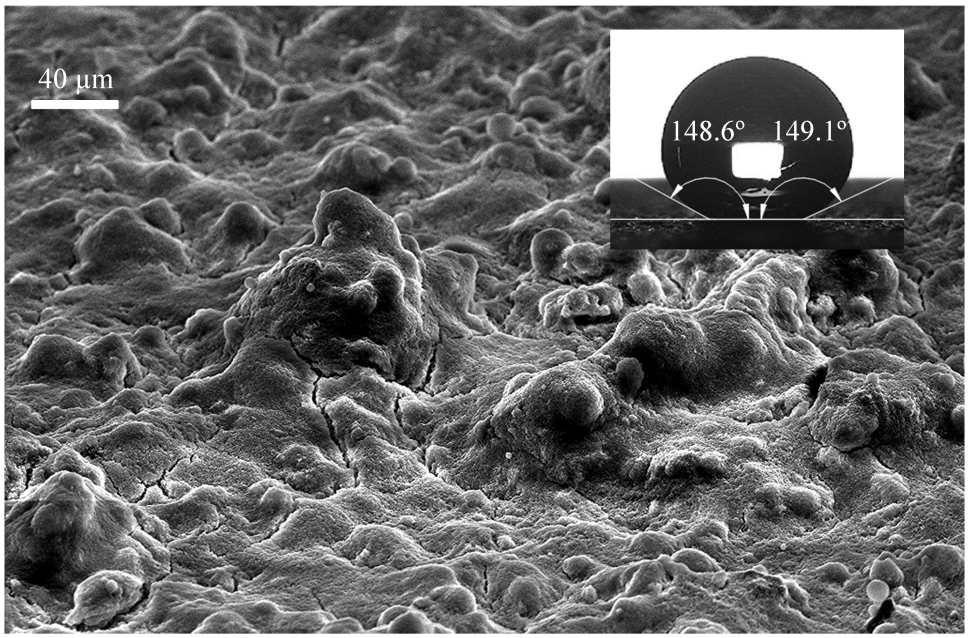

Figure 3.4: Micrographs of the SHS obtained using scanning electron microscopy (EVO-MA10, Zeiss microscope). The inset presents image of a water droplet on the SHS for contact angle measurement.

and Pesacreta, 2003), appears to have different peak heights up to approximately 20 μm.

$$R = \frac{1}{S_l} \int_0^{S_l} |S(x) - \overline{S}| dx, \tag{3.1}$$

where S_l is the surface length, $S(x)$ is the surface profile in the wall-normal direction, and $\overline{S}$ is the mean of the surface profile $S(x)$. The root-mean-square of surface roughness (R_{rms}), estimated from Equation 3.2, was 4.9, with a standard deviation of 0.3 μm mm based on measurements at different locations on eight SHSs.

$$R_{rms} = \sqrt{\frac{1}{S_l} \int_0^{S_l} |S(x) - \overline{S}|^2 dx}, \tag{3.2}$$

The average texture width, g, between the peaks with $R > 3\mu$m is 85 μm. The profilometer measurement over a longer distance of 120 mm is also shown in Figure 3.5b to characterize the low-wavenumber features. The mean distance between roughness peaks (d_p) which are larger than a prescribed threshold is illustrated in Figure 3.5c. As can be seen, d_p increases with the increase of the roughness height and reaches up to a d_p of 26 mm for the largest roughness peaks with $R = 22\mu$m. The plastron visualization of Reholon and

Ghaemi (2018), over an SHS with a similar structure under turbulent flow, has shown that at high DR ($> 15\%$) a relatively flat air plastron covers the surface roughness. At lower DR, the surface elements are exposed to the liquid flow and a rough interface forms.

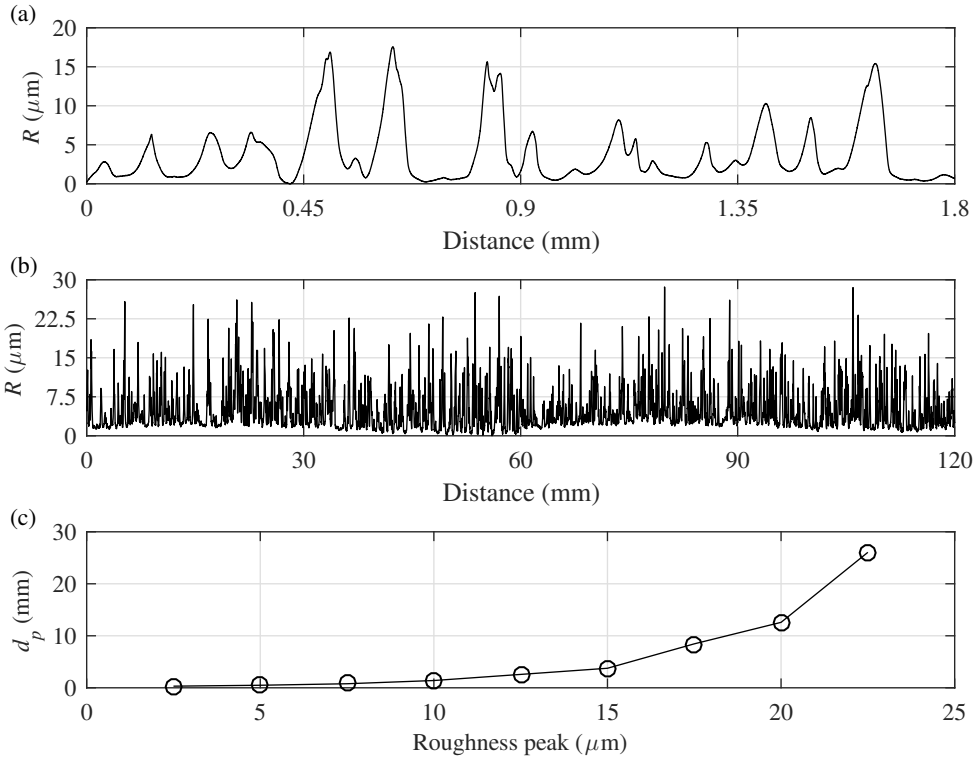

Figure 3.5: Samples of the profilometer measurement of microscale roughness of the SHS over (a) 1.8 mm and (b) 120 mm of the sample. (c) The mean distance between roughness peaks.

3.3.2 Sandblasting superhydrophobic surfaces

Sandblasting is another common way of manufacturing inexpensive and scalable SHSs. Three randomly textured SHSs were fabricated by the Interracial Fluid Mechanics group at the University of Texas. Aluminum substrates with dimensions of 230 mm ($38H$) long and 35.5 mm wide were used. The substrates were first processed by a sandblasting process with different particle sizes and sandblasting speed. This process is followed by acid etching in a 12 molar Hydrochloric acid bath at high temperature to simulate aluminum oxidation. The final step included coating the surfaces with low surface energy material through a

chemical deposition of polytetrafluoroethylene (PTFE). The topography of the fabricated surfaces is presented in Figure 3.6 with a top down view scanning electron microscopy (SEM) images. The SHSs in Figure 3.6(a, b, c) are presented from small to large roughness and denoted by SHS-S, SHS-M, and SHS-L, respectively. The three SHSs share similar pattern of random distribution of voids and pits. The contact angle measurements over these SHSs were performed using a droplet shape analyzer (DSA-100 KRÜSS GmbH). The contact angle was $148.2°, 151.1°$, and $151.6°$ over SHS-S, SHS-M, and SHS-L, respectively.

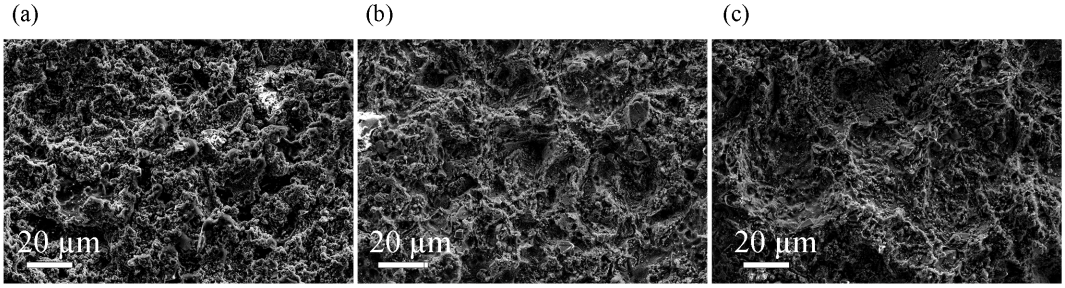

Figure 3.6: SEM images of SHSs with (a) small (SHS-S), (b) medium (SHS-M), and (c) large (SHS-L) roughness

The roughness of the fabricated surfaces was analyzed using the step profiler (XP-300, Ambios Technology, USA). For the current profilometer measurement, the scanning speed and the stylus force were set at 30 μm/s and 10 mg, respectively, over 1.8 mm samples of SHSs in Figure 3.6 (a, b, c). The average root-mean-square height of SHS-S, SHS-M, and SHS-L roughness, R_{rms}, are 1.44, 2.58, and 4.5 μm, respectively. The normalized surface roughness by the wall unit of the smooth surface (it will be introduced in Section 8.1), $k_0^+ = R_{rms}/\lambda_0$, is 0.11, 0.20, and 0.35 for SHS-S, SHS-M, and SHS-L, respectively.

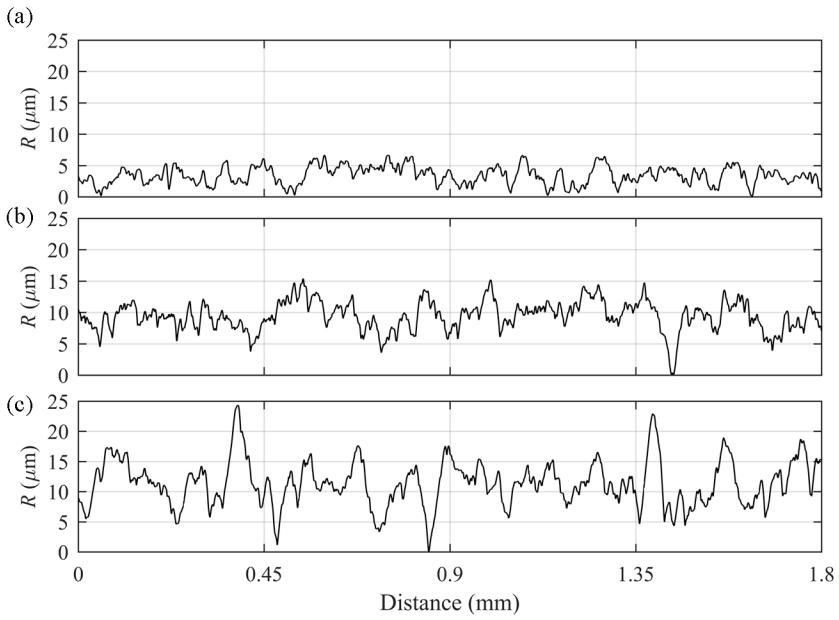

Figure 3.7: Profilometer measurement over 1.8 mm samples of (a) SHS-S, (b) SHS-M, and (c) SHS-L

Chapter 4

Measurement systems

This chapter is organized into five sections. The first section describes a macroscopic particle image velocimetry used in Chapter 5. The second section of this chapter introduces a microscopic particle tracking velocimetry (micro-PTV) also used for the same investigation in Chapter 5. The third section includes three-dimensional PTV performed in Chapters 6, 7, and 8. Section four includes a two-dimensional time-resolved PTV used in Chapter 7. The final section of this chapter explains the pressure measurement used in Chapters 6 and 7. In each section of this chapter, the apparatus and processing parameters are introduced for each measurement technique. Evaluation of the uncertainties for each measurement system is also included.

4.1 Planer particle image velocimetry

Planer particle image velocimetry (PIV) measurement is utilized to characterize the outer layer of a turbulent channel flow over an SHS in Chapter 5. This measurement is also performed to evaluate the symmetry of the flow by visualizing the turbulent flow across the full-channel height.

4.1.1 Apparatus

An Imager Intense camera (LaVision GmbH) with 1376×1040 pixel charge-coupled device (CCD) sensor (pixel size of 6.45×6.45 μm^2 and 12-bit resolution) images at a magnification of 0.2 with a digital resolution of 32.6 μm/pixel through a $f = 105$ mm Nikkor lens at an

aperture size of $f/8$. The field-of-view (FOV) of this measurement is 44.8×33.9 mm^2. The FOV is located $94H$ downstream of the channel entrance of flow facility 1 (Section 3.1) and $18H$ downstream of the leading-edge of the insert plate as shown in Figure 4.1. The laser beam, generated by a 400 mJ/pulse Nd:YAG laser (Spectra-Physics), is shaped into a collimated laser sheet with 25 mm width in the $y-$direction and 1 mm thickness in the $z-$direction using a combination of spherical and cylindrical lenses. The edges of the laser sheet are directed parallel to the top wall of the channel (in the $x-$direction) to minimize wall reflection. This illumination is carried out using a mirror sealed inside an acrylic column submerged downstream of the channel in the flume, as shown in Figure 4.1. An ensemble of 8000 pairs of double-frame images (with a laser pulse separation of $\Delta t = 1500$ μs) is recorded at 5 Hz. This laser pulse separation results in a maximum particle displacement of 10 pixel in the channel centerline. The camera frames and laser pulses are synchronized using a timing unit controlled by DaVis 7.4 (LaVision GmbH).

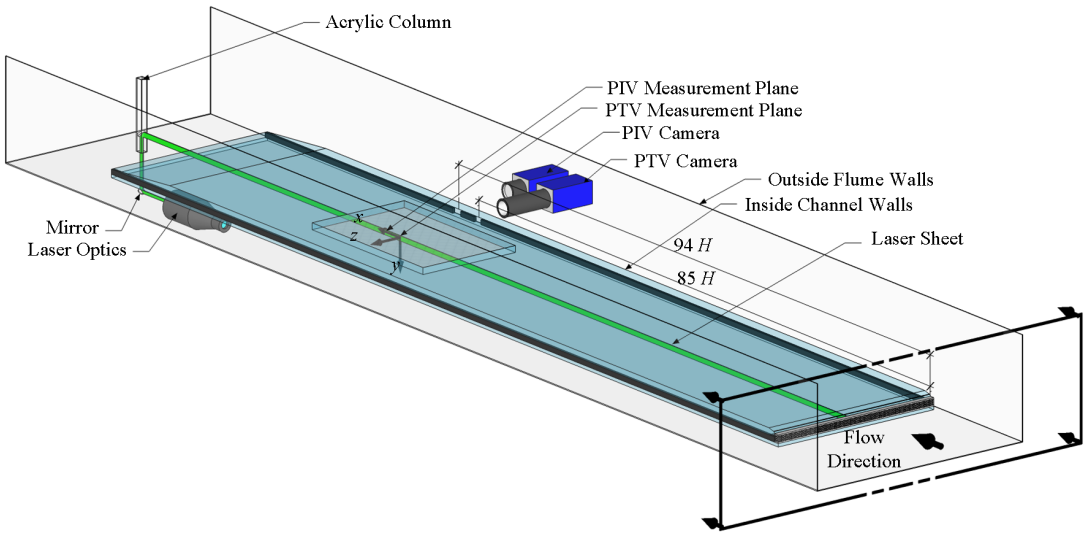

Figure 4.1: The PIV and micro-PTV cameras image a wall-normal streamwise plane (xy plane) illuminated by a collimated laser sheet with edges parallel to the channel wall to minimize wall reflection.

4.1.2 Image processing

The PIV images are processed in DaVis 8.3 (LaVision Gmbh). The minimum intensity of the ensemble of the PIV images is subtracted from each image. The images are also normalized by the average intensity of the ensemble to increase the signal-to-noise ratio before applying the cross correlation algorithm. Multi-pass cross correlation with a final interrogation window (IW) size of 48×48 pixels (1.5×1.5 mm$^2, 17.6^+ \times 17.6^+$) with 75% overlap are applied. The obtained vector fields are post-processed by applying the universal outlier detection (Westerweel and Scarano, 2005). The vector range is also limited to 0-14 pixels for the U component and -3 to 3 pixels for the V component of the velocity vector. A multi-pass ensemble of correlation (EOC) with an initial IW size of 96×96 pixels and a final IW size of 8×8 pixels (0.2×0.2 mm$^2, 2.9^+ \times 2.9^+$) with 75% overlap are applied to obtain the mean velocity profile. Parameters of the PIV setup are listed in Table 4.1.

Magnification	0.2	
Digital resolution	32.6 μm/pixel	
Time interval (Δt)	1,500 μs	
Measurement field	1376×1040 pixel 44.8×33.9 mm^2 $504.8^+ \times 381.5^+$	
Wall accuracy	± 5 pixel ± 163.5 μm $\pm 1.8^+$	
Velocity evaluation	Correlation of double-frame	Ensemble of correlations
IW/ bin size	48×48 pix	8×8 pix
$(\Delta x, \Delta y)$	1.5×1.5 mm^2 $17.6^+ \times 17.6^+$	0.2×0.2 mm^2 $2.9^+ \times 2.9^+$
IW / bin overlap	75%	75%
Application	Outer layer turbulence	$\langle U \rangle$ across the channel

Table 4.1: Parameters of the PIV system for measurement of the outer layer flow

4.1.3 Uncertainty evaluation

The uncertainty sources of optical diagnostic techniques are crucial to determine. The work of Park et al. (2008) categorized the sources of uncertainty for optical diagnostic techniques into four main categories: calibration, displacement of particle image, time interval, and experiment condition. The calibration uncertainty can include a physical error due to target manufacturing and an error due to the reference board. The displacement of particle image uncertainty is typically the largest source of error since it includes the error in detecting the particles' position and the data processing errors. The former is affected by the illumination source fluctuation, lens aberration, sensor distortion, and alignment of the viewing angle. The data processing errors include the subpixel analysis. The uncertainty due to the delay generator or pulse timing can be included under the time interval uncertainty. The experimental condition uncertainties include the time response of the tracers and the out-of-plane motion component. The accumulation of these uncertainties as listed in Table 4.2 for the current PIV system is 2.1 mm/s. Although the calibration uncertainty is typically smaller than the displacement of particle uncertainty, the calibration uncertainty was the largest magnitude of the current measurement (as listed in Table 4.2) due to the poor resolution of the used target. The sensitivity coefficients, c, for the uncertainties due to the calibration, displacement of particle image, and time interval are estimated from the ratio of the maximum particle displacement (13 pix) to Δt, the digital resolution to Δt, and the maximum particle displacement (in mm) to $(\Delta t)^2$, respectively. This uncertainty is equivalent to 0.09 pixel similar to the 0.1-pixel assumption of Young et al. (1993) for the accuracy of particle peak detection. Uncertainty of estimating the measured wall shear stress from the current PIV is discussed in Section 5.2.2.

The estimation of the wall location is an important factor for predicting the slip length and slip velocity over SHSs. It has been shown before that the wall location can be determined precisely in the 2D measurements from the distance between the mirrored particles at the surface in the particle images (Kähler et al., 2006). However, no mirrored particles above the surface were found when the surface was covered with the superhydrophobic coat-

Error sources	Magnitude (unit)	c (unit)	Total (unit)
Calibration	1.7 E-4 (mm/pix)	8,666.6 (pix/s)	1.5 (mm/s)
Displacement of particle	3.0 E-2 (pix)	21.7 (mm/pix s)	6.6 E-1(mm/s)
Time interval	5.4 E-9 (s)	188,355.5 (mm s^{-2})	1.0 E-3(mm/s)
Experiment condition	1.7 E-5 (mm/s)	1.0	1.7 E-5(mm/s)

Table 4.2: Summary of uncertainties for velocity from the current PIV. c is the sensitivity coefficient

ing, and a strong reflection appeared at the wall due to the air layer. Therefore, the location of the top and bottom walls is detected from the intensity peak (I_{max}) of the remaining reflection of the laser sheet at the wall. The I_{max} location is obtained by detecting the local maxima on a plot of intensity versus y averaged over the ensemble of the images and also along the $x-$direction. The upper bound uncertainty of this technique is equivalent to the thickness of the glare line, which is estimated using the width of the intensity peak at I_{max}/e^2. This is equivalent to ± 3 pix (163.0 μm) as presented in Table 4.1. The total measurement uncertainty, from 2.1 mm/s of Park et al. (2008) analysis and the error of estimating the wall location, is 0.10 mm.

4.2 Long-range microscopic particle tracking velocimetry

The long-range microscopic particle tracking velocimetry (micro-PTV) is used to study the flow over an SHS in the inner layer as will be presented in Chapter 5. This measurement is carried out simultaneously with the PIV measurement (introduced in Section 4.1) in flow facility 1 (discussed in Section 3.1) to allow scrutiny of the inner and outer layer flows over the same superhydrophobic plastron.

4.2.1 Apparatus

Micro-PTV with high spatial-resolution is carried out using an Imager Intense CCD camera (LaVision GmbH) equipped with a Nikkor lens with a focal length of $f = 200$ mm at an aperture size of $f/11$. The lens is connected to a 360 mm extension tube (bellows) to allow a working distance of 370 mm. The combination results in a magnification of 1.6 and

a digital resolution of 3.92 μm/pixel. The estimated depth-of-field of 0.3 mm is smaller than the laser sheet thickness ($\sim$ 1 mm) ; therefore, the presence of out-of-focus particle images is expected. Mirco-PTV measurements are carried out at $85H$ downstream of the channel entrance and at $9H$ downstream of the leading-edge of the insert plate as shown in Figure 4.1. The FOV is 5.3 mm $\times$ 4.0 mm in the $x-$ and $y-$directions, respectively. An ensemble of 8000 pairs of double-frame images is recorded with $\Delta t = 1500$ μm with a maximum displacement of 70 pixel in the streamwise direction.

4.2.2 Image processing

Minimum intensity subtraction and image normalization are applied before carrying out particle tracking. The number density of the particles in the images is around 4 particles/mm^2. The PTV algorithm was developed in MATLAB to only track the in-focus particles. The algorithm initiates by detection of local maxima larger than a specified intensity threshold. The local maxima are rejected if multiple peaks are detected within a rectangular window of 60×45 pixels in the $x-$ and $y-$directions, respectively. This filter prevents the detection of erroneous pairs in the subsequent steps. The area of particle images is estimated, and particles outside of 3–10 pixels are rejected. Particle images smaller than 3 pixels in the area can introduce bias errors due to peak locking (Kähler et al., 2012), while particles larger than 10 pixels are out-of-focus. The pair detection was carried out using an initial predictor obtained by an ensemble of correlations (EOC) of the micro-PTV images (Meinhart et al., 2000). The multi-pass EOC process initiates with a window size of 256×256 pixels to detect the large particle movements and follows by a smaller window size of $8 \times 8 (31.3 \times 31.3$ mm^2) with 75% overlap. The PTV algorithm applied the estimated velocity from EOC to search for the particle in the second frame in a $\Delta x, \Delta y = 60 \times 30$ pixel neighborhood. Only particle pairs with a peak intensity ratio of 0.25–1.8 are selected for the final sub-pixel peak detection using a Gaussian fit. Summary of the micro-PTV processing parameters are listed in Table 4.3.

Wall detection has been carried out similar to the method applied to the PIV im-

ages. The uncertainty of estimating the wall location based on the micro-PTV images is 1.5 pixels = 5.8 μm. As discussed in the previous section, the measurement system uncertainty can be estimated from the 0.1-pixel assumption of Young et al. (1993) for the accuracy of particle peak detection. Thus, the uncertainty of the current micro-PTV from the error of peak detection is 0.26 mm/s. The total uncertainty from the uncertainty of estimating the wall location and the accuracy of particle peak detection for the current micro-PTV measurement is 0.006 mm and 3.9 mm/s.

Magnification	1.6		
Digital resolution	3.92 μm/pixel		
Time interval Δt	1,500 μs		
Measurement field	1376×1040 pixel 5.3×4.0 mm^2 $60.7^+ \times 45.8^+$		
Wall accuracy	± 1.5 pixel ± 5.8 mm $\pm 0.06^+$		
Velocity evaluation	Particle tracking		Ensemble of correlations
IW/ bin size	1209×100 pix	1290×10 pix	24 × 24 pix
$(\Delta x, \Delta y)$	4.7×0.4 mm^2 $53.3^+ \times 4.4^+$	5.0×0.04 mm^2 $56.9^+ \times 0.44^+$	0.09×0.09 mm^2 $1.0^+ \times 1.0^+$
IW / bin overlap	75%	75%	75%
Application	Inner layer turbulence	$\langle U \rangle$ in the inner layer	Near wall $\langle U \rangle$

Table 4.3: Parameters of the micro-PTV system for measurement of the inner layer flow

The average velocity and high-order turbulence statistics are obtained by averaging the particle velocities sorted in wall-normal bins. The mean velocity profile is obtained by averaging over $\Delta x, \Delta y = 1290 \times 10$ pixel (5.0×0.04 mm$^2, 56.9^+ \times 0.44^+$) bins, while the second-order statistics (Reynolds stresses) are obtained by averaging over larger bins with $\Delta x, \Delta y = 1290 \times 100$ pixel (5.0×0.39 mm$^2, 56.9^+ \times 4.4^+$) to ensure statistical convergence.

4.3 Time-resolved 3D particle tracking velocimetry

Time-resolved 3D-PTV was used to measure the trajectory of tracer particles in a 3D volume covering the inner layer of flow facility 2, shown in Section 3.2, over the test surfaces. The applied Lagrangian particle tracking technique is based on the shake-the-box (STB) method of Schanz et al. (2016) and carried out in DaVis 8.4 (LaVision GmbH). This method uses a combination of trajectory predictions and an image matching technique (shaking) based on the iterative particle reconstruction (IPR) technique of Wieneke (2012) to obtain an accurate estimation of particle position. The STB method can provide measurements with high spatial resolution in the vicinity of the wall ($y^+ \sim 1$), as shown previously by Schröder et al. (2015) and Novara et al. (2016).

4.3.1 Apparatus

The imaging system consisted of four high-speed Phantom v611 cameras with a complementary metal oxide semiconductor (CMOS) sensor of 1280 pixel × 1280 pixel. The CMOS sensor features 20 μm ×20 μm pixels with 12-bit resolution. The cameras were arranged in a plus-like arrangement (Scarano, 2012) as visualized in Figure 4.2. The cameras were equipped with Scheimpflug adapters to align the DOF with the laser sheet. Nikon 105 mm lenses with aperture settings of $f/22$ were used. The magnification and digital resolution of the imaging system were 0.56 and 35.5 μm/pixel, respectively. The solid viewing angle between the wall-normal axis and the cameras was between 25° and 30°. The illumination was provided by a dual-head Nd:YLF laser (DM20-527, Photonics Industries) with 20 mJ/pulse. Spherical and cylindrical lenses were used to form a collimated laser sheet. The lower edge of the laser sheet was cropped by a knife-edge filter, while the upper edge of the laser sheet was cropped by the channel wall to ensure a top-hat intensity profile starting from the wall surface. The cropping resulted in a final laser sheet thickness of 2 mm in the $y-$direction and 21 mm in the $x-$direction. The measurement volume was 21 mm × 2 mm × 21 mm, which is equivalent to 596 pixel × 56 pixel × 596 pixel in the $x-, y-$, and $z-$ directions. The laser pulses and the four high-speed cameras were synchronized using

a programmable timing unit (PTU X, LaVision GmbH) controlled by DaVis 8.2. Nine sets of 1610 single-frame images were recorded at a frequency of 4 kHz. At this recording frequency, the maximum particle displacement was approximately 11 pixels. One of the challenges for particle image velocimetry and PTV over SHSs is caused by the reflection of the laser light from the roughness elements and the shiny air plastron. Thus, the flow loop was seeded with 10 μm red fluorescent particles (polystyrene PS-FluoRed-Fi225) that emit light at a wavelength of 607 nm when illuminated with 530 nm green light. The large size of these tracers is selected to ensure enough light scatter when illuminated with green light. The experiments used a small particle image density of 0.003 particles per pixel (ppp) at 2–3 particles/mm^3. This small particle image density is not a limitation of STB as the algorithm is capable of processing images with up to 0.075 ppp (Schanz et al., 2016). In the current experiment, the smaller particle image density was chosen due to the large amount of monodisperse fluorescent particles required to seed $\sim$ 40 litres of water. As result, spatially uncorrelated data at low ppp were collected over a longer time to obtain statistical convergence. The band-pass filters (#1108573, LaVision) with wavelength limits of 545–800 nm were attached to each camera to record only the fluorescent emitted light.

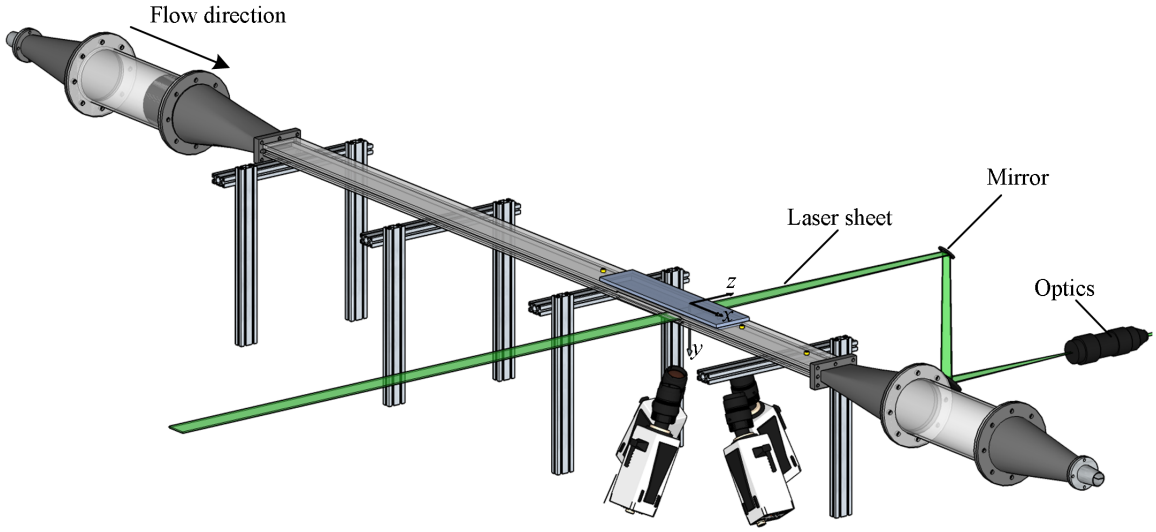

Figure 4.2: Schematic of the experimental set-up showing the camera arrangement and the illumination path for the 3D-PTV experiment.

4.3.2 Image processing

A 2D calibration target with 2 mm spaced holes was utilized for the initial calibration of the four cameras. The target was moved twice with 1 mm increments in the $y-$direction by a micrometer traverse, resulting in three parallel planes. The mapping function between the image and the physical 3D space was carried out using a pinhole model. Owing to small movements of the test section and a relatively large magnification, a large initial distortion of approximately 2–3 pixels was seen in the disparity map. The volume self-calibration (VSC) algorithm of Wieneke (2008) was applied to reduce the residual root-mean-square to approximately 0.02 pixels.

The minimum intensity of images was subtracted from each image, followed by normalization using the average image to increase the signal-to-noise ratio. The images were further improved by applying local intensity normalization over a window with a kernel of 10 pixels, and a Gaussian smoothing with a kernel of 3 pixel $\times$ 3 pixel was used to avoid any peak locking (Kähler et al., 2012). An optical transfer function (OTF) was obtained and used for every iterative particle reconstruction step and the shaking algorithm as described by Schanz et al. (2012). We limited the largest particle shift between two successive image frames to 13 pixels and allowed a maximum triangulation error of 0.5 pixels. Particles closer than 1 pixel were eliminated to prevent any erroneous particle trajectories.

To reduce the noise of particle trajectories and obtain the Lagrangian velocity and acceleration, polynomials with different orders and different kernel sizes can be fitted on the measured particle position. Gesemann et al. (2016) applied a B-spline regression for noise reduction of STB data. Their regression method optimized the B-spline using a cost function assuming that the third derivative of particle position with respect to time (jolt) has a white noise distribution. In the current investigation, we applied a simpler method using a second-order polynomial fitted to each component of particle location (i.e., x, y, and z). The optimum polynomial kernel size is also based on the root-mean-square of acceleration (a^+_{rms}) as suggested by Voth et al. (2002).

In Figure 4.3a, (a^+_{rms}) is estimated at different wall-normal locations for a wide range

of kernel sizes, shown in time steps of $\Delta t = 250$ μs. According to Voth et al. (2002), an initial linear increase of (a^+_{rms}) (in a semi-log presentation) should be observed when the kernel size reduces. As the kernel further reduces to a certain limit, (a^+_{rms}) rapidly increases and deviates from the linear trend. The kernel size (t_k) at which (a^+_{rms}) deviates by 10% from the linear trend is selected as the optimum kernel. For instance, in Figure 4.3a, (a^+_{rms}) at $y^+ = 70$ follows a linear trend until t_k reduces to 25 time steps. The optimum t_k is estimated for different wall-normal locations and is presented in Figure 4.3b. The optimum size varies from $t_k = 70$ time steps (70×250 μs) at $y^+ = 10$ to $t_k = 25$ time steps (25×250 μs) at $y^+ = 70$. Summary of the 3D-PTV processing parameters is shown in Table 4.4.

It is important to note that there is a steep wall-normal velocity gradient: the near-wall particles move by ~ 1 pixel ($\sim 2u_\tau$ at $y^+ = 2$) while the particles away from the wall move up to 11 pixels between two consecutive image frames ($\Delta t = 250$ μs). Therefore, more time steps are required for the near-wall particles to have a similar displacement (i.e., kernel length in pixels or millimetres) as the faster particles away from the wall.

Parameter	Dimensions	Value
Magnification	...	0.56
Digital resolution	μm/pix	35.3
Measurement domain	mm^3	$21 \times 21 \times 2$
Recording rate	kHz	4
Number of images	...	14,490
Remove Close Distance	pixel	1
Max. Particle Displacement	pixel	13
Allowable Triangulation Error	pixel	0.5
Max. Abs. change in particle shift	pixel	1
Max. relative change in particle shift	%	20
Order of fit	...	2
Length for fit	...	70-25

Table 4.4: Summary of the 3D-PTV processing parameters

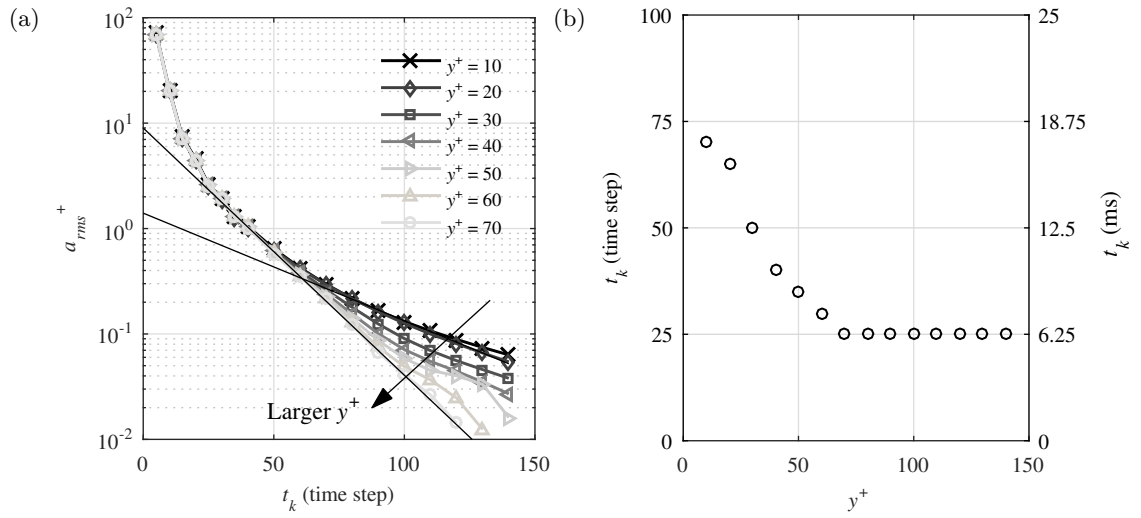

Figure 4.3: (a) Variation of (a^+_{rms}) with kernel size (t_k) at different wall-normal locations. The solid straight black lines are fitted to $y^+ = 10$ and 70 data, showing that the (a^+_{rms}) estimation deviates from the linear model at $t_k = 70$ and 25, respectively. (b) The estimated optimum t_k in time steps (left axis) and in milliseconds (right axis).

4.3.3 Uncertainty evaluation

The sources of uncertainty for the 3D-PTV measurement system are discussed here, including the precision of estimating wall location, the tracers response time, and the noise of particle trajectories.

The wall-normal location of each surface is estimated by applying the multiplicative algebraic reconstruction technique (MART) to the minimum image of the ensemble of images. The minimum intensity image includes small surface glares as shown in the red ellipse of Figure 4.4a. The intensity of the reconstructed surface glares is summed in the $z-$direction and shown in Figure 4.4b. Then the intensity profile of the glare points is projected on the $y-$axis as displayed in Figure 4.4b. A Gaussian distribution is applied over the intensity profile of Figure 4.4c to estimate the wall location. A subpixel accuracy of 0.1 pix is estimated for this Gaussian fit, similar to particle peak detection.

Figure 4.5 shows the instantaneous streamwise velocity of the tracers versus the wall-normal location for the 3D-PTV over a no-slip surface. As can be seen, the instantaneous streamwise velocity of the detected trajectories by STB is limited to $\sim$0.05 m/s. The large

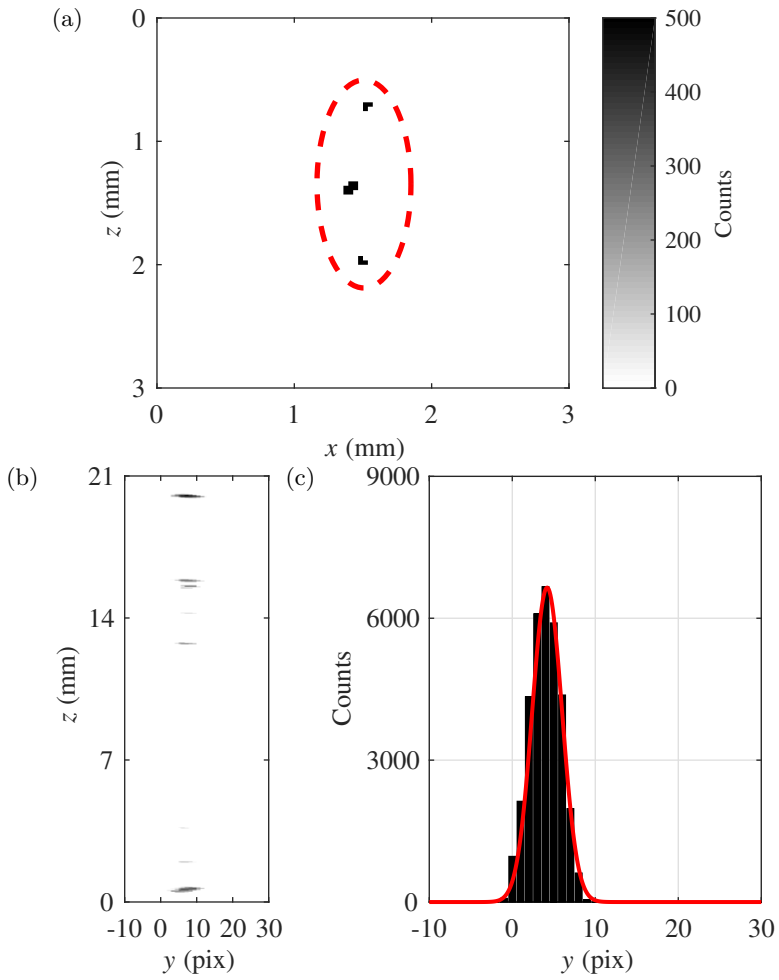

Figure 4.4: (a) A small section of the minimum intensity of the ensemble of images. The red dashed ellipse shows a few surface-glare points. (b) The sum of the intensity for the surface glares along the $z-$direction. (c) Intensity profile of the reflection points also summed in the $y-$direction and fitted with a Gaussian distribution.

size of the fluorescent tracers ($d_t = 10$ μm) and their slow decelerating response at the wall could case this limitation. To advance the understanding of this limitation, Stokes number (St) near and away from the wall is estimated by

$$St = \frac{\tau_T}{\tau_e}, \tag{4.1}$$

here τ_T is the tracers response time expressed as

$$\tau_T = \frac{(\rho_T - \rho)d_t^2}{18\mu}. \tag{4.2}$$

Where ρ_T is the tracers density (= 1510 kg/m^3 for the fluorescent tracers). In Equation 4.1, τ_e is the characteristic time of energy containing eddies $\tau_e = \kappa y^+ \nu / u_\tau^2$ (Righetti and Romano, 2004). The estimated St varied from 0.02 at $y = 0.03$ mm to $2{\times}10^{-4}$ at $y = 2$ mm (the upper edge of the measurement domain). Raffel et al. (2007) reported that tracers with $St \sim 0.06$ lose fidelity of flowing the flow, thus tracers at $y < 0.03$ mm of the current work may be uncoupled from the fluid motion. Henceforth, the lower limit of the 3D-PTV measurement in this thesis is at $y = 0.03$ mm.

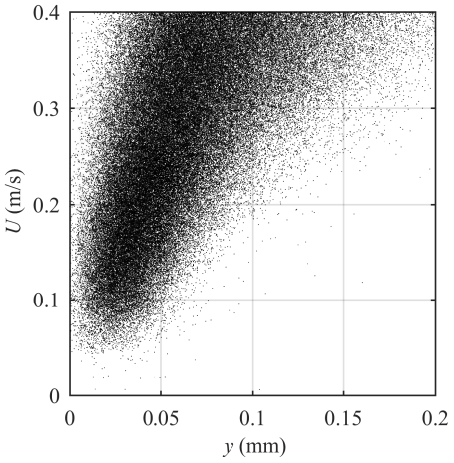

Figure 4.5: Scatter plot of the streamwise velocity of the tracers from 3D-PTV without the polynomial filter.

The $x-$, $y-$ and $z-$components of a trajectory before and after applying the second-order polynomial filter are shown in Figure 4.6. The trajectory is at average wall-normal locations of $y = 0.16$ mm (12λ) with t_k of 60. As shown in Figure 4.6a, the raw trajectory in the $x-$direction is smooth and the regression filter has a negligible effect. The trajectory in the $y-$direction is relatively noisy in Figure 4.6b as it is the out-of-plane motion for the cameras. However, the second-order polynomial filter can capture the motion and reduce the noise. The trajectory in the $z-$ direction in Figure 4.6c has relatively low, negligible, noise compared with the $y-$component. However, the second-order polynomial filter also captured the motion and reduced the noise. The velocity of the particle is obtained from the coefficient of the second-order polynomial in the central part of the trajectory, where

the full t_k can be applied. This central part is shown with a solid line in Figure 4.6.

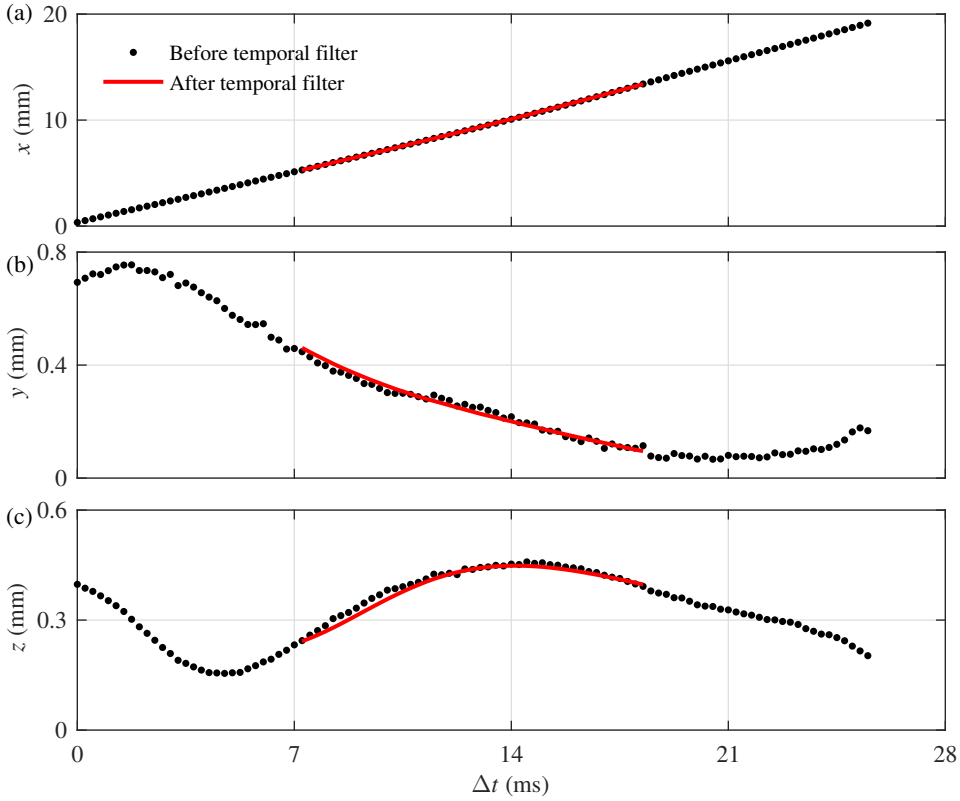

Figure 4.6: A particle trajectory before and after applying the regression in the (a) $x-$, (b) $y-$ and (c) $z-$directions. The trajectory is at an average wall-normal location of $y = 0.16\,\text{mm}$.

The performance of the second-order temporal filter is evaluated here by plotting the pre-multiplied linear spectral density (LSD) of the $x-$, $y-$ and $z-$components of the particle trajectories (Gesemann et al., 2016). The pre-multiplied LSD for the trajectories with and without the temporal filter is plotted as a function of frequency in Figure 4.7. Frequency (f) is normalized using the Nyquist frequency (f_N). The LSD profiles with and without the regression filter overlap at low frequencies until a cross-over frequency. Beyond this cross-over frequency, the LSD of trajectories without the temporal filter becomes flat (white noise). The estimated cross-over frequency is at approximately 1100, 1200, and 300 Hz for the $x-$, $z-$ and $y-$components. This results in an estimated noise wavelength of 3.6, 11.4 and 3.3 time steps (Δt) based on the acquisition frequency of 4000 Hz. The flat region also

corresponds to pre-multiplied LSD values of 3.5, 3.2, and 7 μm, which are equivalent to 0.1, 0.1, and 0.2 pixel in the $x-$, $z-$ and $y-$directions, respectively. This estimated uncertainty of particle position agrees with the expected accuracy for the in-plane and out-of-plane components of particle tracking methods before applying a temporal filter. The temporal filter has a negligible effect on the low-frequency content while it significantly reduces the random noise of higher frequencies as seen in Figure 4.7.

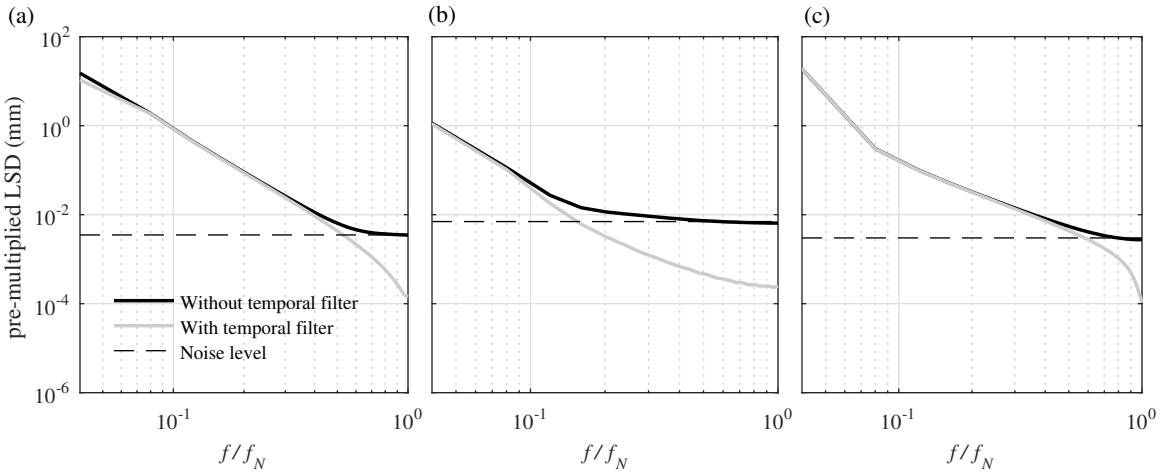

Figure 4.7: Pre-multiplied LSD of the $(a)x-$, $(b)y-$ and $(c)z-$components of particle position with and without the temporal filter.

The measurement noise of the 3D-PTV system is also evaluated using statistical convergence of the turbulence parameters. Figure 4.8 shows the statistical convergence of U^+, W^+, and the four components of $\langle u_i u_j \rangle^+$ at $y^+ = 40$ over the smooth surface. The U^+, W^+, and $\langle u_i u_j \rangle^+$ data are averaged over bins with 10, 30, and 50 μm length in the wall-normal direction, respectively. The horizontal axis of Figure 4.8 shows the number of data points (n) normalized with the total number of data points (N). It is seen in Figure 4.8a that U^+ quickly reaches statistical convergence. The difference of the minimum and maximum values (peak-to-peak) of average U^+ in the last 20% of the data $(n/N = 0.8 - 1)$ is 0.06%.

Figure 4.8b shows a larger range of noise of 0.40% based on peak-to-peak value for W^+. Figure 4.8c and 4.8d show that $\langle u^2 \rangle^+$ and $\langle v^2 \rangle^+$ converge at $n/N = 0.8$ with 0.40% and 0.30% random noise, respectively. The largest peak-to-peak noise is observed for $\langle w^2 \rangle^+$

and is 0.50% as seen in Figure 4.8e. The average $\langle uv \rangle^+$ in Figure 4.8f converges faster than $\langle u^2 \rangle^+$ and $\langle v^2 \rangle^+$, with 0.46% peak-to-peak noise between $n/N = 0.8$ and 1. The evaluation of the random noise for the 3D-PTV measurement of the mean velocities and Reynolds stresses over the smooth surface is summarized in Table 4.5. The percentages of peak-to-peak variation based on statistical convergence at the three wall locations of $y^+ = 15, 30,$ and 45 are presented in Table 4.5. The noise level reduces by moving away from the wall where the displacement of the particles is larger, and the fluctuations are smaller.

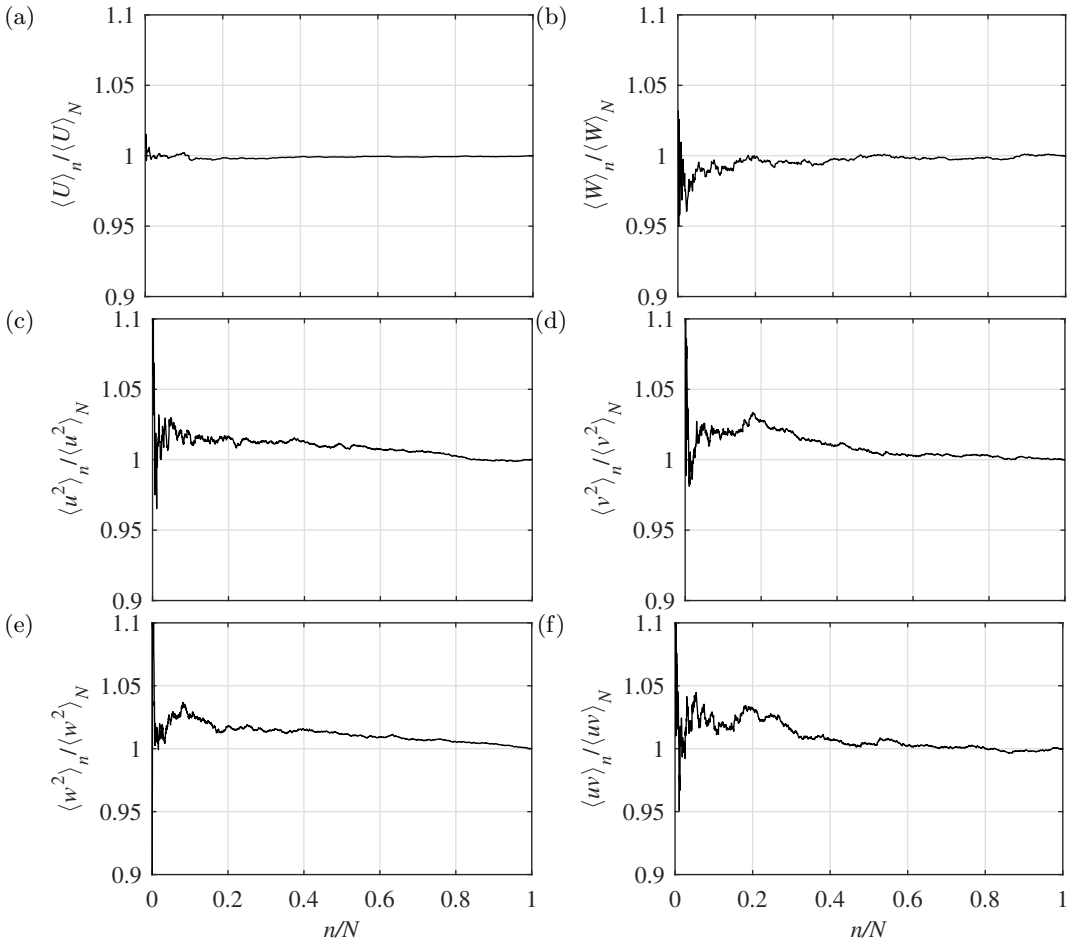

Figure 4.8: Statistical convergence of $(a)U_0^+, (b)W_0^+, (c)\langle u^2 \rangle_0^+, (d)\langle v^2 \rangle_0^+, (e)\langle w^2 \rangle_0^+,$ and $(f)\langle uv \rangle_0^+$ over the smooth surface at $y^+ = 40$ Each component of the mean velocities and Reynolds stress tensors is normalized by its own mean tensor at $y^+ = 40$.

The number of data points versus the wall-normal location for 10, 30 and 50 μm bins (75% overlap) is shown in Figure 4.9. The 10, 30 and 50 μm bins are used to obtain

$\langle U \rangle, \langle |W| \rangle$ and $\langle u_i u_j \rangle^+$, respectively. The average number of data along y^+ for the 10, 30 and 50 μm bins is $1.7 \times 10^4, 5.4 \times 10^4$, and 9.3×10^4, respectively.

As presented above, the lower limit of the current 3D-PTV measurement is 0.03 mm due to the tracers velocity lag below this location. The sources of uncertainty are a subpixel (0.1-pixel) error due to the wall location detection and 0.1, 0.1, and 0.2 pixels for $x-, z-$, and $y-$components, respectively, after applying the temporal filter. The summation of these errors can be estimated using propagation of uncertainties. The total uncertainty in the $x-, z-$, and $y-$directions is 0.005 mm (20.0 mm/s), 0.005 mm (20.0 mm/s), and 0.008 mm (31.7 mm/s), respectively. It is worth mentioning that uncertainty from estimating the wall location has more effect on the parameters that an estimated at the wall (e.g. slip velocity, slip length, and fiction velocity).

Parameter	$y^+ = 15$	$y^+ = 30$	$y^+ = 45$
$\langle U \rangle^+$	0.60%	0.11%	0.06%
$\langle W \rangle^+$	0.51%	0.31%	0.24%
$\langle u^2 \rangle^+$	0.77%	0.60%	0.28%
$\langle v^2 \rangle^+$	0.90%	0.54%	0.30%
$\langle w^2 \rangle^+$	0.91%	0.52%	0.48%
$\langle uv \rangle^+$	0.82%	0.68%	0.44%

Table 4.5: Random noise of the mean velocities and Reynolds stresses over the smooth surface at $y^+ = 15, 30$ and 45.

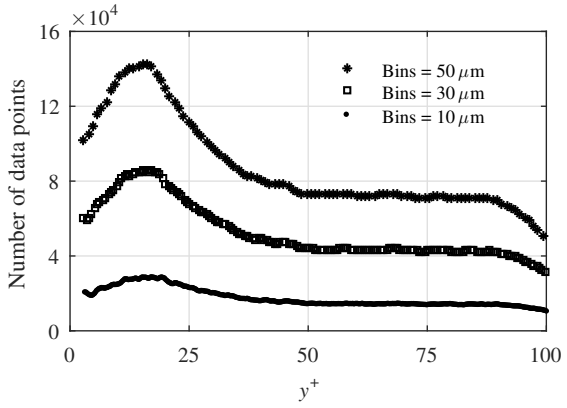

Figure 4.9: Number of data points for three different bin sizes along the $y-$axis.

4.4 Time-resolved 2D particle tracking velocimetry

Time-resolved 2D particle tracking velocimetry (2D-PTV) was used for measurement of slip length and velocity in Chapters 7 due to application of small tracer particles (5 μm tracers) and the possibility to directly obtain the wall location from the PTV images.

4.4.1 Apparatus

The flow at the mid-span of the channel of flow facility 2 in Section 3.2 is characterized using a high-magnification 2D-PTV with FOV of 4.7×6.2 mm^2 in $x-$ and $y-$directions, respectively. The illumination source is a dual-cavity Nd: YLF laser (DM20-527, Photonics Industries) with 20 mJ/pulse at a wavelength of 532 nm. Using a combination of cylindrical and spherical lenses, the laser beam is shaped into a laser sheet with 1 mm thickness in the $z-$direction and 5 mm width in the $x-$direction, as shown in Figure 4.10. The flow is seeded with polyamide particles (VESTOSINT 2070) with an average diameter of 5 μm and a density of 1.016 g/cm^3. A high-speed Phantom v611 camera with 1280×800 pixel CMOS sensor images the reflected light from the tracers. Each CMOS pixel is 20×20 μm^2 with 12-bit resolution. The camera is equipped with Nikon 60 mm lens at an aperture size of $f/11$. The lens is connected to an 80 mm extension tube resulting in a final magnification of 2.2 and digital resolution of 8.8 μm/pix. The laser pulses and the camera are synchronized using a high-speed controller (PTU X, LaVision, GmbH) controlled by DaVis 8.2. Six sets of 2,048 single-frame images (12,288 images in total) are collected at a frequency of 10 kHz.

4.4.2 Image processing

The signal-to-noise ratio of the images is improved by subtracting the minimum intensity of the ensemble of images. Following this step, the images are normalized using the average intensity of the ensemble of images and further improved using a bandwidth filter with a kernel of 3 to 7 pixels. Particles below a specified intensity threshold and particles that are smaller than 2 pixels or larger than 6 pixels are discarded to avoid out-of-focus particle images. The 2D-PTV algorithm in DaVis 8.4 is used to track the in-focus particles based on

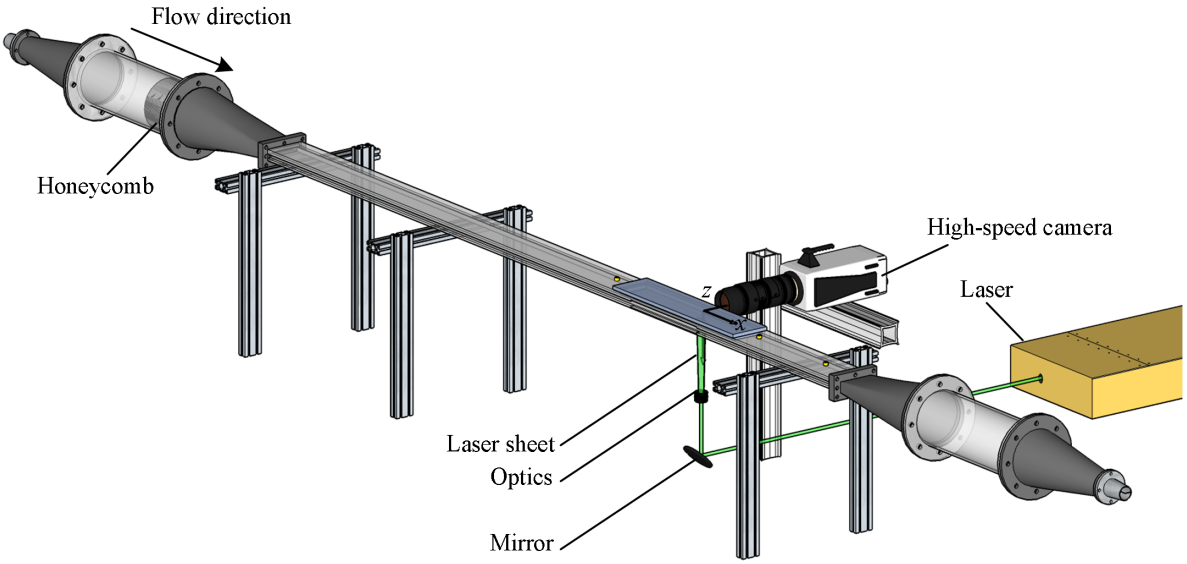

Figure 4.10: Schematic of the experimental set-up for the 2D-PTV experiment.

an initial velocity predictor obtained from the ensemble of correlations of the time-resolved images (Meinhart et al., 2000). To reduce the random noise of the particle position, a second-order polynomial with a constant kernel size of 20-time steps is applied. Parameters for the 2D-PTV measurement system are listed in Table 4.6.

Parameter	Dimensions	Value
Magnification	...	2.2
Digital resolution	μm/pix	8.8
Measurement domain	mm^2	4.7×6.2
Recording rate	kHz	10
Number of images	...	12,288
Min. Particle Size	pixel	2
Max. Particle Size	pixel	6
Order of fit	...	2
Length for fit	...	20

Table 4.6: Summary of the 2D-PTV parameters

4.4.3 Uncertainty evaluation

Two sources of uncertainty are considered for the 2D-PTV system. The first source is the error of the tracers peak detection and the second source is the uncertainty of detecting the wall location. As presented above, the error the tracers peak detection can be estimated from the 0.1-pixel assumption which is equivalent to 8.8 mm/s.

The accuracy of the estimated wall location in PTV images strongly affects the estimated slip velocity and slip length over the SHS. To estimate the wall location, the glaring line, formed by the reflection of the laser light, is averaged over all the images as shown in Figure 4.11a. The image is then averaged in the $x-$direction to obtain the intensity profile of Figure 4.11b. The location of peak intensity in the wall-normal direction (y) is considered as the wall location. The uncertainty of the estimated wall location from this technique is evaluated based on the radius of the intensity profile at $1/e^2$ ($\sim 13.5\%$) of the peak value, which is equal to ± 25 μm. This method of estimating the wall location resulted in the uncertainty of obtaining the friction velocity and wall unit by up to 5×10^{-3} m/s and 1.3 μm, respectively. The estimation of the slip velocity and slip length from the 2D-PTV measurement over the SHS were also varied by about 0.04 m/s and 9.1 μm, respectively. Henceforth, the slip length and slip velocity from the 2D-PTV measurement over the SHS are reported with the uncertainty of estimating the wall location for each case. The 2D-PTV were averaged in 10 μm bins with 50% overlap in the $y-$direction to obtain the mean velocity profile.

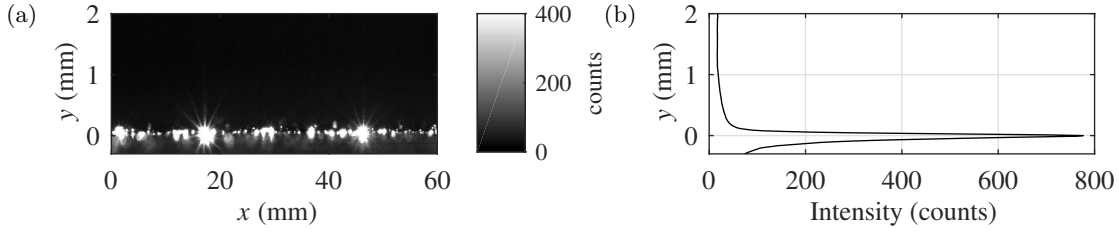

Figure 4.11: (a) Average of PTV images showing the region near the SHS. The glare line is due to reflection of the laser sheet from the SHS. (b) The intensity profile after averaging the image in the x direction.

4.5 Pressure measurement

The previous experiments of Lei et al. (2009); Ling et al. (2016); Gose et al. (2018) observed that high pressure can push the air layer into the cavities of the SHS and expose the peaks of the roughness elements to the turbulent flow, reducing the DR performance of the SHS. Dilip et al. (2014) reported that the increase of the pressure over the SHSs can increase the solubility of water dissolving part of the air layer in water. Ling et al. (2016) carried out experiments over an SHS at two different hydrostatic pressures (98 kPa and 122 kPa). They concluded that the air layer over the SHS is compressed inside the roughness elements at the higher pressure while it is maintained at the lower pressure. Recently, the shadowgraphy particle tracking velocimetry measurement of Reholon and Ghaemi (2018) was carried out at atmospheric pressure on a body of revolution sprayed with a superhydrophobic coating. They showed that the air layer over the SHS at the tested hydrostatic pressure was relatively flat and covered all the roughness elements except for the large roughness peaks which are exposed to the flow. Thus, in the current work, the absolute pressure over the tested SHS is monitored to ensure that the absolute pressure over the test surfaces is below the atmospheric pressure. In this work, DR is also estimated from a pressure drop measurement.

4.5.1 Apparatus

The absolute pressure inside the loop is measured by a pressure transducer (Validyne 0.5 psi diaphragm) and maintained below the atmospheric pressure at 97 kPa. The pressure difference (dP) over the test surface is also monitored using another pressure transducer (P15, Validyne) with a 0.2 psi diaphragm. The latter transducer is connected to two pressure ports upstream and downstream of the test surface with a distance of 276 mm ($46H$). The pressure ports locations are as shown in 3.3. Each pressure traducer is connected to a demodulator (CD15, Validyne) to amplify the signal. The demodulators communicate with the developed program in LabVIEW 2015 (National Instruments) through a data acquisition module (NI USB-6001, National Instruments) for data sampling.

4.5.2 Uncertainty evaluation

The DR over the SHS is directly measured using pressure drop measurements according to DR $= 2.16 \times \frac{dp_0 - dp}{dp_0}$. Here, dp_0 and dp are the pressure drop measurements over the smooth and SHS, respectively. The factor 2.16 is included since the SHS covers 46% of the channel surface area between the two pressure ports (see Figure 3.3). The uncertainty of the pressure drop measurement is approximately 2% based on six repeated measurements over the smooth surface. The error in DR is estimated following the error propagation as

$$DR = 2.16 \times \frac{(dp_0 \pm 0.02dp_0) - (dp \pm 0.02dp)}{(dp_0 \pm 2\%)}. \tag{4.3}$$

$$DR = 2.16 \times \frac{(dp_0 - dp \pm (0.02dp_0 + 0.02dp))}{(dp_0 \pm 2\%)}. \tag{4.4}$$

$$DR = 2.16 \times \frac{\left(dp_0 - dp \pm 2\frac{dp_0 + dp}{dp_0 - dp}\%\right)}{(dp_0 \pm 2\%)}, \text{or} \tag{4.5}$$

$$DR = \left[2.16 \times \frac{dp_0 - dp}{dp_0}\right] \pm \left[2.16 + 2 \times \frac{dp_0 + dp}{dp_0 - dp}\right] \times \left[2 \times \frac{dp_0 - dp}{dp_0}\right] \tag{4.6}$$

In Chapters 6 and 7, the uncertainty in estimating the DR from the pressure drop measurement is evaluated using Equation 4.6.

Chapter 5

Inner and outer layer turbulence over a superhydrophobic surface

5.1 Introduction

There has been recently a large number of investigations that characterized turbulent flows over SHSs. The particle image velocimetry (PIV) of Zhang et al. (2015) in a boundary layer observed a significant increase of mean streamwise velocity extended up to the boundary layer edge. Woolford et al. (2009a); Vajdi Hokmabad and Ghaemi (2016) showed comparable mean velocity profiles over an SHS and a no-slip smooth in turbulent channel flow. The theoretical study of Fukagata et al. (2006) suggested an increase of mean velocity in the vicinity of the wall as a result of the slip and a reduction of the mean velocity further away from the SHS when compared with that over the no-slip smooth surface. This is consistent with the DNS of Min and Kim (2004) over a flat surface with an imposed slip boundary condition. Daniello et al. (2009) observed higher near-wall velocity over an SHS as Re increased based on a PIV measurements, although direct comparison with a baseline smooth surface and the spatial resolution of their PIV system were not provided. To the author's knowledge, Ling et al. (2016) is the only experimental work that measured the streamwise slip velocity. Ling et al. (2016) carried out an experiment over SHSs with a wide range of k^+ from 0.43 to 3.3 (where k^+ is the root-mean-square of wall roughness normalized by wall-unit) in a turbulent boundary layer using digital holographic microscopy (DHM). They reported up to 36% DR over an SHS with $U_s = 0.73$ m/s at a bulk velocity

of 2.0 m/s. However, there is no experimental investigation that characterized the flow over an SHS with low roughness ($k^+ < 0.4$).

To understand the mechanism of the skin-friction reduction over SHSs with low roughness, the inner and outer layers of a turbulent channel flow over an SHS with ($k^+ < 0.2$) were characterized using simultaneous long-range micro-PTV and PIV introduced in Section 4.2 and 4.1, respectively. The objective from this work is to measure the slip velocity and length over the SHS in the streamwise direction. This investigation also aims to study the effect of the SHS on the Reynolds stresses and skin-friction.

5.2 Results

Details about the turbulent channel flow used in this chapter are included in Section 3.1. The velocity averaged along the y-direction and the maximum streamwise velocity at the center of the channel are $U_b = 0.174$ m/s and $U_{max} = 0.205$ m/s, respectively. The flow rate is kept constant in the flume using an orifice flow meter with an estimated time-averaged variation of ± 0.002 m/s in U_b based on repeating the experiments. The Reynolds number based on the full channel height (H) is 4400. The estimated friction velocity is $u_{\tau 0} = 0.0113 m/s$, while the wall unit (viscous length scale) is $\lambda_0 = \nu/u_{\tau 0} = 88.8 \mu$m based on the PTV measurements over the smooth acrylic wall as detailed in Section 4.2. The friction Reynolds number based on the half channel height is $Re_\tau = u_\tau H/2\nu = 140$. The analysis is also carried out at a constant flow rate, which results in different Re_τ over the two surfaces. This relatively low Re is chosen to obtain a larger wall unit and improve the relative spatial-resolution of the measurement system in the vicinity of the wall (Kim et al., 1987). The channel dimensions and flow condition are summarized in Table 5.1.

Statistical characterization of the turbulent flow is presented over the superhydrophobic surface (denoted SHS) and the flat acrylic surface (denoted smooth). The SHS and smooth surfaces are placed at the top wall where $y/H = 0$ while the bottom surface is at $y/H = 1$. The bottom surface is always a glass surface in both the SHS and smooth experiments.

Parameter	Dimensions	Value
Channel dimensions ($H \times W \times L$)	mm	$25 \times 540 \times 3000$
U_b	m/s	0.174
U_{max}	m/s	0.205
Re	...	4400
$u_{\tau 0}$	m/s	0.0113
λ_0	μm	88.8
Re_τ	...	140

Table 5.1: The geometric dimensions and flow statistics of the turbulent channel flow. The velocities U_b and U_{max} are measured using PIV, while $u_{\tau 0}$ and λ_0 are obtained using micro-PTV

5.2.1 Mean velocity

The semi-logarithmic presentation of normalized mean streamwise velocity ($u^+ = \langle U \rangle / u_\tau$) over the smooth surface obtained from micro-PTV and PIV using EOC method is shown in Figure 5.1a. The PTV profile is in agreement with both the law of the wall ($u^+ = y^+$) in the linear sublayer ($y^+ < 5$) and the logarithmic law ($u^+ = \frac{1}{\kappa} ln(y^+) + B$) profile with $\kappa = 0.39$ and $B = 5.5$. The overlap indicates a fully developed turbulent channel flow. There is a small discrepancy between the PIV data and PTV data up to $y^+ \sim 20$ which is associated with bias errors in the near wall PIV measurement. The large PIV interrogation window is the main cause of bias error in the buffer layer where the velocity gradient is large. Closer to the wall and in the viscous sublayer, the mirrored particle images, signal truncation, and the glare of the laser sheet in the near wall interrogation windows are also associated with near-wall error of PIV measurement (Theunissen et al., 2008). The closest data point with no apparent bias error in Reynolds stresses from the PIV measurement is at $y^+ \sim 15$. An investigation of the PIV data using the indicator function, $\zeta^+ = y^+ + \frac{\partial u^+}{\partial y^+}$, shows that the log-law is relatively narrow (Elbing et al., 2013; White et al., 2012). The log-law is limited to y^+=50 to 110 based on the flat section of ζ^+ with an assumption of 10% variation.

The profile of $\langle U \rangle$ over the smooth and SHS surface across the channel measured using PIV (EOC method) are shown in Figure 5.1b. The data is normalized using bulk velocity (U_b) over the corresponding surface. The profile of the smooth surface shows a good

symmetry as shown by comparison with the flipped axis profile shown with dashed line in Figure 5.1b. The SHS and smooth profiles overlap across the channel showing no considerable macroscopic difference between the velocity profiles within the spatial-resolution and near-wall limitations of the PIV system. The overlap across the bottom side of the channel over the glass surface ($y/H > 0.5$) shows repeatability of the measurements. Vajdi Hokmabad and Ghaemi (2016) also observed overlap of $\langle U \rangle$ over a smooth and SHS away from the wall at $y^+ > 10$. Their measurement closer to the wall and in particular within $y^+ < 5$ (linear viscous sublayer) was biased due to the strong glare of the laser light from the SHS. PIV measurements of Woolford et al. (2009a) over an SHS manufactured by photolithography (24 μm wide longitudinal cavities) also showed no discernible difference at $0.02 < y/H < 0.2$ while they observed a slightly flatter $\langle U \rangle$ (smaller velocity) over the SHS in the channel core ($0.4 < y/H < 0.6$).

Scrutiny of the near-wall velocity is carried out using the long-range micro-PTV measurement. The velocity of individual PTV tracers ($U^+ = U/u_\tau$) over the smooth surface and SHS in the inner layer ($y^+ < 35$) are shown in Figure 5.2a and 5.2b, respectively. The mean velocities obtained from averaging the particle velocities in bins with $(\Delta x, \Delta y) = 56.9^+ \times 0.44^+$ dimensions are also shown in these figures. The presence of the no-slip boundary condition is evident over the smooth surface as the mean velocity approaches zero at the wall ($y^+ = 0$). The detected tracers also have a negligible velocity in the immediate vicinity of the smooth wall. There is a large number of particles with finite velocity $1 \leq U^+ \leq 4$ (0.011 m/s $\leq U \leq$ 0.044 m/s) at the immediate vicinity of the SHS. The estimated mean slip velocity is $U_s = 0.023$ m/s ($U^+ = 2.1$) at $y^+ = 0$ over the SHS which is about 13% of the bulk velocity (U_b). Ling et al. (2016) reported slip velocities in the order of 14.5 to 36.5% of U_b (0.29 to 0.73 m/s or 3.2^+ to 9.6^+) on different SHSs with k^+ ranging from 0.43 and 3.28. Ou et al. (2004) observed a slip velocity with $0.6U_b$ magnitude over ultra-hydrophobic surface in a laminar micro-channel.

The mean profile obtained using sliding average over the velocity of tracers is shown in Figure 5.2c to scrutinize the gradient and the slip length over the smooth and SHS surfaces.

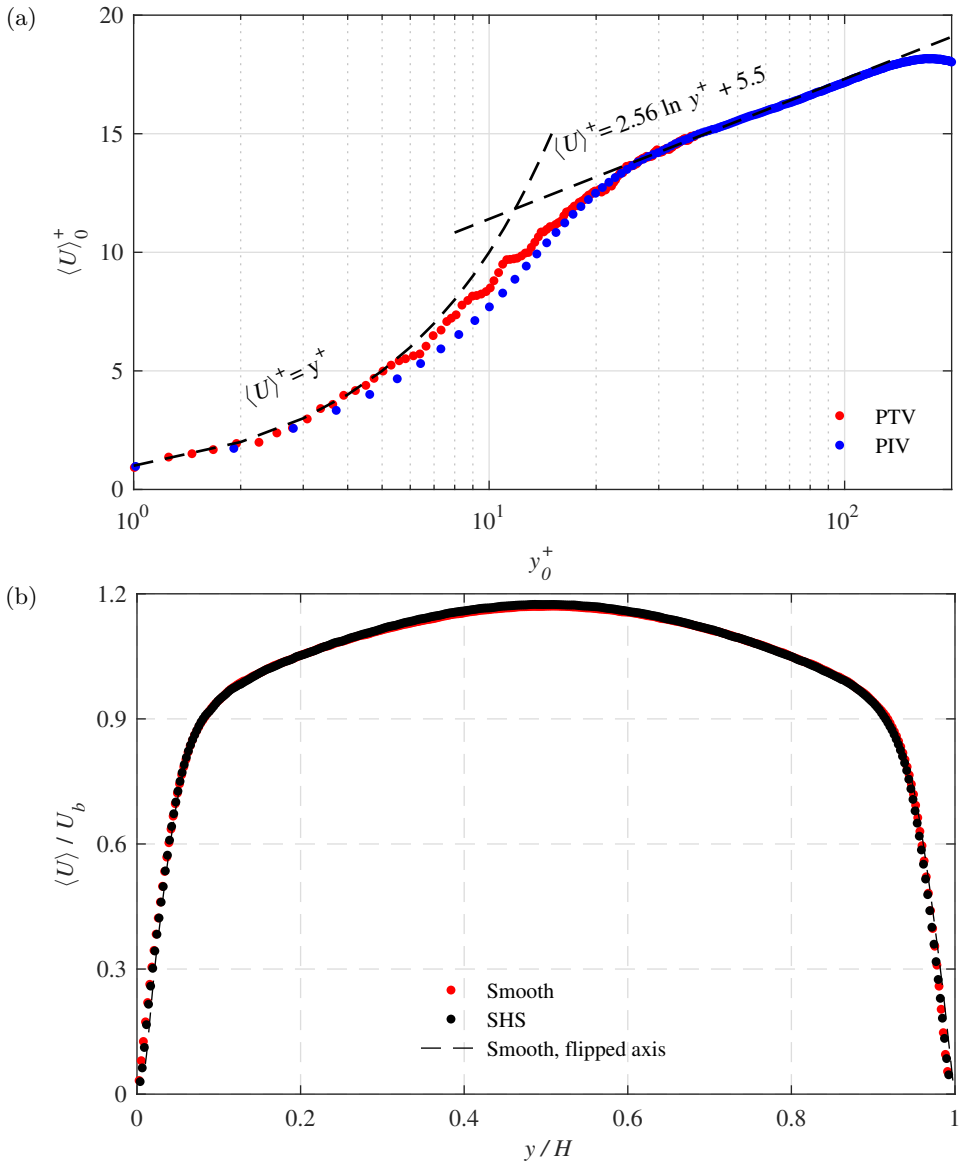

Figure 5.1: (a) Mean velocity profile over the smooth wall (no-slip wall) obtained from the micro-PTV and PIV (using EOC). (b) Mean streamwise velocity over the smooth and SHS obtained using PIV.

The velocity gradient $\frac{\partial\langle U\rangle}{\partial y}$ of the viscous sublayer ($y^+ < 5$ with 20 data points) reduces by about 19% over the SHS as shown by the fitted lines in Figure 5.2c. As a result, the friction velocity over the SHS reduces to 0.0102 m/s and the corresponding $Re_\tau = 127$. This value is similar to the 18% DR reported by the DNS of Rastegari and Akhavan (2015) with an assumed slip velocity of $U_s = 0.15U_b$. The $\frac{\partial\langle U\rangle}{\partial y}$ estimation over the SHS results in an effective slip length of about $l_s = 200$ μm (2.2^+). The accuracy of the wall location (available in Table 3) is about 0.06^+ and does not affect the estimated effective slip length. The u^+ over the smooth surface is smaller than that of the SHS at $y^+ < 10$ as observed in Figure 5.2c. The theoretical work of Fukagata et al. (2006) also predicts an increase in $\langle U\rangle$ in the vicinity of the wall as a result of the wall slip while $\langle U\rangle$ reduces further away from the wall to conserve the mass flow. The DNS of Jung et al. (2016) also shows evidence of an increase in the mean velcoity in the near wall region ($y/H < 0.2$) with increase of the air-layer thickness, while a reduction of mean velocity is observed further away from the wall. The holographic measurements of Ling et al. (2016) in the inner layer also indicated an increase in the near-wall mean velocity.

Figure 5.2d shows semi-logarithmic plots of mean velocity profiles with subtracted slip velocity ($u^+ - U_s^+$) for the SHS relative to the smooth wall. The $u^+ - U_s^+$ over the SHS overlaps with the smooth surface profile in the viscous sublayer ($y^+ < 3$) while a downward shift of $u^+ - U_s^+$ with respect to the smooth wall is observed further away from the wall. The fitted logarithmic line over the SHS has a smaller B of 3.3. Min and Kim (2004) also confirm a downward shift in the buffer and log layers of the SHS when combined streamwise and spanwise wall slip is imposed in their DNS. The $u^+ - U_s^+$ versus y^+ of the smooth and the SHS collapsed when only a streamwise slip was applied in their DNS. This indicates the presence of a combination of streamwise and spanwise slip over the SHS of the current study with random texture. The DNS of Rastegari and Akhavan (2015) has also confirmed the downward shift of the log-layer and thinner buffer layer over the SHSs.

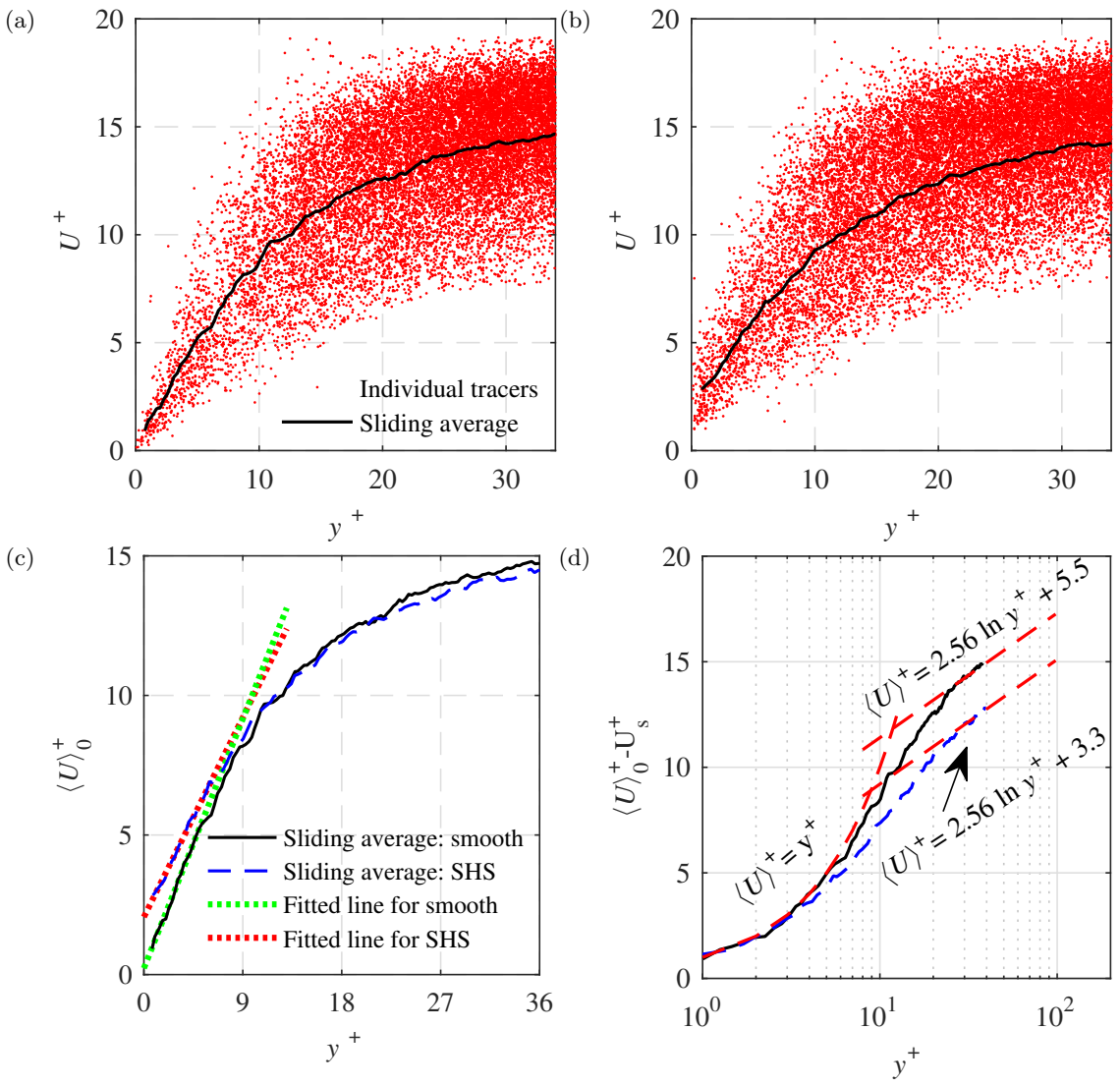

Figure 5.2: The velocity of tracer particles from micro-PTV over (a) smooth surface and (b) SHS. (c) The mean velocity over the smooth and SHS obtained from averaging the velocity of the tracer particles in bins with wall-normal dimension of 40 μm (0.44λ) and 75% overlap. (d) Semi-logarithmic representation of the mean velocity relative to the estimated slip velocity at the wall ($u^+ - U_s^+$).

5.2.2 Reynolds shear stress

The profiles of Reynolds shear stress $\langle uv \rangle$ across the channel are measured using planar PIV and plotted in Figure 5.3a. The measurement of the Reynolds shear stresses from micro-PTV in the near-wall region of $y^+ < 35$ is also shown in Figure 5.3b since the applied PIV system cannot resolve the smallest turbulent structures ($\sim 20^+ \sim 1.8$ mm) (Stanislas et al., 2008), since it is optimized to cover the full channel. The $\langle uv \rangle$ profile of the smooth wall in Figure 5.3a shows perfect symmetry when compared with the flipped profile shown as red solid line. A linear variation of $\langle uv \rangle$ over the smooth surface is observed in the mid-section ($0.2 < y/H < 0.7$) of the channel which confirms the fully developed state of the turbulent channel flow. The $\langle uv \rangle$ profiles of smooth and SHS overlap across the bottom half of the channel ($y/H = 0.5$ to 1) as the common glass wall is located at $y/H = 1$ for both cases. The $\langle uv \rangle$ profile from the DNS of Tsukahara et al. (2005) at $Re_\tau = 150$ is also shown on the lower half of the channel ($y/H = 0.5$ to 1) for comparison with the measurement over the flat surface. There is a small discrepancy between the measured data and the DNS which is attributed to the lower $Re_\tau = 140$ of the current work.

The intercept of the fitted line over the linear region $\langle uv \rangle$ profile in the upper-half of the channel (i.e., $y/H = 0.2$ to 0.5) with the wall $y/H = 0$ can be used to estimate the wall-shear stress (τ_w). The results show a 7.2% reduction of the intercept of the fitted line and consequently wall shear stress over the SHS. The uncertainty of this method to obtain the wall-shear stress is estimated according to Hou et al. (2017) using

$$\tau_w = \rho u_\tau^2 \left(1 \pm \frac{\varepsilon_{uv}}{0.6u_\tau^2}\right)\left(1 \pm \frac{\varepsilon_y}{0.5H}\right), \tag{5.1}$$

Here ε_{uv} is the error in the measurement of $\langle uv \rangle$ and is equal to $0.03u_\tau^2$ with the assumption of 0.1 pix uncertainty in the instantaneous velocity of PIV. The ε_y is the error in estimation of the location of the mid-channel and is assumed to be 0.5pix $\sim 0.18\lambda$. Equation 5.1 can be simplified as

$$\tau_w = \rho u_\tau^2 \left(1 \pm 0.05\right), \tag{5.2}$$

where the uncertainty of τ_w is about 5%. The peak value of $\langle uv \rangle$ is also reduced by about 7.4% over the SHS while its wall-normal distance stays at $y/H \sim 0.10$ (28^+) and within the spatial-resolution of the PIV system (17.6^+). The underestimation of DR relative to the previous estimation based on $\frac{\partial \langle U \rangle}{\partial y}$ of the micro-PTV is associated with relatively short length of the SHS surface ($22.8H$). Microscopic PTV measurement in Figure 5.3b shows that $\langle uv \rangle$ over the SHS is slightly larger than the smooth surface at $y^+ < 10$ while it becomes smaller further away from the wall beyond $y^+ > 10$. At $y^+ = 35$, $\langle uv \rangle$ over the SHS is $\sim 30\%$ smaller than that of the smooth surface. This is qualitatively in agreement with the outer layer PIV measurement of Figure 5.3a. PIV showed a reduction of $\langle uv \rangle$ peak over the SHS although it underestimated the reduction due to spatial-resolution limitations.

The PIV of Woolford et al. (2009a) showed overlap of $\langle uv \rangle$ profiles on the half of the channel where the common flat surface was located, while $\langle uv \rangle$ over the SHS becomes gradually smaller than that of the smooth surface with approaching the SHS wall. They observed about 8% reduction of $\langle uv \rangle$ peak intensity with no displacement of its location over the investigated SHS with 11% DR. Vajdi Hokmabad and Ghaemi (2016) observed a 15% reduction of $\langle uv \rangle$ peak intensity over their SHS with roughness of $k^+ = 0.11$ with a slight shift of the peak location away from the wall ($\sim 5\lambda$). The DHM of Ling et al. (2016) over SHSs with $k^+ = 0.43$, 0.62, and 0.89 showed a larger $\langle uv \rangle$ over the SHSs at $y^+ < 15$ followed by smaller $\langle uv \rangle$ over the SHS at $15 < y^+ < 100$. This trend is consistent with the current investigation although the increase of $\langle uv \rangle$ at $y^+ < 15$ over the rough SHSs of Ling et al. (2016) is larger. Ling et al. (2016) also observed an increase of $\langle uv \rangle$ across their measurement domain ($2 < y^+ < 200$) over SHSs with larger roughness of $k^+ = 1.71$ and 3.28.

The DR percentage is also estimated using the analytical expression provided by Rastegari and Akhavan (2015) for surfaces with slip velocity based on the initial formulation of Fukagata et al. (2002). They suggested DR is the summation of two terms, which includes slip velocity at the wall, and a weighted wall-normal integral of Reynolds shear stress. This

equation is expressed as

$$DR = \frac{U_s}{U_b} + \left(1 - \frac{U_s}{U_b}\right)\left(\frac{3\varepsilon}{1 - 3I^+}\right), \tag{5.3}$$

where $\varepsilon = I^{+0} - I^+$ is the difference between the integrals of weighted Reynolds shear stress over the smooth surface (I^{+0}) and SHS (I^+), respectively. I^+ is defined as

$$I^+ = \int_0^1 (1 - \delta)\langle uv\rangle^+ d\delta. \tag{5.4}$$

Here $\delta = 2y/H$ is the normalized wall-normal coordinate. The integrals are obtained within $\delta = 0.01$ to 0.16 (or from 1.4^+ to 22.5^+) using micro-PTV and continued from $\delta = 0.16$ to 1.0 (22.5^+ to 140^+) using PIV. The obtained DR from Equation 5.3 is 21.9% over the current SHS. The corresponding friction velocity and Re_τ are 0.010 and 125 m/s, respectively. This value of DR is close to the estimated DR of 19% obtained from the velocity gradient $\frac{\partial\langle U\rangle}{\partial y}$ as shown in Figure 5.2c.

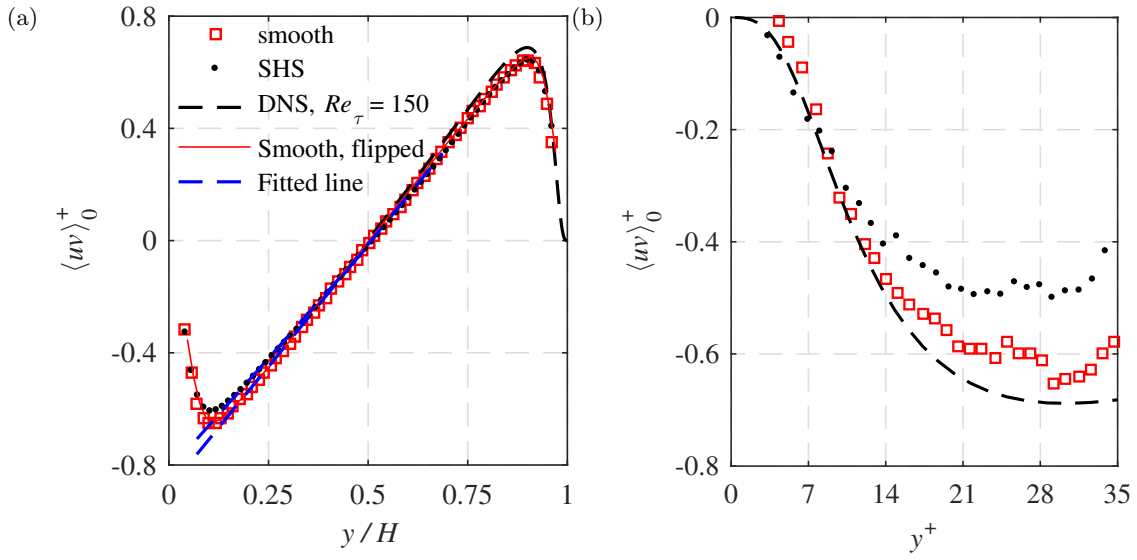

Figure 5.3: (a) Measurement of Reynolds shear stress using PIV over smooth and SHS across the full channel. The wall-normal distance is normalized using the channel height (H). The SHS surface is placed at $y/H = 0$ while the top wall at $y/H = 1$ is a smooth glass wall for both the smooth and SHS cases. The DNS data of Tsukahara et al. (2005) is provided for comparison over the bottom half of the channel. (b) Inner layer measurements of $\langle uv\rangle$ using micro-PTV.

5.2.3 Normal Stresses

The streamwise component of normal Reynolds stress, $\langle u^2 \rangle / u_\tau^2$, is obtained from the PIV and shown in Figure 5.4a to evaluate its distribution across the channel. DNS of Tsukahara et al. (2005) at $Re_\tau = 150$ is also shown in the lower half of the channel for comparison. The near-wall peak of $\langle u^2 \rangle$ is not captured due to the limited spatial-resolution of the current PIV. The $\langle u^2 \rangle$ profile of the smooth surface overlaps with the $\langle u^2 \rangle$ profile plotted with a flipped y/H axis. This shows the symmetry of the channel flow. No considerable difference is observed between $\langle u^2 \rangle$ profile of the smooth and SHS away from the walls at $y/H > 0.1$. The PIV of Vajdi Hokmabad and Ghaemi (2016) with slightly better spatial-resolution (14.6λ) showed smaller $\langle u^2 \rangle$ over the SHS with respect to the smooth surface until about $y^+ \sim 100$ followed by overlap of the profiles further away from the wall. The outer layer measurement of Woolford et al. (2009a) also showed 20% reduction in $\langle u^2 \rangle$ over the SHS at $y/H = 0.2$, which extends until $y/H = 0.8$ into the other half of the channel. The thickness and morphology of the plastron and the length of the SHS may have contributed to the observed differences of these outer layer measurements.

The inner layer measurement of $\langle u^2 \rangle$ within $y^+ < 35$ from micro-PTV over the SHS and the smooth surface is shown in Figure 5.4b. In the immediate vicinity of the wall at $y^+ < 7$, $\langle u^2 \rangle$ is lightly larger over the SHS relative to the smooth surface. The magnitude of the $\langle u^2 \rangle$ peak over the SHS and the smooth surface is similar. However, the location of the peak is closer to the wall over the SHS ($y^+ \sim 9.8$) compared to the smooth surface ($y^+ \sim 15.2$). Further away from the wall at $y^+ > 20$, $\langle u^2 \rangle$ over the SHS becomes comparable with the smooth wall. The DNS of Busse and Sandham (2012) also reported larger values of $\langle u^2 \rangle$ over SHS at about $y^+ < 10$ and an overlap with the smooth case at $y^+ > 10$ for an imposed streamwise effective slip length $l_s^+ > 0.6$. The DNS of Min and Kim (2004) demonstrated that $\langle u^2 \rangle$ over an SHS with both streamwise and spanwise slip is larger at $y^+ < 8$, while it becomes smaller at $8 < y^+ < 100$. The DNS of Rastegari and Akhavan (2015) over SHSs with longitudinal micro-grooves also observed larger $\langle u^2 \rangle$ at $y^+ < 7$ relative to the smooth surface. They associated it with the thinner buffer layer and the downward shift

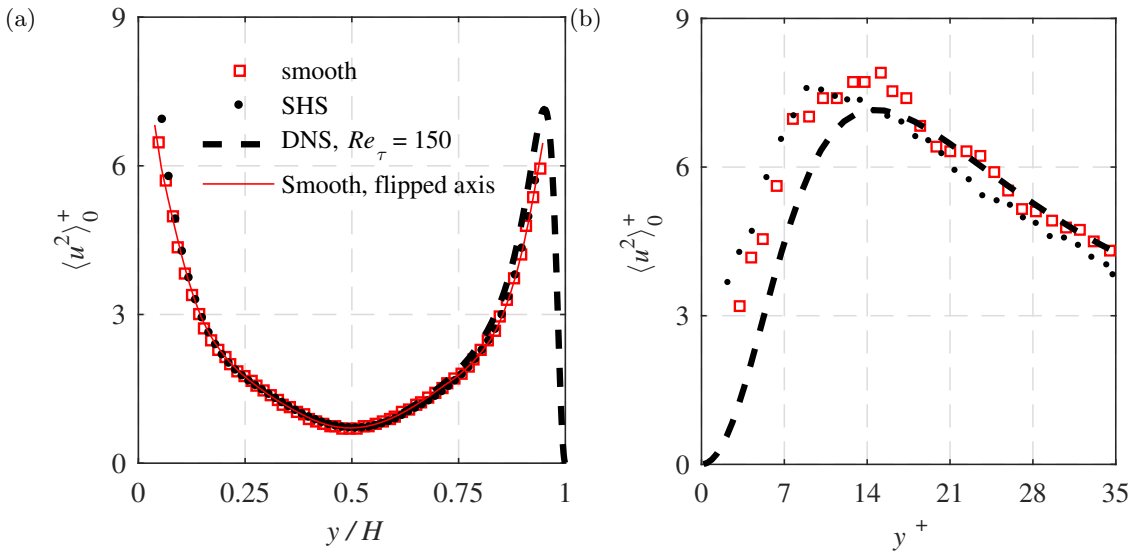

Figure 5.4: (a) Measurement of $\langle u^2 \rangle$ using PIV over smooth and SHS. The wall-normal distance normalized using the outer (H). DNS of Tsukahara et al. (2005) is provided for comparison over the bottom half of the channel. (b) Measurements of $\langle u^2 \rangle$ within the inner layer using micro-PTV.

of the logarithmic layer over SHSs. They observed an approximate overlap of $\langle u^2 \rangle / u_\tau^2$ of SHS and smooth surfaces away from the wall if $\langle u^2 \rangle$ is normalized with the u_τ of the corresponding surface. However, dimensional $\langle u^2 \rangle$ over the SHS is smaller in the outer layer. The holographic measurement of Ling et al. (2016) showed for SHSs with $0.43 \leq k^+ \leq 1.71$, the value of $\langle u^2 \rangle$ is larger than the smooth case at $y^+ < 10$ with the peak closer to the wall. At $10 \leq y+ \leq 100$, $\langle u^2 \rangle$ is smaller than the smooth surface for these SHSs. They also reported smaller magnitude of $\langle u^2 \rangle$ peak at larger DR. In general, simulations and experiments show SHSs increase $\langle u^2 \rangle$ in the inner layer (linear sublayer and buffer layer) while reduce $\langle u^2 \rangle$ in the outer layer.

The wall-normal component of Reynolds stress, $\langle v^2 \rangle$, is shown in Figure 5.5a from PIV measurements over both surfaces across the channel. The $\langle v^2 \rangle$ profiles of the smooth and SHS overlap across most of the bottom-half of the channel although there are discrepancies near the bottom wall at $y/H > 0.85$. However, $\langle v^2 \rangle$ peak values of the two surfaces at $y/H \sim 0.8$ overlap. The smaller peak value relative to the DNS of Tsukahara et al. (2005) is attributed to the smaller Re_τ of the current experiment and also the spatial averaging of

PIV. The symmetry of the $\langle v^2 \rangle$ profile of the smooth is also evident from comparison with the flipped data as shown by the red line. The peak of $\langle v^2 \rangle$ over SHS at $y/H = 0.18$ (or $y^+ = 51$) is reduced by about 5% relative to the peak value over the smooth surface. The location of $\langle v^2 \rangle$ peak is also fixed within the spatial-resolution of the PIV system (17.6^+). The difference of $\langle v^2 \rangle$ profiles decreases with reduction of wall-normal distance as they overlap at $y/h = 0.05$ ($y^+ = 15$).

The normalized $\langle v^2 \rangle$ in the inner layer of $y^+ < 35$ is shown in Figure 5.5b from micro-PTV measurements. The $\langle v^2 \rangle$ over SHS and smooth surface are observed to overlap near the wall at $y^+ < 10$. Beyond $y^+ > 10$, $\langle v^2 \rangle$ over the SHS becomes smaller than the smooth surface. About 30% reduction of $\langle v^2 \rangle$ is observed at $y^+ = 30$. The experiments of Vajdi Hokmabad and Ghaemi (2016) showed 13% reduction in $\langle v^2 \rangle$ peak over SHS while the peak moved away from the wall by 15 wall unit. Woolford et al. (2009a) also observed about 5% reduction of $\langle v^2 \rangle$ extended to core of the channel flow. Min and Kim (2004) observed an overlap of $\langle v^2 \rangle$ over the SHS and smooth surface at $y^+ < 8$ but smaller $\langle v^2 \rangle$ over the SHS further away from the wall at $y^+ > 8$. The DNS of Rastegari and Akhavan (2015) shows slightly smaller $\langle v^2 \rangle$ in the near wall when the applied slip velocity is 15% of U_b (similar to the present work). In general, the DNS of Min and Kim (2004); Rastegari and Akhavan (2015) and the current micro-PTV measurement show negligible change of $\langle v^2 \rangle$ in the viscous sublayer. However, Ling et al. (2016) observed an increase of $\langle v^2 \rangle$ over the SHSs in the inner layer with $y^+ < 10 - 30$ depending on the roughness of the surface. This difference is associated with larger roughness of surfaces tested by Ling et al. (2016) compared to the current experiment and DNS with assumption of a flat surface. Further away from the wall, all experiments (e.g., Woolford et al. (2009a); Vajdi Hokmabad and Ghaemi (2016)) and simulations (e.g., Min and Kim (2004); Rastegari and Akhavan (2015)) with DR show reduction of $\langle v^2 \rangle$ relative to that of the smooth wall.

The joint probability density function (JPDF) of u and v velocity fluctuations from micro-PTV is plotted in Figure 5.6a to investigate the correlation of the fluctuations over the SHS. The data is associated with $y^+ = 20 - 30$ range for statistical convergence of the JPDF.

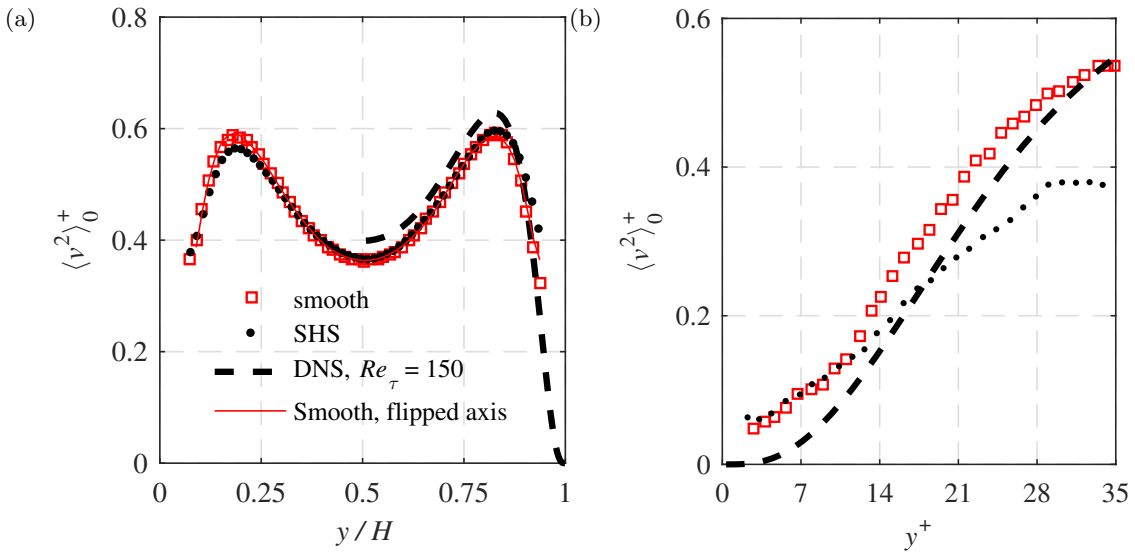

Figure 5.5: (a) Measurement of $\langle v^2 \rangle$ using PIV over smooth and SHS. The wall-normal distance normalized using the outer (H). DNS of Tsukahara et al. (2005) is provided for comparison over the bottom half of the channel. (b) Measurements of $\langle u^2 \rangle$ within the inner layer using micro-PTV.

The separate PDFs of u and v are also shown in Figure 5.6b and 5.6c. The area enclosed by the contours in the sweep quadrant (i.e., $u > 0$ and $v < 0$) for the SHS is similar to the smooth surface. However, the enclosed area by the contours in the ejection quadrant ($u < 0$ and $v > 0$) is smaller over the SHS relative to the smooth surface. The principle axis of the fluctuations has also tilted towards the u axis over the SHS, indicating ejection motions with smaller angle with respect to the wall (smaller v). This modification to turbulent fluctuations is also observed in the PDF plots. A negligible change of u distribution is observed in Figure 5.6b, while the PDF of v over the SHS in Figure 5.6c becomes narrower with a larger peak at $-0.5 < v/u_\tau < 0.5$. The latter shows that there is a larger number of weak v fluctuations and smaller number of strong v fluctuations over the SHS surface. Therefore, the slip boundary condition has resulted in attenuation of ejection motions in $y^+ = 20 - 30$ range.

The JPDF of u and v velocity fluctuations in the wall-normal range of $y^+ = 5 - 15$ over the SHS and smooth surface is shown in Figure 5.7a. The effect of slip velocity at this range is different relative to the $y^+ = 20 - 30$ range. The sweep events in the fourth quadrant

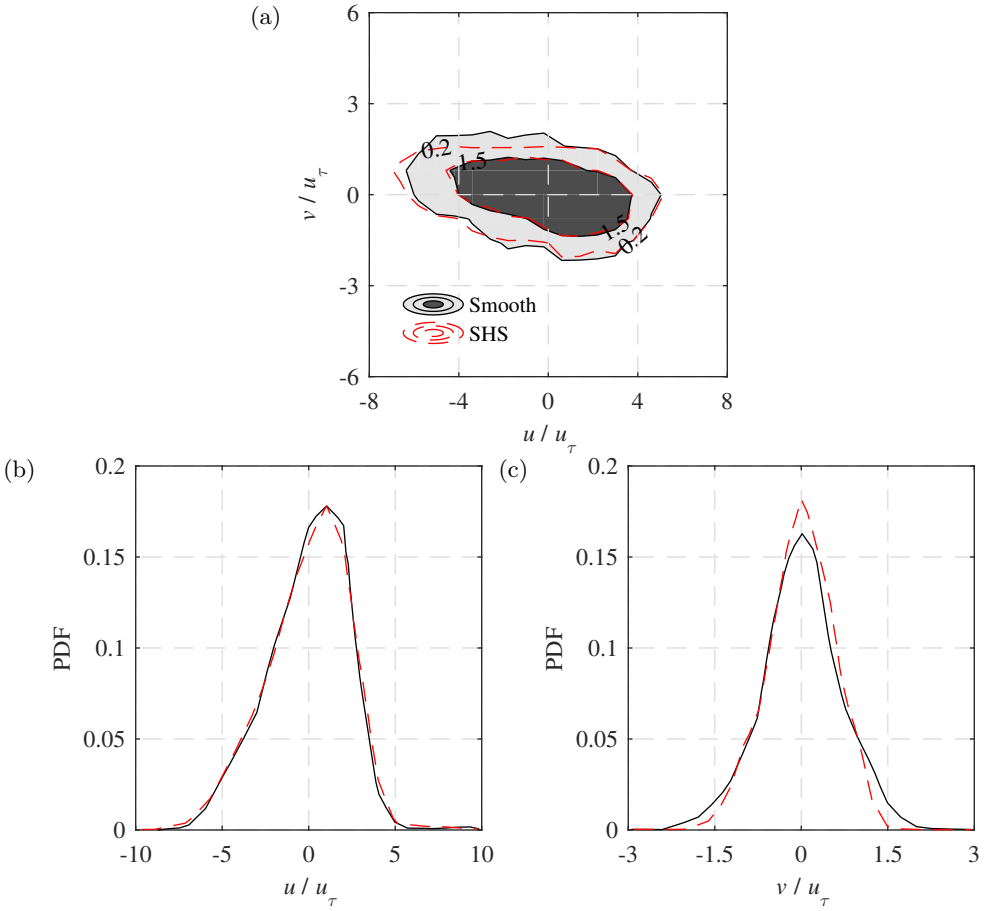

Figure 5.6: (a)The JPDF of u and v fluctuations in the buffer layer $y^+ = 20 - 30$. The filled contours represent the JPDF over the smooth surface and the lines contours in red show the JPDF over the SHS. The dark gray and the light gray colors represent the 1.5%, and 0.2% JPDF values, respectively. The 2D PDF of (b) the u and (c) v fluctuations. The solid lines in PDF represent the smooth surface while the dashed red lines show the PDF of the SHS.

$(u > 0, v < 0)$ are attenuated while the ejection motions $(u < 0, v > 0)$ appear to have a similar JPDF as the smooth surface. This attenuation of sweep events is associated with reduction of the intensity of strong u fluctuations as observed in the PDF of Figure 5.7b at about $u/u_\tau = \pm 6$. The PDF of v fluctuation in Figure 5.7c does not show a significant variation of v fluctuations over the SHS in comparison with the smooth surface.

5.2.4 Analysis of surface stability

Drag reduction over an SHS depends on the topology and lifetime of the air layer (plastron). Several repeats of PIV and micro-PTV experiments showed occasional failure of the surfaces ($\sim 30\%$ of the tests) and lack of DR, which is speculated to be due to partial or total loss of the air-layer over the SHS. The presence of PIV/PTV tracers and small variations of pH and oxygen level in the flume ($\sim$ 2000 liters of tap water) may have contributed to the inconsistencies. The pH and oxygen level of the water were monitored to be between 7.9–8.1 and 8.3–8.4 mg/l in all the experiments. The manufacturing repeatability and surface defects can also affect the DR.

Two data sets are introduced here as "stable" and "unstable" plastron to characterize the longevity of the SHSs. The unstable data are associated with an SHS that gradually lost its DR performance. The longevity of the SHS is monitored by applying the EOC method on the first 100 s (500 double-frame images) and the last 100 s ($t = 1500 - 1600$ s) of the long-range micro-PTV images. The 100 s interval is chosen as a compromise between statistical convergence and temporal resolution. The convergence and repeatability of this method are evaluated on the smooth surface in Figure 5.8a. The mean velocity profiles of the initial ($t = 0 - 100$ s) and the final ($t = 1500 - 1600$ s) subsets overlap at $y^+ < 5$, showing the statistical convergence of the analysis. The mean velocity at $y^+ = 0$ is also negligible in both subsets indicating the no-slip boundary condition over the smooth surface. The results for the initial and final subsets of the stable SHS are shown in Figure 5.8b. The results confirm the stability of the slip velocity $U_s^+ \sim 1.5 - 2$ over time. The detected U_s^+ using the EOC method is smaller than the estimated value using micro-PTV in Figure 5.2c

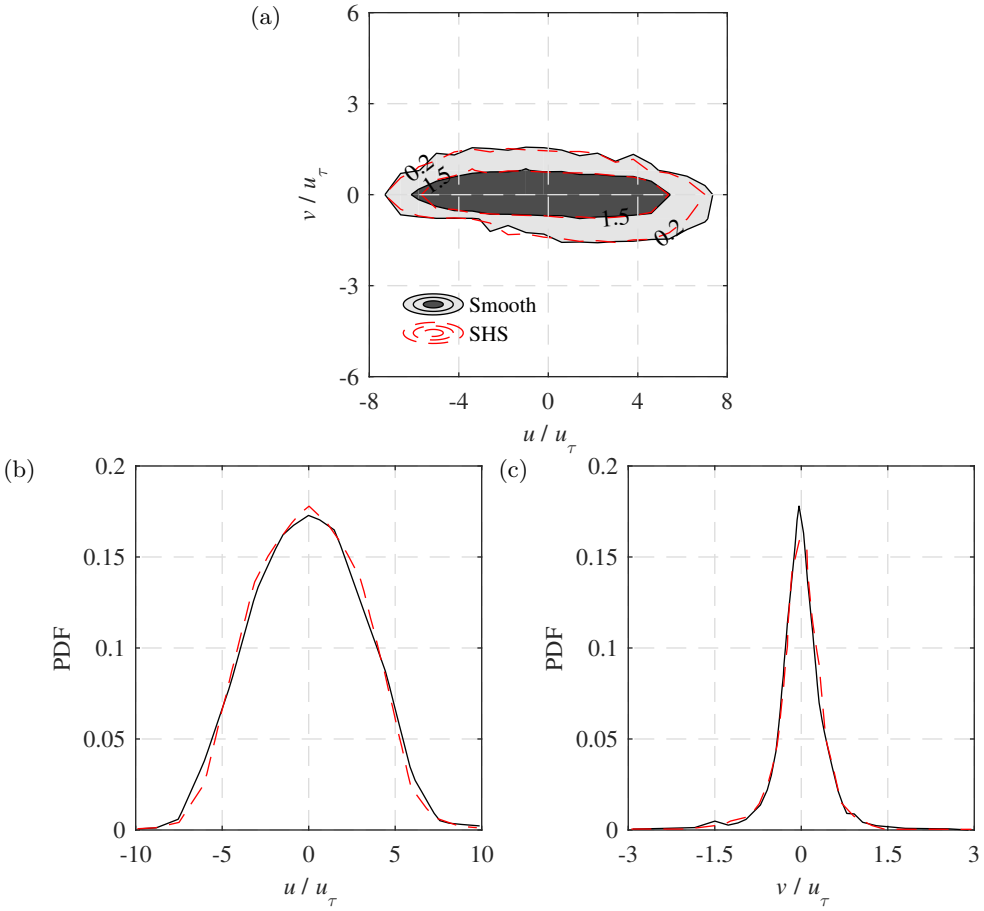

Figure 5.7: (a)The JPDF of u and v fluctuations in the buffer layer $y^+ = 5 - 15$. The filled contours represent the JPDF over the smooth surface and the lines contours in red show the JPDF over the SHS. The dark gray and the light gray colors represent the 1.5%, and 0.2% JPDF values, respectively. The 2D PDF of (b) the u and (c) v fluctuations. The solid lines in PDF represent the smooth surface while the dashed red lines show the PDF of the SHS.

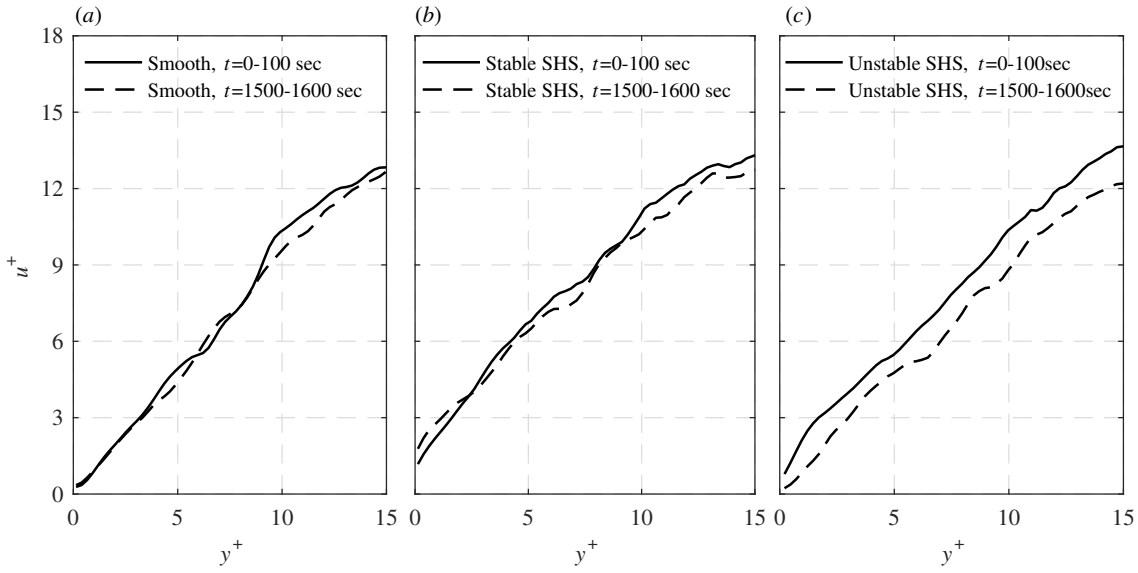

Figure 5.8: Normalized mean streamwise velocity (u^+) over the (a) smooth surface, (b) stable SHS, and (c) unstable SHS obtained from two subsets of the data. The first subset includes the 500 double-frame PTV images from t = 0-100 s, and the second subset covers t = 1500-1600 s.

due to the larger spatial-resolution of the EOC. The slip velocity over the unstable SHS in Figure 5.8c during $t = 0 - 100$ s is slightly smaller than the stable surface. However, in the final subset ($t = 1500 - 1600$ s) of Figure 5.2c, U_s^+ approaches zero and the unstable SHS loses its DR performance.

The temporal variation of SHS performance is characterized by averaging the streamwise velocity in the wall-normal range of $y^+ < 15$ and also over time intervals of 100 s (moving average). The combined average enhances statistical convergence of the data and is indicated by $\langle U_t^+ \rangle$. The result is shown in 5.9 as $u_t^+ = \langle U_t^+ \rangle / u_\tau$ for the smooth surface, stable SHS, and unstable SHS. The average velocity over the smooth surface and stable SHS is relatively constant in time, while u_t^+ of the unstable SHS decreases with time over $t = 0$ until 800 s. The velocity over both SHSs started at larger values ($u_t^+ = 6.5, \sim 0.08$ m/s) than the smooth surface ($u_t^+ = 5.3, \sim 0.06$ m/s). However, after 300 s, the unstable SHS loses the plastron as the mean velocity reduces from u_t^+ of the stable SHS to that of the smooth surface. This investigation highlights the importance of plastron evaluation in large-scale experiments. It also shows the need for simultaneous PIV and micro-PTV of the

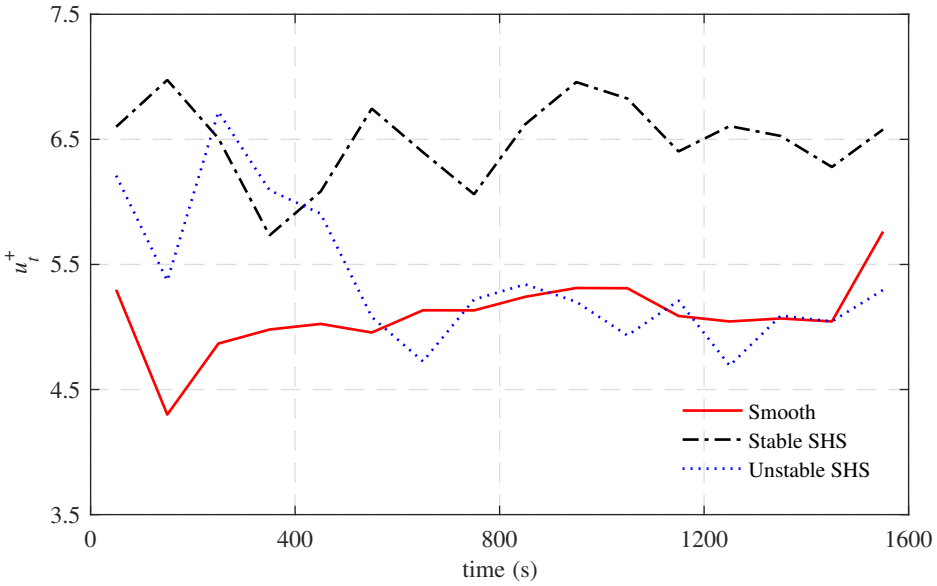

Figure 5.9: Velocity obtained from micro-PTV is averaged within the wall-normal range of $y^+ = 1$–15 and with a temporal kernel of 100 s (500 images pairs) for the smooth surface, stable SHS, and unstable SHS.

current investigation to ensure inner and outer layer characterization is carried out over the same plastron.

5.3 Discussion

The investigation showed that the applied SHS with random texture reduces drag by $\sim 20\%$ due to the 200 μm slip length. The comparison of Reynolds stresses over the SHS and smooth surface is carried out at a constant flow rate while the Reynolds stresses are normalized using a common inner scaling. The results showed that $\langle uv \rangle$ and $\langle u^2 \rangle$ increase over the SHS at the near-wall region of $y^+ < 10$. However, $\langle v^2 \rangle$ over the SHS stays comparable to the smooth surface within $y^+ < 10$. Ling et al. (2016) observed increase of all three $\langle uv \rangle$ and $\langle u^2 \rangle$, and also $\langle v^2 \rangle$ over the SHS within $y^+ < 10$ while the flow rate was kept constant. The percentages of increase in Reynolds stresses based on the experiment of Ling et al. (2016) is also larger than those of the current study as it is detailed in Table 1. The larger increase is associated with larger roughness (larger k^+) as presented Figure 5.10. In this figure, the variation of Reynolds shear stress is defined as $\Delta\langle uv \rangle = ([\langle uv \rangle_{SHS} - \langle uv \rangle_{smooth}]/\langle uv \rangle_{smooth})$,

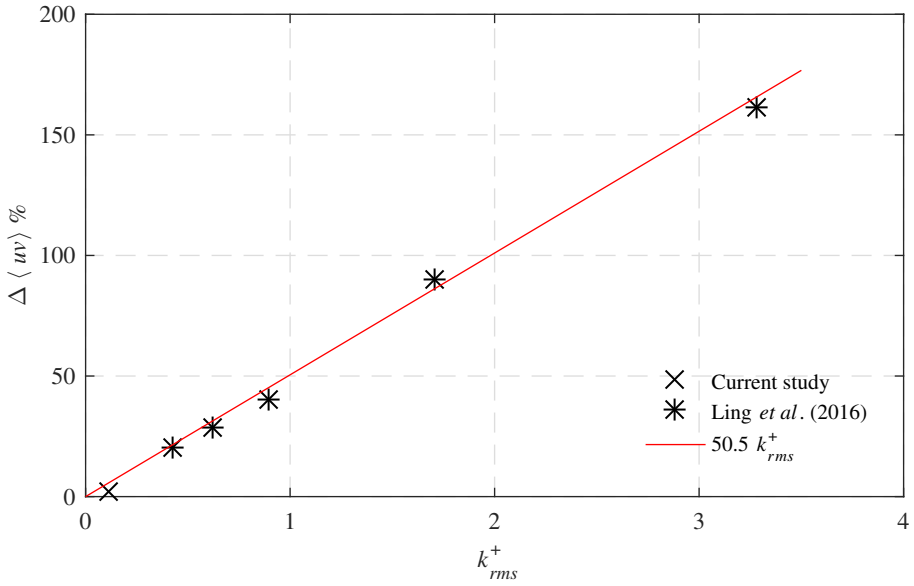

Figure 5.10: Variation of Reynolds shear stress over SHS in comparison with the smooth surface at $y^+ = 5$ versus the surface roughness (k^+).

and estimated from Ling et al. (2016) and the current investigation at $y^+ = 10$. The results, presented versus the surfaces roughness (k^+), show a linear increase of $\langle uv \rangle$ with increase of roughness. However, the larger Reynolds shear stress in the near wall region of the SHSs does not necessarily indicate drag increase as the total drag also depends on the slip velocity. The dependence of total drag on Reynolds shear stress and slip velocity is observed in Equation 5.3. It is important to note that the current investigation has been carried out a low Re_τ and the results cannot be extended to surfaces with lower roughness at the higher Re_τ of Ling et al. (2016). However, the current investigation is suitable for evaluation of DNS at low Re_τ such as Min and Kim (2004); Rastegari and Akhavan (2015).

The experiments of the current study and also Ling et al. (2016) are both carried out at a constant flow rate. Therefore, the friction velocity and Re_τ reduce in case of drag reduction. If Reynolds stresses are scaled based on the corresponding friction velocity (i.e., $u_{\tau s} = 0.0100$ m/s of the SHS instead of $u_\tau = 0.0113$ of the smooth surface where $u_{\tau s}$ is the friction velocity of the SHS), the non-dimensional stresses of the current work show a larger increase of $\langle uv \rangle / u_\tau^2$, $\langle u^2 \rangle / u_\tau^2$, and $\langle v^2 \rangle / u_\tau^2$ over the SHS with respect to the smooth at $y^+ < 10$ as illustrated in Figure 5.11. Farther away from the wall at $y^+ > 10$, the scaling

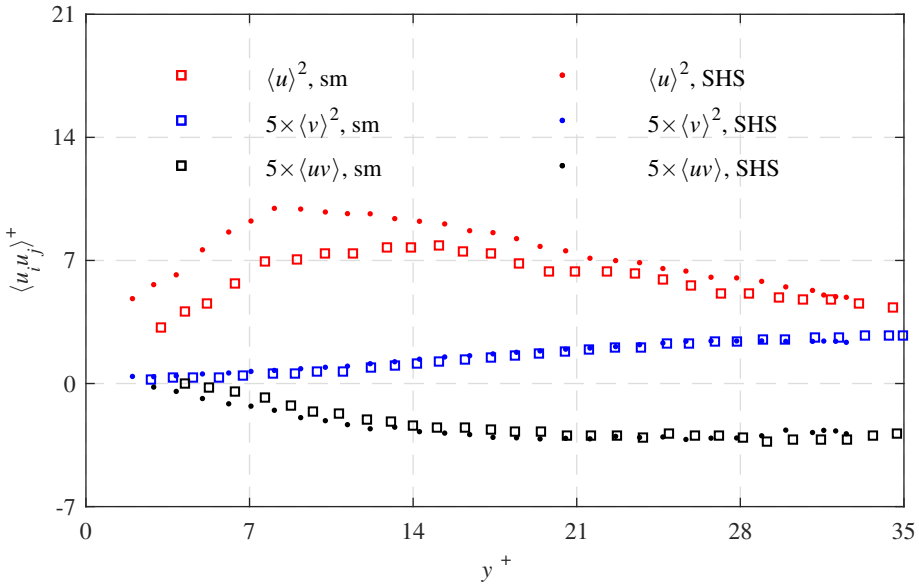

Figure 5.11: Inner layer measurement of Reynolds stresses using micro-PTV over smooth and SHS normalized by the corresponding friction velocity. $\langle uv \rangle$ and $\langle v^2 \rangle$ multiplied by 5 for clarity.

of $\langle uv \rangle$ and $\langle v^2 \rangle$ based on the corresponding $u\tau$ results in overlap of the smooth and SHS profiles.

5.4 Conclusion

The magnitude of slip velocity and the effect of the superhydrophobic surface (SHS) on Reynolds stress in the inner and outer layers have been experimentally investigated using simultaneous long-range microscopic particle tracking velocimetry (micro-PTV) and macroscopic particle image velocimetry. The micro-PTV results show a slip velocity of 0.023 m/s over the SHS which corresponds to 200 μm slip-length. A drag reduction of 19% based on the slope of the linear viscous sublayer realized. The reduced friction Reynolds number over the SHS based on the corresponding friction velocity is ~ 125. The quadrant analysis of turbulent fluctuations shows attenuation of stronger sweep motions at $y < 15\lambda$, while ejections are attenuated in the buffer layer at $y = 20\lambda$ until 30λ.

Chapter 6

Streamwise and spanwise slip over a superhydrophobic surface

6.1 Introduction

The effect of the slip velocity on Reynolds stresses can be evaluated by comparison with a smooth surface with a no-slip boundary condition under the same bulk flow velocity. Reduction in the streamwise, wall-normal, and shear Reynolds stresses is observed in the outer layer as seen in the experiments of Woolford et al. (2009a); Vajdi Hokmabad and Ghaemi (2016); Ling et al. (2016); Abu Rowin et al. (2017). However, closer to the wall at $y < 10\lambda$, the streamwise Reynolds stress, $\langle u^2 \rangle$, and shear Reynolds stress, $\langle uv \rangle$, are larger than those over the smooth surface (Ling et al., 2016). The increase in $\langle u^2 \rangle$ is associated with the increase of fluctuations by relaxing the no-slip boundary condition. On the other hand, the increase in $\langle uv \rangle$ is mostly associated with the roughness of the SHS as discussed by Abu Rowin et al. (2017). The wall-normal Reynolds stress, $\langle v^2 \rangle$, remains comparable to that over the smooth surface near the wall due to the non-permeable boundary condition for SHSs with low roughness (Abu Rowin et al., 2017). Ling et al. (2016) reported an increase of $\langle v^2 \rangle$ near the SHS, which is presumably due to the high roughness of their tested surfaces. The numerical studies have also confirmed these trends (Min and Kim, 2004; Busse and Sandham, 2012; Rastegari and Akhavan, 2015). A near-wall increase of spanwise Reynolds stress, $\langle w^2 \rangle$, was also observed in the DNS of Min and Kim (2004) when a spanwise slip ($l_z \neq 0$) was imposed. It is interesting to note that $\langle w^2 \rangle$ increased over an SHS with

streamwise microgrooves in the DNS of Rastegari and Akhavan (2015) as well. This suggests that a surface with streamwise microgrooves can also result in an effective spanwise slip. The characterization of the local slip is of particular importance for simulation of SHS with random texture. However, there has been no experimental investigation of the magnitude of spanwise slip over an SHS in a turbulent flow.

Although there is a large number of DNS over SHSs with an organized pattern in turbulent flow, a limited number of numerical studies modeled the flow over randomly textured SHSs due to limited information about the air layer pattern over this texture. The DNS of Seo et al. (2018a) compared SHSs with organized and randomly patterned no-slip posts with the same height. They reported that the interruption of the shear-free regions over the randomly distributed posts results in 30% smaller slip length compared with the SHS with the organized pattern. Seo et al. (2018a) also indicated that the randomly patterned SHS with small roughness elements ($\sim 4\lambda$) can be modeled with an isotropic homogeneous effective slip length ($l_x = l_z$) at the surface. However, for surfaces with larger roughness, a model with a distribution of a non-isotropic slip is required. Thus, the degree of the non-isotropy slip ($l_x \neq l_z$) over SHS with larger roughness is not clear. The numerical study of Alamé and Mahesh (2019) modeled the flow over a more realistic SHS with a random pattern obtained from surface profile measurement over a sandblasted aluminum substrate. They observed that the shear-free interface attenuates the turbulence intensities while the surface roughness increases turbulence. Further development of numerical simulations of SHSs benefits from an experimental characterization of slip non-isotropy ($l_x \neq l_z$), and its inhomogeneity over an SHS.

The present investigation measures the slip velocity in both the streamwise and spanwise directions over a spray-coated SHS with a random texture. This investigation also characterizes all components of the near-wall Reynolds stresses and the inhomogeneity of the shear-free interface over an SHS.

6.2 Results

The experiments were operated at a constant flow rate with a bulk velocity of $U_b = 0.93m/s$, defined as the average velocity over the cross-section. The Reynolds number is $Re = 7000$, based on the full channel height (H). The friction velocity over the no-slip smooth surface is $u_{\tau 0} = 0.060$ m/s and the wall unit is $\lambda_0 = 13.3\mu$m, based on the wall-normal gradient of mean velocity in the linear viscous sublayer as described in Section 6.2.1. The estimation also agrees with the inner scaling obtained from Clauser's method using the logarithmic law of the turbulent boundary layer (Clauser, 1956). The friction Reynolds number based on the half channel height is $Re_\tau = 225$. Summary of the channel flow dimensions and the flow characteristics is listed Table 6.1. The streamwise and spanwise velocities and the Reynolds stresses over the SHS are investigated in this section. The test surfaces are placed at the top wall of the channel where y = 0. The error of estimating the wall location, that was discussed in Chapter 4 in Section 4.3.3, is equivalent to $0.26\lambda_0$. The DNS results of smooth channel flow from Gilbert and Kleiser (1991) at $Re_\tau = 211$ and Rastegari and Akhavan (2015) at $Re_\tau = 222$ are also used to evaluate the uncertainty in the measurement of velocity and Reynolds stresses. The superscript + denotes parameters normalized using inner scaling, i.e., velocities are normalized by u_τ and the coordinate system is normalized by λ. If the subscript 0 is added, it indicates that the parameters are normalized using the inner scaling of flow over the smooth surface. When there is no subscript, the normalization is carried out by the inner scaling of the corresponding surface.

6.2.1 Streamwise velocity

Scatter plots of the streamwise velocity of the particles over the smooth and SHS from 3D-PTV are shown in Figures 6.1a and 6.1b, respectively. The velocity over both surfaces is normalized using the inner scaling of the smooth surface ($u_0^+ = \langle U \rangle / u_{\tau 0}$), and the plots cover the inner layer up to $y^+ = 100$. The mean velocity profile is also shown using the solid lines by averaging the data over 10 μm (0.72λ) bins with 75% overlap. The mean velocity profile at $y^+ < 2.5$ is not shown due to its deviation from the expected linear viscous

Parameter	Dimensions	Value
Channel dimensions ($H \times W \times L$)	mm	$6 \times 40 \times 1200$
U_b	m/s	0.93
U_{max}	m/s	1.2
Re	...	7000
$u_{\tau 0}$	m/s	0.060
λ_0	μm	13.3
Re_τ	...	225

Table 6.1: Summary of the parameters of the turbulent channel flow with smooth wall.

sublayer profile $u^+ = y^+$ for the smooth surface. Therefore, $y^+ = 2.5$ is considered as the lower limit of the measurements. This limitation is imposed by the size of the fluorescent tracer particles ($d = 10\mu\text{m} = 0.72\lambda$) and lack of data at $y^+ < 2.5$.

As shown in Figure 6.1a, there are a large number of particles with small $u_0^+ (< 2.5)$ in the immediate vicinity of the smooth wall, indicating the no-slip boundary condition. However, particles with larger u_0^+ varying from 2 to 8 (0.12 to 0.48 m/s) are observed at the lowest wall-normal limit of the measurement in Figure 6.1b. The larger streamwise velocity at $y^+ = 2.5$ indicates the presence of a streamwise slip velocity at the SHS. The larger scatter of the instantaneous streamwise velocity in the vicinity of the SHS also agrees with the 2D-PTV of Abu Rowin et al. (2017) over an SHS at $Re_\tau = 140$.

The mean streamwise velocity at $y^+ < 15$ over the smooth and SHS are presented in Figure 6.2a. The inner variables over the smooth surface are estimated using the wall-normal gradient of $\langle U \rangle$ within $22.5 < y^+ < 3.5$. Figure 6.2a shows that the mean streamwise velocity over the smooth surface follows the law-of-the-wall ($u^+ = y^+$) in the linear viscous sublayer and the DNS of Rastegari and Akhavan (2015) over the smooth channel at $Re_\tau = 222$. The extrapolation of the fitted line on the velocity profile of the smooth surface approaches zero at the wall. The values of u_0^+ over the SHS are higher than those of u_0^+ over the smooth surface near the wall region due to the streamwise slip velocity. Farther away from the wall, the mean velocity over the SHS becomes smaller than the smooth surface; however, the outer layer is not shown for brevity. The numerical simulation of Min and Kim (2004), the

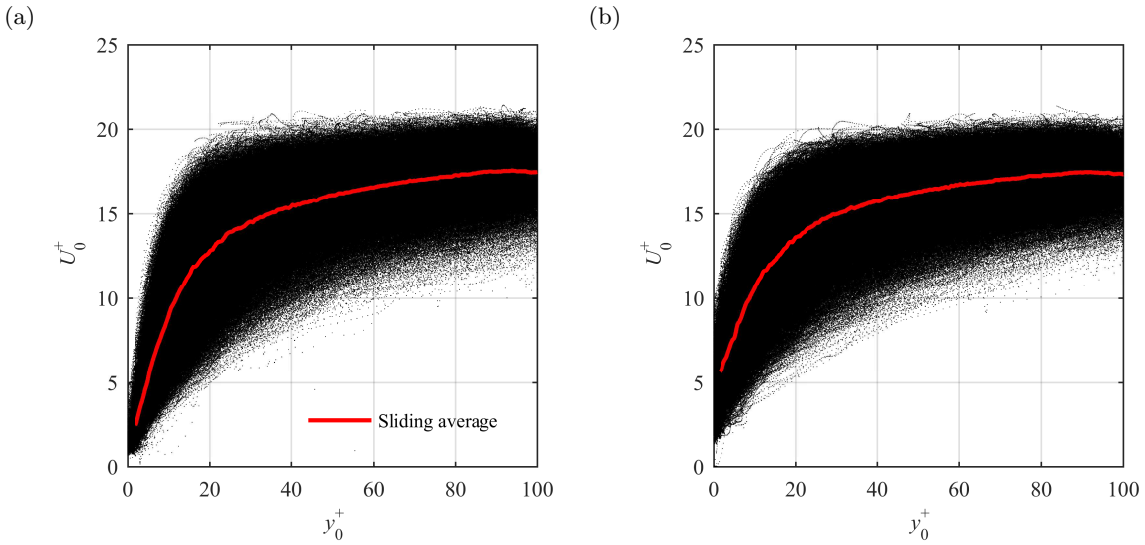

Figure 6.1: Streamwise velocity of the individual tracers over (a) smooth and (b) SHS. The data is normalized using inner variables of the smooth surface.

theoretical work of Fukagata et al. (2006), and measurements of Abu Rowin et al. (2017) have also observed a larger near-wall velocity and a smaller velocity farther away from an SHS. The slip velocity over the SHS is estimated by extrapolation of a linear fit over the near-wall velocity within $2.5 < y^+ < 3.5$ to $y^+ = 0$ as shown in Figure 6.2a. The estimated slip velocity is $U_{s0}^+ = U_s/u_{\tau 0} \approx 4.54$ ($U_s = 0.27$ m/s), which results in $U_s/U_b \approx 30\%$. The repeatability of the measurement is confirmed by carrying out the STB measurements over two additional SHSs manufactured through a similar spray coating procedure. The measured Us over these two SHSs is 0.30, and 0.25 m/s, showing $\pm 8\%$ variation. The slope of this line is also used to estimate the inner scaling over the SHS. The estimated friction velocity over the SHS is $u_\tau = 0.048$ m/s, which is reduced by 17% with respect to the smooth surface. This corresponds to $Re_\tau = 180$ over the SHS. In Figure 6.2b, the velocity over the smooth and SHS is normalized by their corresponding inner scaling. The fitted line over the mean velocity of the SHS within $2.5 < y^+ < 3.5$ follows $u^+ = y^+ + U_s^+$. The slip velocity normalized as $U_s^+ = U_s/u_\tau$ is 5.76, and the effective slip length is $l_s \approx 96.5$ μm (5.91λ).

The probability density function (PDF) of u_0^+ over the smooth and SHS in the immediate

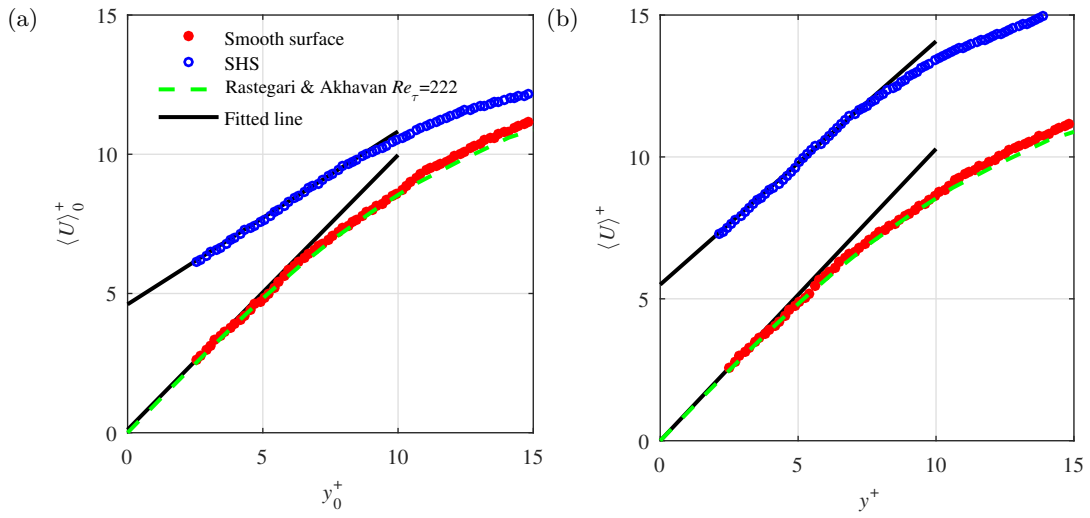

Figure 6.2: Mean velocity profiles normalized by the inner variables of the (a) smooth surface and (b) their corresponding inner variables. The mean values are obtained over bins of 10 μm (0.72λ) with 75% overlap in y direction. The fitted lines over the data of $2.5 < y^+ < 3.5$ are shown with black solid line. The DNS of Rastegari and Akhavan (2015) at $Re_\tau = 222$ is also shown for comparison.

vicinity of the wall at $2.5 < y^+ < 3.5$ is shown in Figure 6.3a. This PDF shows that the SHS has shifted the streamwise velocity distribution toward larger velocities with a broader distribution due to the streamwise slip velocity. Farther away from the wall at $45 < y^+ < 46$, the streamwise slip has a smaller influence on the PDF of U_0^+ as shown in Figure 6.3b. Our investigation of different wall-normal locations within the log-layer shows a similar trend: a slightly narrower PDF for the SHS. The larger mean streamwise velocity and the wider PDF for $2.5 < y^+ < 3.5$ is consistent with the larger near-wall $\langle u^2 \rangle$ observed in the numerical simulation of Min and Kim (2004); Rastegari and Akhavan (2015).

For the analysis of streamwise velocity over a wider wall-normal distance, semi-logarithmic presentations of u^+ over the smooth and SHS are plotted in Figure 6.4a, together with the DNS of Rastegari and Akhavan (2015). The data is normalized using the inner scaling of the corresponding surface obtained from the linear velocity gradient in Figures 6.4a. The law-of-the-wall for the linear viscous sublayer as $u^+ = y^+$ and the log-law expressed as $u^+ = \frac{1}{\kappa} ln(y^+) + B$ are also shown with the von Kármán constant of $\kappa = 0.41$ and $B = 5.2$. The profile of the smooth surface agrees with the law-of-the-wall and the log-law, indicating

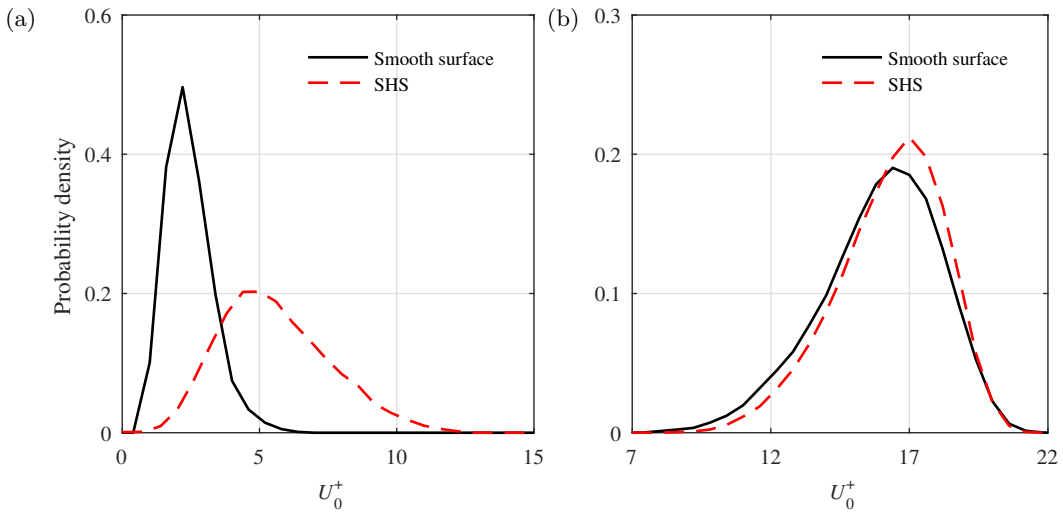

Figure 6.3: Probability density functions of streamwise velocity over the smooth and SHS normalized by the inner variables of the smooth wall for data within (a) $2.5 < y^+ < 3.5$, and (b) $45 < y^+ < 46$.

a fully developed channel flow (Kim et al., 1987). The 3D-PTV measurements are also consistent with the DNS profile in the buffer layer range of $5 < y^+ < 30$. The u^+ of the SHS does not follow the standard log-law and is shifted upward due to the slip velocity. The upward shift of u^+ in the semi-logarithmic representation over an SHS has been observed in previous numerical simulations (Min and Kim, 2004; Martell et al., 2010) and experiments (Woolford et al., 2009a; Ling et al., 2016; Abu Rowin et al., 2017).

In Figures 6.4b, the slip velocity is subtracted from the mean velocity profile (i.e., $u^+ - U_s^+$). As a result, the velocity profile over the SHS overlaps with the velocity profile over the smooth surface in the linear viscous sublayer for $y^+ < 3.5$. In the buffer and log layers, the SHS velocity profile appears to have a slight downward shift. A similar downward shift was reported in the DNS of Min and Kim (2004) when they imposed a slip velocity at the wall in both directions (l_x and l_z). Thus, the downward shift of the log-law in Figures 6.4b indicates the presence of both streamwise and spanwise slip over the current SHS.

6.2.2 Spanwise velocity

Scatter plots of the spanwise particle velocity over the smooth and SHS are presented in Figures 6.5a and 6.5b, respectively. The velocity over both surfaces is normalized using

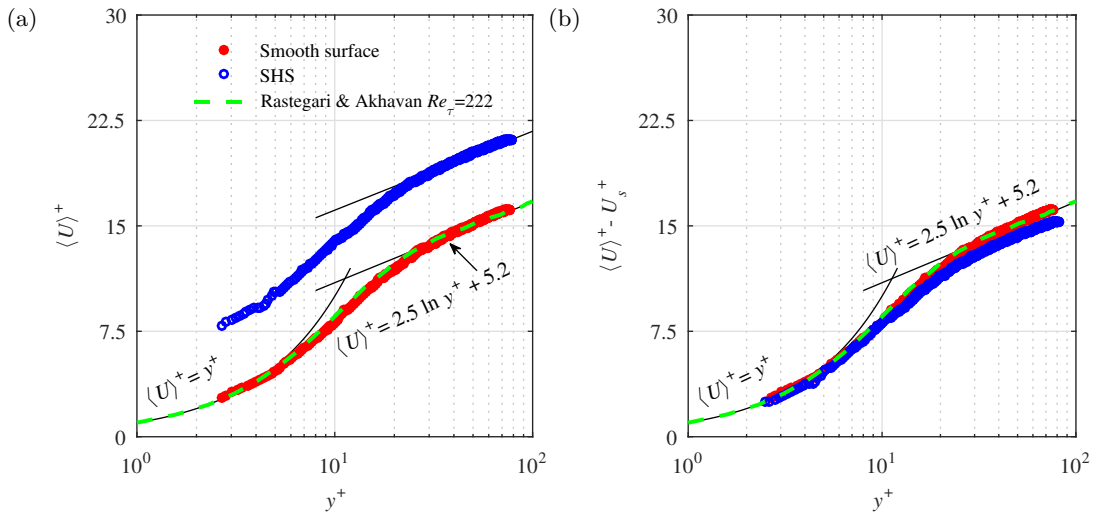

Figure 6.4: (a) Semi-logarithmic plots of mean streamwise velocity normalized with the inner scaling of the corresponding surface $\langle U \rangle$. (b) Semi-logarithmic plots of $\langle U \rangle - U_s^+$. The DNS of Rastegari and Akhavan (2015) in a smooth channel at $Re_\tau = 222$ is also shown for comparison.

the inner scaling of the smooth surface. The mean of absolute spanwise velocity (i.e., $\langle W \rangle = \langle |W| \rangle / u_{\tau 0}$) is also presented with a solid line from an averaging process over widows of 30 μm (2.2λ) with 75% overlap in the y-direction. The lower limit of the mean spanwise velocity is also set to $y^+ = 2.5$, similar to the mean streamwise velocity. Due to the no-slip condition, the spanwise velocity in the vicinity of the smooth surface is negligible in Figures 6.5a. In contrast, a large number of tracers with a finite spanwise velocity within $-0.8 < W_0^+ < 0.8$ appear in the immediate vicinity of the SHS in Figures 6.5b. This large scatter of spanwise velocity confirms the presence of a spanwise slip velocity (W_s). A narrower band of scattering in W_0^+ is observed away from the wall ($y^+ > 20$) in Figures 6.5b when compared with the smooth surface in Figures 6.5a. This will be further scrutinized by investigating profiles of $\langle w^2 \rangle$ in the next section.

The profiles of $\langle W \rangle_0^+ = \langle |W| \rangle / u_{\tau 0}$ over the smooth and SHS are shown in Figures 6.6a. The magnitude of $\langle W \rangle^+$ is much smaller than $\langle U \rangle_0^+$; $\langle W \rangle_0^+$ is about $0.4 u_{\tau 0}$ at $y^+ = 5$ while $\langle U \rangle_0^+$ is $5 u_{\tau 0}$ at $y^+ = 5$. The profile of $\langle W \rangle_0^+$ also does not follow a linear trend in the viscous sublayer. The values of $\langle W \rangle_0^+$ over the smooth surface tend toward a negligible

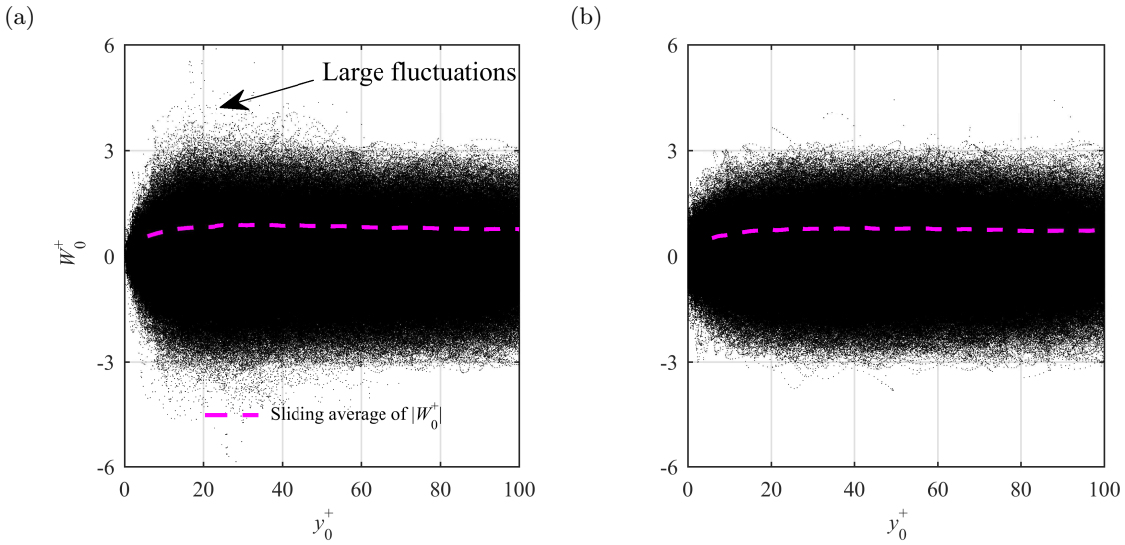

Figure 6.5: Spanwise velocity of the tracers over the (a) smooth and (b) SHS normalized by the inner scaling of the smooth surface. The dashed line shows the mean of the absolute value of spanwise velocity, $\langle|W|\rangle/u_{\tau 0}$, obtained by averaging in 30 μm (2.2λ) bins with 75% overlap.

velocity at the wall, confirming the no-slip boundary condition. The profile of $\langle W\rangle_0^+$ over the SHS is shifted upward and approaches a finite value at the wall, indicating a slip velocity in the spanwise direction. Further away from the SHS at $y^+ > 10$, $\langle W\rangle_0^+$ becomes smaller than that of the smooth surface. This trend is consistent with the streamwise velocity profile but the crossing point is closer to the wall due to the smaller spanwise slip velocity. The profiles of mean absolute spanwise velocity normalized with their corresponding inner scaling, $\langle W\rangle^+ = \langle|W|\rangle/u_\tau$, are shown in Figures 6.6b It is observed in this figure that the variation of $\langle W\rangle^+$ can be described by a second-order polynomial. The extrapolation of the second-order polynomial within $2.5 < y^+ < 7$ for the smooth surface to $y^+ = 0$ also results in zero $\langle W\rangle^+$, which agrees with the no-slip boundary condition. Thus, the spanwise slip velocity and length over the SHS are estimated by applying a second-order polynomial to the data within $2.5 < y^+ < 7$. As displayed in Figure 6.6b, the extrapolation of this model results in a spanwise slip velocity of $0.38u_\tau$ (0.018 m/s) over the SHS which corresponds to an effective spanwise slip length of 5.86λ ($l_z \approx 95.8\mu$m).

The magnitude of the effective slip length in the streamwise direction ($l_x = 96.3\mu$m

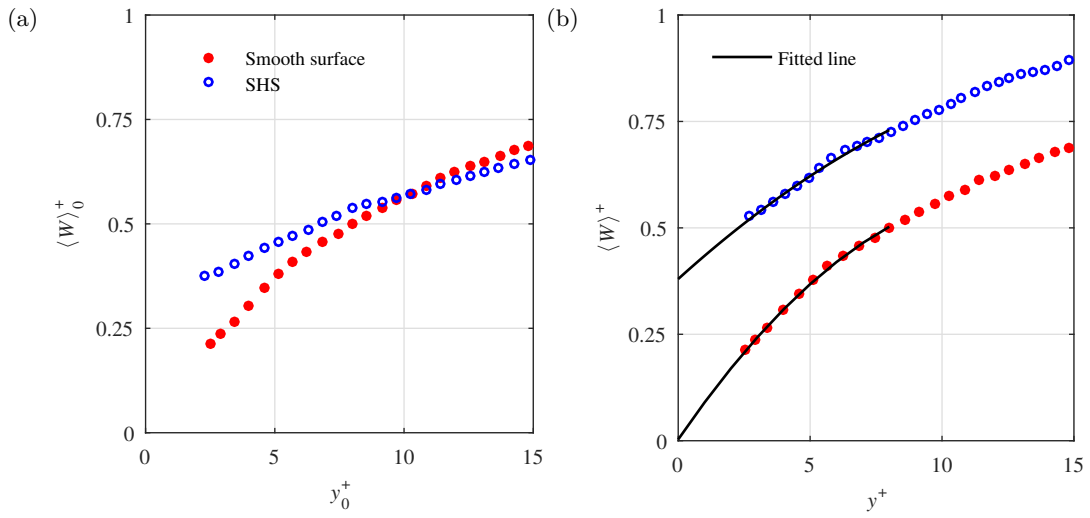

Figure 6.6: Mean of the absolute spanwise velocity over the smooth and SHS obtained from averaging over 30 μm (2.2λ) bins with 75% overlap. The values are normalized by (a) the inner variables of the smooth surface and (b) the corresponding inner variables. Second-order polynomials with $\langle W \rangle^+ = 0.0035y^{+2} + 0.0905y^+ + 0.0031$ and $\langle W \rangle^+ = -0.0015y^{+2} + 0.0560y^+ + 0.3800$ are applied to the smooth and SHS profiles, respectively.

$\approx 5.9\lambda$) is comparable to the magnitude of the effective slip length in the spanwise direction ($l_z = 95.8\mu\text{m} \approx 5.9\lambda$). Therefor the slip boundary condition over the current randomly textured SHS with $k^+ = 0.35$ and $g^+ = 6$ is isotropic. The results confirm the DNS of Seo et al. (2018a), in which a randomly patterned SHS with texture width of $g^+ = 4.3$ was modeled assuming a homogenized isotropic effective slip length ($l_x = l_z$). They observed that an SHS with a larger texture width $g^+ = 28.5$ cannot be modeled by an isotropic effective slip length model.

The PDF of spanwise velocity over the smooth and the SHS for data within $2.5 \leq y^+ \leq 3.5$ and $45 \leq y^+ \leq 46$ are shown in Figure 6.7a and 6.7b, respectively. The SHS increases the probability of large spanwise velocity and reduces the probability of the small spanwise velocity within $2.5 \leq y^+ \leq 3.5$. The effect reduces further away from the wall and the two PDFs overlap in Figure 6.7b. The DNS of Min and Kim (2004) also showed that an imposed l_z at the wall (without l_x) increases $\langle w^2 \rangle$ over an extended wall normal distance; however, imposing both l_x and l_z results in a larger $\langle w^2 \rangle$ only at a short wall-normal distance. The latter is due to an increase of turbulence by the spanwise slip.

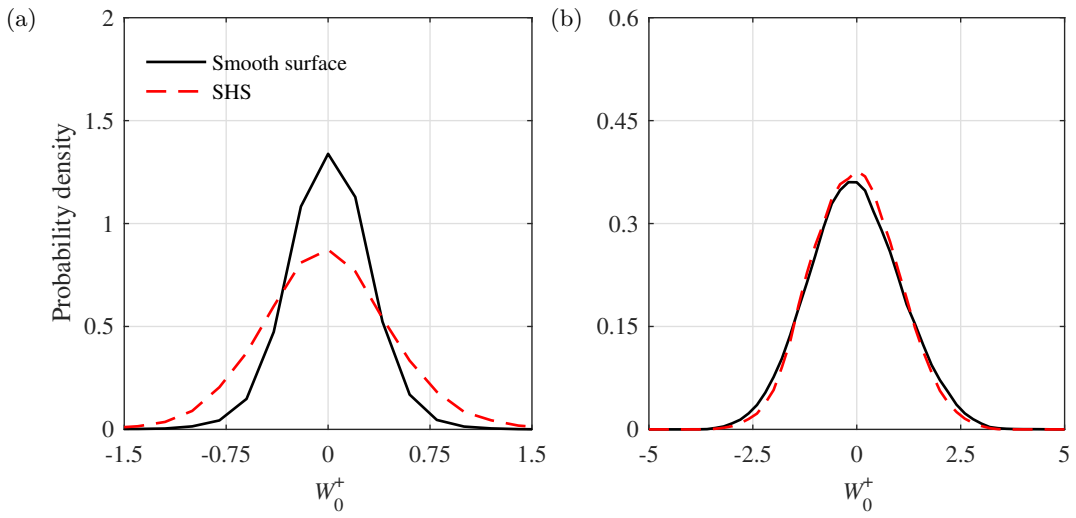

Figure 6.7: The probability density functions of spanwise velocity for velocity data within (*a*) $2.5 < y^+ < 3.5$, and (*b*) $45 < y^+ < 46$.

6.2.3 Turbulence statistics

The profiles of the non-zero components of the Reynolds stress tensors over the smooth and SHS from 3D-PTV at $y^+ < 60$ are shown in Figure 6.8. Reynolds stresses in Figure 6.8 are only shown at $y^+ < 60$ due to the lack of statistical convergence and larger error in Reynolds stresses close to upper boundary of the 3D-PTV domain. The results from the DNS of Gilbert and Kleiser (1991) at a Re_τ of 211 and Rastegari and Akhavan (2015) at a Re_τ of 222 over the smooth surface are also shown for comparison. The two DNS data are also used to show the effect of a small change in Re_τ since the smooth surface is at a Re_τ of 217 and the SHS is at a lower Re_τ of 180. The DNS of Rastegari and Akhavan (2015) over an SHS modeled as an organized array of streamwise microgrooves with $U_s/U_b = 0.32$ and a DR of 33% is included in the right-side plots of Figure 6.8 for comparison. The SHS performance of the DNS is similar to the current investigation where $U_s/U_b = 0.3$ and the DR is about 30% (discussed in Section 6.2.5). In addition, Reynolds stresses over an SHS with randomly distributed posts (with the same height) from DNS of Seo et al. (2018a) is also included in the right-side plots of Figure 6.8. The simulated SHS of Seo et al. (2018a) has $U_{s0}^+ = 4.5$ similar to $U_{s0}^+ = 4.54$ of the current SHS. The averaging is carried out using

windows of 50 μm (3.8λ) with 75% overlap in the $y-$direction. The Reynolds stresses are normalized by the inner variables of the smooth surface (i.e., $\langle u_i u_j \rangle_0^+ = \langle u_i u_j \rangle / u_{\tau 0}^2$) in Figure 6.8 (a, c, and g) at the left side and normalized using the inner variable of the corresponding surface (i.e., $\langle u_i u_j \rangle^+ = \langle u_i u_j \rangle / u_\tau^2$) in Figure 6.8 (b, d, f, and h) on the right side. When the Reynolds stresses of the SHS are normalized with the inner scaling of the smooth surface it is possible to study their variation at a constant bulk flow rate without considering the change in friction velocity. Both normalizations have been applied in the literature.

The streamwise Reynolds stress of the smooth surface $\langle u^2 \rangle_0^+$, in Figure 6.8a follows the DNS profiles. There is a slight difference which is associated with the difference in Re_τ and measurement noise. In the near wall region of $y^+ < 12$, $\langle u^2 \rangle_0^+$ over the SHS is larger than the smooth surface due to the streamwise slip. Away from the wall, $\langle u^2 \rangle_0^+$ attenuates and becomes smaller than the smooth surface. The closer distance of the $\langle u^2 \rangle_0^+$ peak to the wall suggests a thinner inner layer over the SHS. The $\langle u^2 \rangle_0^+$ peak is 16% smaller than the smooth surface and is shifted closer to the wall to $y^+ = 14$. The DNSs of Min and Kim (2004) and Busse and Sandham (2012) also reported an increase of $\langle u^2 \rangle_0^+$ in the immediate vicinity of the wall and a reduction of $\langle u^2 \rangle_0^+$ farther away from the wall when a finite l_x was imposed. Min and Kim (2004) also showed that the modulation of $\langle u^2 \rangle_0^+$ became negligible when l_x was reduced from 3.57λ to 0.36λ.

When $\langle u^2 \rangle$ of the SHS is normalized with its friction velocity in Figure 6.8b, $\langle u^2 \rangle^+$ of the SHS is larger than that of the smooth surface in the near-wall region and it slowly approaches $\langle u^2 \rangle^+$ of the smooth surface at about $y^+ = 45$. A smaller $\langle u^2 \rangle^+$ is observed for the SHSs of Rastegari and Akhavan (2015) and Seo et al. (2018a) relative to the measurements over the SHS in Figure 6.8b. The smaller $\langle u^2 \rangle^+$ of the DNSs over the SHS compared with $\langle u^2 \rangle^+$ of the current investigation is associated with the flatness or the structure of the simulated SHSs. However, both DNSs and 3D-PTV measurements confirm a larger $\langle u^2 \rangle^+$ over the SHS.

The wall-normal Reynolds stress, $\langle v^2 \rangle_0^+$, over the smooth surface in Figure 6.8c agrees

with the DNS profiles. The profiles of $\langle v^2 \rangle_0^+$ over the SHS and the smooth surface in Figure 6.8c both start from zero at the wall as expected due to the non-permeable boundary condition. The overlap of $\langle v^2 \rangle_0^+$ for the smooth and SHS at $y^+ < 10$ also suggests negligible oscillation and movement of the SHS plastron in the wall-normal direction. However, $\langle v^2 \rangle_0^+$ of the SHS is smaller than the smooth surface in the inner layer, indicating smaller turbulence over the SHS. A similar trend is also seen in the DNS of Min and Kim (2004) over a flat SHS and the measurement of Abu Rowin et al. (2017) over an SHS with a roughness of $k^+ = 0.11$. The DHM of Ling (2017) shows a larger $\langle v^2 \rangle_0^+$ in the near-wall region of $y^+ < 10$ for SHSs with k^+ values as large as 0.89. The normalization based on the inner scaling of the corresponding surface results in larger values of $\langle v^2 \rangle^+$ over the SHS with respect to the smooth surface in Figure 6.8d. The $\langle v^2 \rangle^+$ of the DNS of Rastegari and Akhavan (2015) over the SHS in Figure 6.8d is also larger than $\langle v^2 \rangle^+$ of the smooth surface within $10 < y^+ < 30$. The $\langle v^2 \rangle^+$ of Seo et al. (2018a) overlaps with $\langle v^2 \rangle^+$ of the current measurement.

The spanwise component of normal Reynolds stress, $\langle w^2 \rangle_0^+$, over the smooth surface in Figure 6.8e falls between the DNS profiles of Gilbert and Kleiser (1991) and Rastegari and Akhavan (2015). This is expected since the Re_τ of the current measurements falls between the Re_τ of Gilbert and Kleiser (1991) and Rastegari and Akhavan (2015). Figure 6.8a and 6.8e show that the SHS modifies $\langle w^2 \rangle$ similarly to $\langle u^2 \rangle$. In Figure 6.8e, a larger $\langle w^2 \rangle_0^+$ is observed over the SHS at $y^+ < 7$ due to the spanwise slip (W_s), followed by a smaller $\langle w^2 \rangle_0^+$ farther away from the wall. This is consistent with the DNS of Min and Kim (2004) and Busse and Sandham (2012). The crossing-point for $\langle w^2 \rangle_0^+$ is closer to the wall than for $\langle u^2 \rangle_0^+$ due to a smaller magnitude of W_s compared with U_s. In Figure 6.8f, $\langle w^2 \rangle^+$ over the SHS is larger than the smooth surface across the measurement domain. A similar trend is observed for $\langle w^2 \rangle^+$ of Rastegari and Akhavan (2015) and Seo et al. (2018a) over the SHS in Figure 6.8f.

The Reynolds shear stress in Figure 6.8g overlaps with the DNS profiles. The $\langle uv \rangle_0^+$ of the SHS starts slightly larger than the smooth surface at $y^+ < 8$, while it is about 20% smaller farther away from the wall. This trend was previously observed by Ling (2017) and

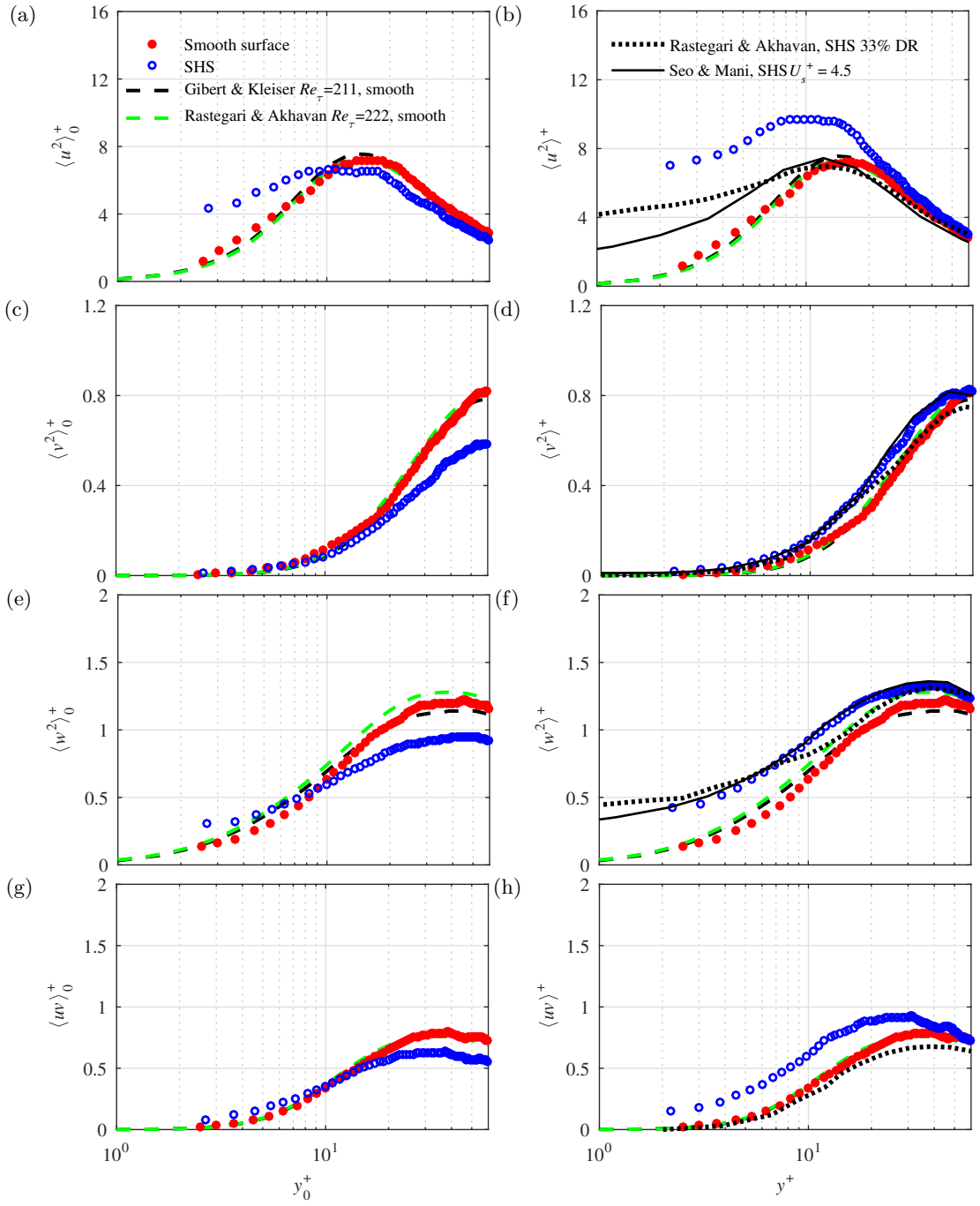

Figure 6.8: 3D-PTV measurement of (a, b) streamwise (c, d) wall-normal, (e, f) spanwise and (g, h) shear Reynolds stresses over the smooth and SHS. The Reynolds stresses normalized by the inner variables of the smooth surface are denoted by $\langle u_i u_j \rangle_0^+$ in the left-side plots and those normalized by the corresponding inner variables are indicated by $\langle u_i u_j \rangle^+$ in the right-side plots.

Abu Rowin et al. (2017). The level of increase in $\langle uv \rangle_0^+$ in the immediate vicinity of the SHS depends on the relative roughness of the SHS as discussed by Abu Rowin et al. (2017). Ling et al. (2016) noticed that $\langle uv \rangle_0^+$ over SHSs with large roughness ($k^+ > 1$) is larger than a smooth surface in both the inner and outer layer regions. In Figure 6.8h, $\langle uv \rangle^+$ of the SHS is larger than the smooth surface and gradually approaches the smooth surface with an increase of y^+. The $\langle uv \rangle^+$ profile from the DNS of Rastegari and Akhavan (2015) over the SHS in Figure 6.8h follows the smooth surface. The low Reynolds shear stress of the DNS is associated with the assumed flatness of the SHS. The organized structure of the simulated SHS of Rastegari and Akhavan (2015) can also result in smaller $\langle uv \rangle^+$ at the wall.

The distribution of viscous shear stress, $\tau_{v0}^+ = \partial \langle U \rangle_0^+ / \partial y_0^+$, Reynolds shear stress, $\tau_{R0}^+ = \langle uv \rangle_0^+$, and the total shear stress, τ_{t0}^+, over the smooth surface and the SHS are shown in Figure 6.9. The shear stresses are normalized by the wall shear stress of the smooth surface ($\tau_{w0} = \rho u_{\tau 0}^2$). Here ρ is the water density. It is observed that the viscous stress τ_{v0}^+ over the SHS is smaller than that over the smooth surface at $y^+ < 45$ due to the smaller wall-normal velocity gradient. Away from the wall, τ_{v0}^+ over the SHS overlaps with that over the smooth surface. The DHM measurement of Ling et al. (2016) also reported a similar trend of smaller τ_{v0}^+ over the SHS compared with the smooth counterpart. They observed that τ_{v0}^+ of the SHS approaches τ_{v0}^+ of the smooth surface at $y^+ = 50$. The Reynold shear stress τ_{R0}^+ of the SHS is larger than the smooth surface at $y^+ < 10$, due to the larger streamwise velocity fluctuations as seen in Figure 6.8a. Farther from the wall, τ_{R0}^+ of the smooth surface rapidly increases and becomes larger than τ_{R0}^+ of the SHS surface. The total shear stress τ_{t0}^+ over the SHS is smaller than that over the smooth surface within the measurement domain. As expected, the τ_{t0}^+ of the smooth surface approaches one at the wall. Over the SHS, τ_{t0}^+ increase with y^+ and reaches a local maximum at about $y^+ = 15$. The increase of τ_{t0}^+ over the SHS in the near wall region is also observed in the experiment of Ling et al. (2016).

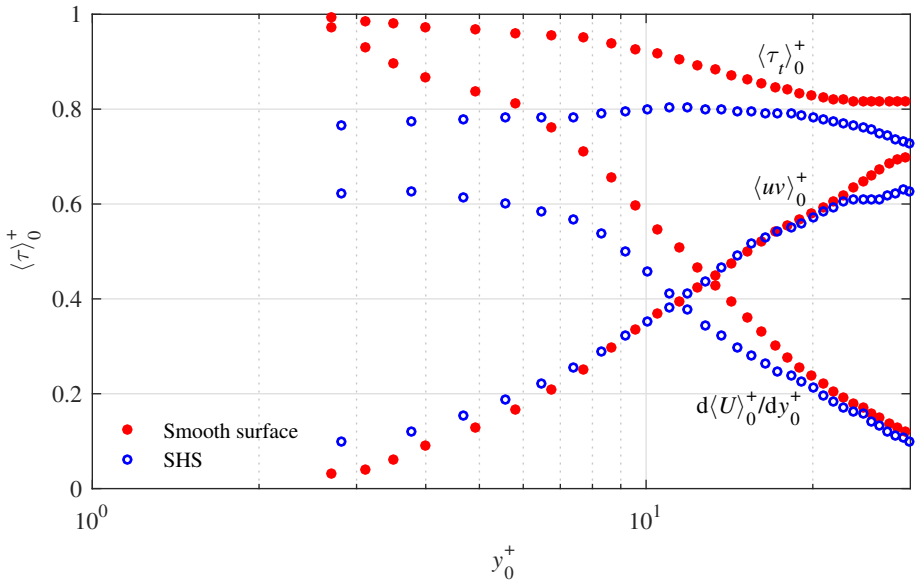

Figure 6.9: Profiles of viscous shear stress (τ_{v0}^+), Reynolds shear stress (τ_{R0}^+), and total shear stress (τ_{t0}^+) over the smooth and the SHS. The shear stresses are normalized by the wall shear stress of the smooth surface (τ_{w0}).

6.2.4 The shear-free pattern

For an SHS with an organized pattern of cavities or grooves, the morphology of the shear-free pattern can be inferred based on the surface pattern. However, this is more complex for a random surface due to the large spectrum of roughness elements and sensitivity of the plastron morphology to environmental parameters such as pressure and dissolved air. The recent visualization of Reholon and Ghaemi (2018) showed the presence of a full plastron for high DR ($> 16\%$) and isolated menisci of air, pinned between the tips and valleys of the roughness elements for lower DR ($< 8\%$) over an SHS with a random texture. To investigate the shear-free pattern of the SHS, the streamwise velocity measured in the immediate vicinity of the wall is used here.

The spatial distribution of temporally averaged velocity $\langle U^+\rangle_t$ in an $x-z$ plane with dimensions of $1000\lambda \times 1000\lambda$ (13×13 mm^2) at $y^+ = 3$ over the smooth and SHS are shown in Figure 6.10. The velocity data corresponds to $2.5 < y^+ < 3.5$, binned into a grid of $75\lambda \times 75\lambda$ (1×1 mm^2) windows in the $x-z$ plane. The $\langle U^+\rangle_t$ distribution over the smooth surface in Figure 6.10a shows a relatively uniform velocity distribution varying

between $\langle U^+ \rangle_t \approx 2$ to 4. The variation is due to statistical convergence of the data when divided into the 1×1 mm^2 windows. The $\langle U^+ \rangle_t$ contours over three separately fabricated SHSs are displayed in Figure 6.10(b-d). The contours show higher streamwise velocity up to $\langle U^+ \rangle_t \approx 6$ in patches as larger as $800\lambda \times 300\lambda$ (13.6×5.1 mm^2) in the x and z directions, respectively. The high-speed patches indicate regions of substantial streamwise slip due to a thicker underneath layer of air.

The DNS of Seo and Mani (2018b) showed that randomly distributed posts with similar height can interrupt the shear-free regions. This interruption resulted in smaller shear-free areas, which in turn generated a smaller effective slip length compared with an organized counterpart with streamwise-aligned posts. In the current investigation, the variation of protrusion height allows the shear-free regions to extend between the peaks of the larger protrusions without interruption by the smaller roughness elements. The SEM images and the profilometer measurements in Chapter 4 showed that the SHS roughness features with $\sim 20\mu$m height occur at a mean distance of about 12 mm, similar to the streamwise length of the shear-free regions (see Figure 6.10a). This shows that the smaller peaks ($R < 20\mu$m) do not disrupt the shear-free regions; the trapped air bubbles form a larger plastron pinned between the highest peaks. This is consistent with the DNS of Alamé and Mahesh (2019) over a more realistic SHS with a random texture based on a 3D scan of an SHS. They numerically showed that a thicker air layer can generate larger shear-free regions since small roughness elements are covered with the air plastron.

6.2.5 Drag estimation

In this section, the DR is estimated using several techniques including pressure drop measurements, estimation of wall-shear stress, the logarithmic law, and the formulation of Rastegari and Akhavan (2015). The results are used to evaluate the analytical estimation of DR by Fukagata et al. (2006), which explicitly includes the streamwise and spanwise slip lengths (l_x and l_z).

Drag reduction from pressure drop measurement is expressed as $(dp_0 - dp)/dp_0$, where

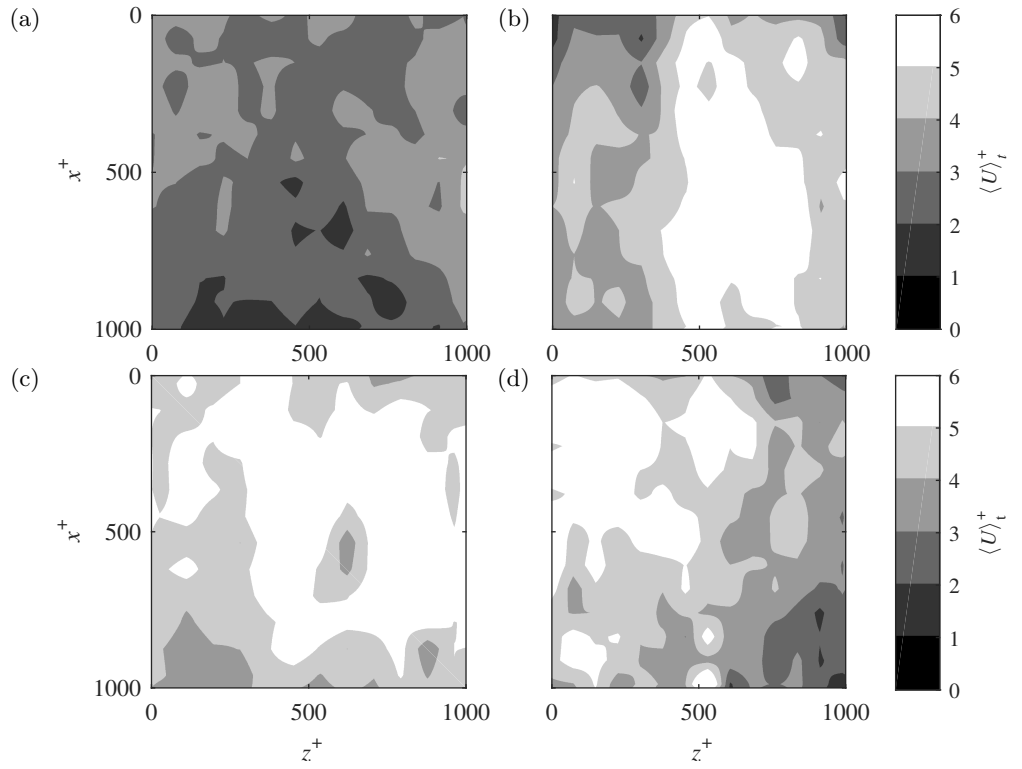

Figure 6.10: Mean velocity distribution over an $x - z$ plane for (a) smooth and (b, c, and d) three sample SHSs. The velocity is averaged within $2.5 < y^+ < 3.5$ and a grid with $75\lambda_0 \times 75\lambda_0$ windows is considered to generate the contours.

dp_0 is pressure drop along the smooth surface and dp is pressure drop along the SHS. Although this method is straightforward, it is subject to relatively large uncertainties due to the small pressure drop ($\sim$ 700 Pa) along the streamwise length of the SHS (240 mm) and partial coverage of the inner surface of the channel by the SHS coating. As previously discussed, the SHS is installed only at the top wall of the channel; however, the measured pressure drop is due to skin-friction on the whole interior of the channel. Therefor the drag reduction by the SHS is estimated as $DR = 2.16 \times (dp_0 - dp)/dp_0 = 32\%$, where following Gose et al. (2018) a factor of 2.16 is applied due to partial coverage of the channel interior. Based on the error propagation theory (Hughes and Hase, 2010) and the 2% uncertainty in pressure drop measurement, as discussed in Chapter 4 Section 4.5, the uncertainty of the estimated DR is $\pm 8\%$. To check the repeatability of DR, pressure drop measurements were performed over two additional SHSs, showing 34 and 30% DR.

Ling et al. (2016) estimated the DR over an SHS from direct measurement of wall shear stress (τ_w) as a summation of viscous stress ($\tau_w^\mu = \mu\partial\langle U\rangle/\partial y$) and Reynolds shear stress ($\tau_w^R = -\rho\langle uv\rangle$), where μ is the dynamic viscosity. As seen in Figure 6.8g, the Reynolds shear stress is expected to be negligible at $y^+ = 0$ over the current SHS due to its small roughness. Therefor the DR is estimated here as $(\tau_{w,0}^\mu - \tau_w^\mu)/\tau_{w,0}^\mu$, where the subscript 0 refers to wall shear stress over the smooth surface. The calculated DR is 38% based on wall shear stress estimated from the linear velocity gradient at $2.5 < y^+ < 3.5$.

The third method for estimating DR is based on a modification of the logarithmic law of the mean velocity profile as investigated by Min and Kim (2004), Busse and Sandham (2012), and Rastegari and Akhavan (2019). For an SHS with DR, the von Kármán constant, κ, remains unchanged while the intercept of the logarithmic profile B, increases as seen in Figure 6.4a. Following the formulation of Bechert et al. (1997) in a study of riblet surfaces, DR can be obtained from

$$DR = \frac{-\Delta B}{(2c_{f0})^{-1/2} + (2\kappa)^{-1}}, \tag{6.1}$$

where ΔB is the change of the intercept of the logarithmic profile between the smooth and SHS, and the skin-friction coefficient is defined as $c_f = \tau_w/(\frac{1}{2}\rho U_b^2)$. The estimated DR from 6.1 is 36%. This method underestimates the DR by 4.0% compared with the DR obtained from the reduction of the wall shear stress as shown in Table 6.2. The lower DR from 6.1 can be associated with the effect of the surface structure since ΔB is a function of surface structure while c_f depends on Re (Rastegari and Akhavan, 2019).

Rastegari and Akhavan (2015) developed an expression to estimate DR over a wall with a slip-free boundary by decomposing the drag into a term due to slip velocity and another term due to modifications of the Reynolds shear stress based on the original formulation of Fukagata et al. (2002). This decomposition of DR is given by

$$DR = \frac{U_s}{U_b} + \left(1 - \frac{U_s}{U_b}\right)\left(\frac{3\varepsilon}{1 - 3I^+}\right). \tag{6.2}$$

Here $\varepsilon = I^{+0} - I^+$ is the difference between the weighted integrals of $\langle uv\rangle$ over the

smooth and SHS, obtained from

$$I^+ = \int_0^1 (1-\delta)\langle uv\rangle^+ d\delta, \tag{6.3}$$

where $\delta 2y/H$ is the normalized wall-normal coordinate. The integrals over the two surfaces in Equation 6.3 were carried out within $2.5 < y^+ < 90$ ($0.01 < \delta < 0.4$). The limited range of integration does not affect the estimated DR due to the negligible value of $(1-\delta)\langle uv\rangle^+$ at $y^+ < 2.5$ and farther away from the wall at $y^+ > 90$. The estimated DR from 6.2 is 35%.

The expression of DR from the theoretical study of Fukagata et al. (2006) includes both slip lengths (l_x and l_z) as follows:

$$\kappa F_0 + lnRe_{\tau 0} = (1-DR)\kappa l_{x0}^+ + \sqrt{1-DR}ln\left(\sqrt{1-DR}Re_{\tau 0}\right) + \sqrt{1-DR}\kappa F. \tag{6.4}$$

Here F_0 is obtained from $U_b/u_\tau = (\kappa^{-1}lnRe_{\tau 0} + F_0)$ as expressed by Dean (1978) and is equal to 2.9. The parameter F is a function of the non-dimensionalized spanwise slip length (l_z^+). Fukagata et al. (2006) estimated F based on an exponential fit obtained from the numerical results of Min and Kim (2004) as

$$F = 4exp[-(0.14l_z^+)^{0.7}] - 0.8. \tag{6.5}$$

This function results in $F \leq 0.75$ using the spanwise slip length obtained in subsection 6.2. The numerical solution of 6.4 results in a DR of 32%, which underestimates DR by 3-6% compared with the other techniques as shown in Table 6.2. The low DR from 6.4 is associated with the estimated F from the DNS of Min and Kim (2004), which assumes a flat boundary condition. The analysis shows that spanwise slip should be measured over a wider range of conditions including Re_τ and k^+ to develop more accurate analytical models for the estimation of drag over SHS.

6.3 Conclusion

The 3D-PTV measurement of the mean velocity profiles over the SHS showed an increase of the mean streamwise velocity in the near-wall region, confirming the presence of a streamwise slip velocity. The extrapolation of the linear viscous sublayer to the wall indicated a

Equation for estimation of DR	DR %
$DR = 2(dp_0 - dp)/dp_0$	32 $\pm$8
$DR = (\tau^{\mu}_{w,0} - \tau^{\mu}_{w})/\tau^{\mu}_{w,0}$	38
$DR = \frac{-\Delta B}{(2c_{f0})^{-1/2}+(2\kappa)^{-1}}$	36
$DR = \frac{U_s}{U_b} + \left(1 - \frac{U_s}{U_b}\right)\left(\frac{3\varepsilon}{1-3I^+}\right)$	35
$\kappa F_0 + lnRe_{\tau 0} = (1-DR)\kappa l^+_{x0} + \sqrt{1-DR}ln\left(\sqrt{1-DR}Re_{\tau 0}\right) + \sqrt{1-DR}\kappa F$	32

Table 6.2: Summary of the estimated DR from pressure drop measurement, wall-shear stress, logarithmic law, the formulation of Rastegari and Akhavan (2015), and the analytical expression of Fukagata et al. (2006).

slip velocity of 0.27 m/s (30% of the bulk velocity), which is associated with a streamwise effective slip length of 96.5 μm (5.9λ). The scatter plot of spanwise particle velocity showed a large number of tracers with finite spanwise velocity at the SHS. The spanwise slip velocity was estimated to be 0.018 m/s from averaging the absolute values of spanwise velocity of the tracers. This is equivalent to a 95.8 μm (5.9λ) spanwise effective slip length, which indicates an SHS with an isotropic slip with a similar slip length in the streamwise and spanwise directions. Farther away from the SHS, the effect of the slip velocity diminished and a smaller streamwise and spanwise velocity was observed compared with the smooth surface.

When dimensional Reynolds stresses over the smooth and SHS were compared at the same flow rate the streamwise and spanwise Reynolds stresses were larger in the near-wall region of the SHS. This indicates the presence of both streamwise and spanwise slip. The peaks of the streamwise and spanwise Reynolds stresses, when normalized by the smooth and the corresponding inner scaling, were also shifted closer to the wall due to the thinner inner layer over the SHS. The wall-normal Reynolds stress over the SHS remained comparable to the smooth surface in the near-wall region due to the non-permeable boundary condition of both surfaces. In the immediate vicinity of the wall, the Reynolds shear stress over the SHS was slightly larger than that of the smooth surface. All components of the Reynolds

stress tensor were smaller over the SHS farther away from the surface. However, when the Reynolds stresses were non-dimensionalized using the corresponding inner scaling of each surface they had a larger value with respect to the smooth surface across the inner layer. This indicates that normalization of Reynolds stresses using inner scaling does not result in overlap of Reynolds stress profiles when a slip velocity is present.

The patterns of the shear-free regions were also investigated over the SHS using contours of near-wall mean streamwise velocity in a streamwise/spanwise plane at $y^+ = 3$. The results showed streamwise-elongated patches of high streamwise velocity over the SHS, which represent the morphology of the underneath air layer. The high-speed regions were up to $800\lambda \times 300\lambda$ (13.6×5.1 mm^2) in the streamwise and spanwise directions, respectively. The SEM images and the profilometer measurements also showed that the largest roughness features with $\sim 20\mu$m height occur at a mean distance of about 12 mm similar to the streamwise length of the largest shear-free regions. Therefore, the smaller roughness peaks do not disrupt the shear-free regions as the plastron is pinned between the highest peaks. The drag reduction (DR) over the current SHS was estimated and evaluated using various techniques. The results indicated DR of about 30 to 38% over the investigated SHS.

Chapter 7

Effect of Reynolds number on turbulence structures over a superhydrophobic surface

7.1 Introduction

Experimental investigations have studied the effect of Re on DR obtained by an SHS. The experiments show two possible trends of DR increase with increasing Re (Jung and Bhushan, 2009; Srinivasan et al., 2015; Daniello et al., 2009), and reduction of DR with increasing Re (Gogte et al., 2005; Reholon and Ghaemi, 2018), depending on whether the air plastron has been maintained with increasing Re. Jung and Bhushan (2009) measured pressure drop along a channel flow with superhydrophobic walls and compared the values with that of hydrophilic walls to estimate DR at several Re within the laminar regime and a single Re of 4200 (defined based on bulk velocity and channel height) in the turbulent regime. They observed a DR of 30% in the turbulent regime, and 12% DR in the laminar regime. Srinivasan et al. (2015) measured the drag of an SHS in a Taylor-Couette apparatus operating in the turbulent regime. They observed 6% at Re of 2×10^4 that increases to 22% at Re of 8×10^4, where Re was defined based on the gap of the two cylinders and the velocity of the surface velocity of the inner cylinder. Daniello et al. (2009) measured negligible DR for Re smaller than 2500 in a turbulent channel flow. Beyond this Re, DR rapidly increases to 50% for an SHS with a micro-ridge pattern and was sustained up to

the highest investigated Re of 9500. In contrast, with an increase of Re, Gogte et al. (2005) observed attenuation of DR for a hydrofoil coated with a superhydrophobic drag. In that investigation, DR was estimated by measuring the airfoil drag (friction and form drag) in the laminar regime. Aljallis et al. (2013) also observed up to 30% DR for a superhydrophobic plate towed in a water channel compared to a control plate with no coating. However, at higher Re in the turbulent regime, an increase of drag was observed relative to the control plate. In the turbulent regime, Reholon and Ghaemi (2018) measured the drag of the aft-section of an axisymmetric model and observed a gradual reduction of DR from 36 to 6% with increasing Re. Their visualization of the surface showed a full air plastron at lower Re with $DR > 16\%$, while the plastron evolved into isolated menisci of air at higher Re with $DR < 8\%$.

The variation of water slip over the SHS in terms of slip velocity and length in the turbulent regime, and its subsequent effect on turbulence, has rarely been investigated. Daniello et al. (2009) and Reholon and Ghaemi (2018) observed that an increase of flow Re over SHS increases the slip velocity (in physical units). The investigation by Daniello et al. (2009) does not provide any information on the slip length. The particle tracking velocimetry measurements of Reholon and Ghaemi (2018) showed that slip length slightly reduced with increasing Re, as the air plastron diminished. To the authors' knowledge, there has been no measurement of the effect of Re variation on turbulence over an SHS. The DNS of Martell et al. (2010) simulated the flow over a no-slip and an SHS in one side of a turbulent channel flow for three fixed friction Reynolds numbers (i.e., constant pressure gradient): $Re_\tau = 180, 395$, and 590. Over the SHS, they modelled the flow with alternating regions of slip at the air interface and no-slip at the solid interface. They found that the slip velocity over the SHS is not a function of Re where similar slip velocity to the bulk velocity is seen at different Re cases. However, Reynolds stresses over the SHS do change with Re. They found that the peaks of Reynolds stresses increase and shift toward the SHS with increasing Re, when normalized by the average inner scaling of the upper (SHS) and bottom (no-slip surface) walls of the channel. The numerical simulation of Lee et al. (2015)

considered the Re variation on near-wall turbulence over an SHS by simulating a channel flow over an SHS with streamwise microgrooves at three Re of 2800, 6785, and 10975 (based on channel half-height). When normalized Reynolds stresses are considered, at the lowest Re of 2800, Reynolds stresses over the SHS were larger than those of the no-slip surface. However, at Re 6785, and 10975, the Reynolds stresses of the SHS became smaller than those of the no-slip surface in the buffer layer region.

In this chapter, we experimentally investigated variation of the slip boundary condition and the Reynolds stresses over an SHS installed in a turbulent channel flow when Re varies from 6,000 to 10,000 (based on full channel height), equivalent to friction Reynolds number range of $Re_\tau = 200$ to 280, based on friction velocity and half-channel height. The SHS has a random texture and is fabricated using a spray coating. Unlike the previous experimental investigations, the current study is performed at a relatively constant DR to understand the influence of the change of Re on the slip boundary and the near-wall statistics over the SHS. Time-resolved two-dimensional particle tracking velocimetry (2D-PTV), with high digital resolution is used for accurate measurement of slip velocity and length. In addition, time-resolved three-dimensional PTV (3D-PTV) based on shake-the-box algorithm (Schanz et al., 2016) is performed to measure near-wall Reynolds stresses. The mean velocity profile and Reynolds stresses are compared with measurements over a no-slip surface.

7.2 Results

Experiments over the smooth and the SHS were performed at the same flow rates. Five Re starting from 6,200 to 9,400 were tested, see Table 7.1. Re is defined here as $U_b H/\nu$, where U_b is the bulk velocity (0.95 to 1.46 m/s). Although the experiments over the smooth surface and the SHS were performed at the same flow rates as the flow meter specified, the 2D-PTV measurements reviled a small discrepancy between the tests for $Re = 180$. This variation is within the repeatability of the flow meter, as previously noted. Henceforth, Re over the smooth surface and the SHS will be noted by a nominal Re, as shown in Table 7.1.

The mean velocity profiles and the Reynolds stresses from 2D-PTV and 3D-PTV are

Nominal Re	6200	7200	8000	8600	9400
			Smooth surface		
Re	6140	7040	7880	8570	9330
U_b (m/s)	0.95	1.1	1.22	1.33	1.45
			SHS		
Re	6230	7220	8030	8700	9380
U_b (m/s)	0.97	1.11	1.25	1.35	1.46
P_a (kPa)	96.5	97.5	97.8	98.1	99.8

Table 7.1: Summary of the bulk flow parameters over the smooth and SHS

investigated in this section for the five Re. As was explained in Chapter 3 Section 3.2 page 20, the smooth surface (no slip boundary condition) and the SHS were installed at the top wall of the channel, where $y = 0$. The superscript, $+$, represents parameters normalized by the inner scales (u_τ and λ) of the corresponding surface. To study the impact of the change on Re in physical units, the data is also normalized by a common parameter, which is chosen to be the bulk velocity at the smallest $Re = 6200$, shown by the subscript, b.

7.2.1 Measurement evaluation over the smooth surface

The 2D-PTV and 3D-PTV measurements over the smooth surface were conducted to evaluate the state of the turbulent flow at the measurement location, provide a reference for comparison with the SHS, and evaluate the accuracy of the measurements. The latter was carried out through comparison of the measurements with DNS of the turbulent channel flow by Kristoffersen and Andersson (1993); Iwamoto et al. (2002) at $Re_\tau = 195$ and 300, respectively. These two DNS data sets were chosen because they are close to the smallest and largest Re_τ of the experiments, as seen in Table 7.2.

The inner variables over the smooth surface were estimated from the Clauser method (Clauser, 1956) by fitting the data on the log-law, expressed as $u^+ = \frac{1}{\kappa} ln(y^+) + B$. The friction velocity and viscous length of the smooth surface varied from $u_\tau = 0.062$ to 0.088 m/s and $\lambda = 15$ to 10.9 μm, respectively. The friction Reynolds number of the smooth surface, Re_τ, varied from 200 to 283. A summary of inner-scaling parameters for the five Re over the smooth surface, as obtained from 2D PTV measurement, is presented in

Nominal Re	6200	7200	8000	8600	9400
			Smooth surface		
u_τ (m/s)	0.062±5e-3	0.069±5e-3	0.076±5e-3	0.082±5e-3	0.088±6e-3
λ (μm)	15.0±1.3	13.5±1.1	12.3±0.9	11.4±0.7	10.6±0.8
τ_w (Pa)	3.83±0.62	4.75±0.69	5.76±0.76	6.70±0.82	7.72±1.10
Re_τ	200±16	222±16	245±16	264±16	283±19
$\lambda_{clauser}$ (μm)	15.2	13.9	12.6	11.8	10.9
			SHS		
u_τ (m/s)	0.049±4e-3	0.053±4e-3	0.059±4e-3	0.063±5e-3	0.067±5e-3
λ (μm)	19.1±1.6	17.3±1.4	15.8±1.1	14.8±1.0	13.9±1.1
τ_w (Pa)	2.39±0.39	2.80±0.42	3.47±0.47	3.95±0.63	4.47±0.67
Re_τ	157±13	174±13	190±13	203±16	215±16
U_s (m/s)	0.25±0.02	0.28±0.02	0.29±0.03	0.31±0.03	0.34± 0.04
U_s/U_b (%)	26	25	23	23	23
U_s/u_τ	5.1±0.4	5.2±0.3	4.9±0.5	4.9±0.5	5.0±0.6
l_s (μm)	97.5±8.9	92.2±6.3	77.5±8.3	72.1±7.6	69.6±9.1
l_s/λ	5.1±0.4	5.2±0.3	4.9±0.5	4.9±0.5	5.0±0.6
k^+	0.32	0.36	0.4	0.43	0.46
DR (%)	38±5	41±4	40±3	41±3	42±2
DR_{dp} (%)	33±6	35±6	35±6	37±6	39±6

Table 7.2: A summary of the parameters of the experiments at different flow rates over the smooth and SHS. The uncertainty of detecting the wall location resulted in variations of estimating the inner scaling, U_s, and l_s. The uncertainty of the DR by the pressure drop measurement (DR_{dp}) is based on the error propagation theory.

Table 7.2. The semi-logarithmic presentation of the normalized mean streamwise velocity ($u^+ = \langle U \rangle / u_\tau$) versus normalized wall-normal distance $y^+ = y/\lambda$ over the smooth surface from 2D-PTV is shown in Figure 7.1a. The figure shows that 2D PTV data overlaps with the log-law, while the buffer and linear viscous sublayers are also observed near the wall. The 2D PTV measurements are accurate up to the near-wall location of $y^+ \sim 2$ since the data overlaps with $u^+ = y^+$ profile in the linear viscous sublayer. In the analysis of slip length and slip velocity over the SHS, we use 9 data points from 2D-PTV measurement within $2 < y^+ < 3.5$ to obtain the wall-normal gradient of the mean velocity at the wall. This range is chosen to reduce the error of the law-of-the-wall at $y^+ = 5$ (George, 2013). The parameters include maximum velocity at the center of the channel, U_m, wall shear stress, $\tau_w = \rho u_\tau^2$, where ρ is the water density, and absolute static pressure in the test

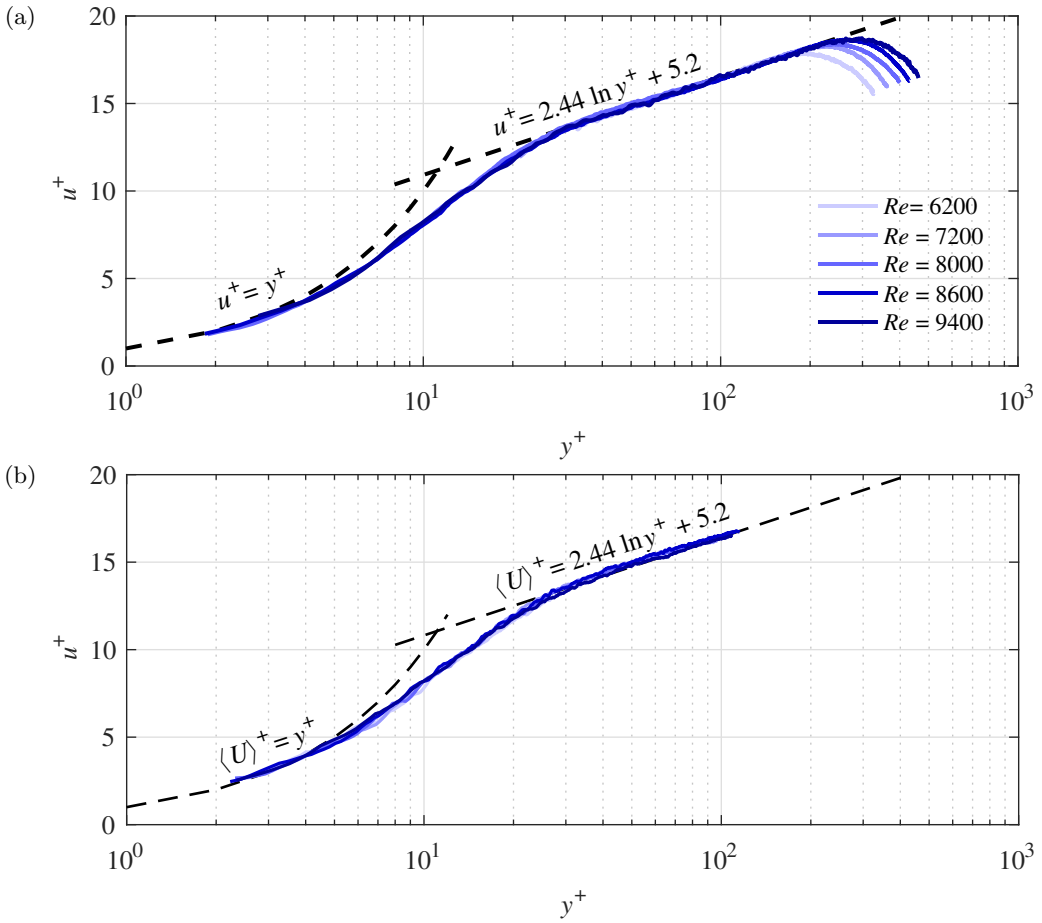

Figure 7.1: Semi-logarithmic presentation of the mean streamwise velocity profile over the smooth surface from (a) the 2D PTV and (b) the 3D PTV measurements. The data is normalized by the inner scale of each case.

section, P_a. As seen in this table, P_a increases from 96.8 to 99.2 kPa with increasing Re.

The streamwise velocity profiles over the smooth surface for $Re_\tau = 200$ to 283 from the 3D-PTV measurement are shown in semi-logarithmic axes in Figure 7.1b. The data is normalized by the inner variables estimated from the 2D-PTV, as listed in Table 7.2. The data at $y^+ < 4$ is discarded due to discrepancy of 3D-PTV with respect to $u^+ = y^+$ of the linear viscous sublayer, especially for the higher Re. The discrepancy is associated with the large size of the fluorescent tracers (10 μm) with respect to λ, which varies from 15 to 10.6 μm with increasing Re. Farther away from the wall, the u^+ profiles coincide with the log-law until $y^+ \approx 100$, which is the upper limit of the 3D measurements.

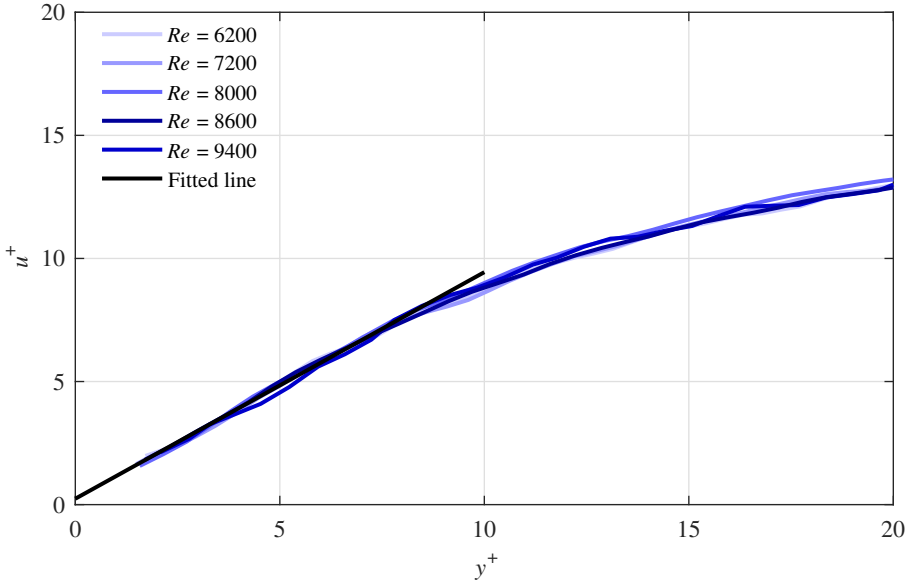

Figure 7.2: Mean streamwise velocity profile in the inner layer over the smooth surface from 2D PTV.

The mean velocity for $y^+ < 20$ from the 2D-PTV is plotted in linear axes in Figure 7.2. The inner scaling used to normalize velocity and wall-normal distance in Figure 7.2 are estimated based on the wall-normal gradient of mean velocity in the linear viscous sublayer ($2 < y^+ < 3.5$). The estimated wall-shear stresses from the velocity gradient are within 4-8% of those estimated from Clauser's method in Figure 7.1a. Thus, this method will be used to estimate the inner scaling parameters over the SHS. Figure 7.2 also illustrates that u^+ over the smooth surface approaches negligible at the wall, which is in agreement with the no slip boundary condition.

Reynolds stresses of the turbulent channel flow over the smooth surface from 3D-PTV for the near-wall region of $y^+ < 50$ are shown in Figure 7.3. The left-side plots of Figure 7.3 (a, c, e, g), show Reynolds stresses and wall-normal distance in outer-scaling. All Reynolds stresses are normalized by U_b^2 of $Re = 6200$ (smallest Re), as denoted with subscript b, and wall-normal distance is shown based on channel height. As expected, Reynolds stresses increase with increasing Re. Due to a thinner inner layer at higher Re, the peak of the Reynolds stresses also shifts toward the wall at larger Re. This is seen for all Reynolds

stresses, except $\langle v^2 \rangle_b$ which peaks at $y^+ > 50$. The profiles of the Reynolds stresses approach zero with reducing wall-normal distance, as expected for a no-slip boundary condition.

In the right-side plots of Figure 7.3 (b, d, f, h), the Reynolds stresses at each Re are normalized by their corresponding inner scaling, $\langle u_i u_j \rangle^+ = \langle u_i u_j \rangle / u_\tau^2$. The normalization by the inner scaling results in overlap of the $\langle u^2 \rangle^+, \langle v^2 \rangle^+, \langle w^2 \rangle^+$ profiles for different Re, while a larger variation is observed for $\langle uv \rangle^+$. This relative overlap is expected near the wall when Reynold stresses are normalized by inner-scaling. The DNS of Kristoffersen and Andersson (1993) at $Re_\tau = 195$ and Iwamoto et al. (2002) at $Re_\tau = 300$ are also presented to compare with the smallest and largest Re_τ of the 3D-PTV, respectively. The measured Reynolds stresses fall between the low and the high Re data from the DNS.

7.2.2 Mean velocity over the SHS

Figure 7.4 shows the near-wall streamwise velocity profiles over the SHS from 2D PTV in linear axes. The inner scales are estimated from the wall-normal gradient of mean velocity at $2 < y^+ < 3.5$, as summarized in Table 7.2. As can be seen from Figure 7.4, u^+ profiles of the SHS at different Re overlap with a subtle discrepancy. It is also noted that the normalized slip velocity, $u_s^+ = U_s / u_\tau$, for all Re numbers approaches ~ 5.0 when the linear fit obtained from the data in $2 < y^+ < 3.5$ is extrapolated to $y^+ = 0$.

To better investigate the effect of the change of Re on the slip boundary condition over the SHS, U_s is plotted against Re in Figure 7.5a , and listed in Table 7.2. The error bars are based on the uncertainty in estimating the wall location, as discussed in Chapter 3. Due to the higher velocity gradient at the wall, the error in estimating U_s increases with Re. As shown in Figure 7.5a, U_s gradually increases from 0.25 to 0.34 m/s with increasing Re. Although no evaluation of accuracy or comparison with a no slip surface was provided, the PIV of Daniello et al. (2009) also observed an increase of U_s over an SHS with microgrooves as Re increased. The microscopic PTV over a body-of-revolution coated with a superhydrophobic layer of Reholon and Ghaemi (2018) also showed a larger Us at larger Re over the SHS. The DNS of Lee et al. (2015) also demonstrated the same trend of an increase of U_s as

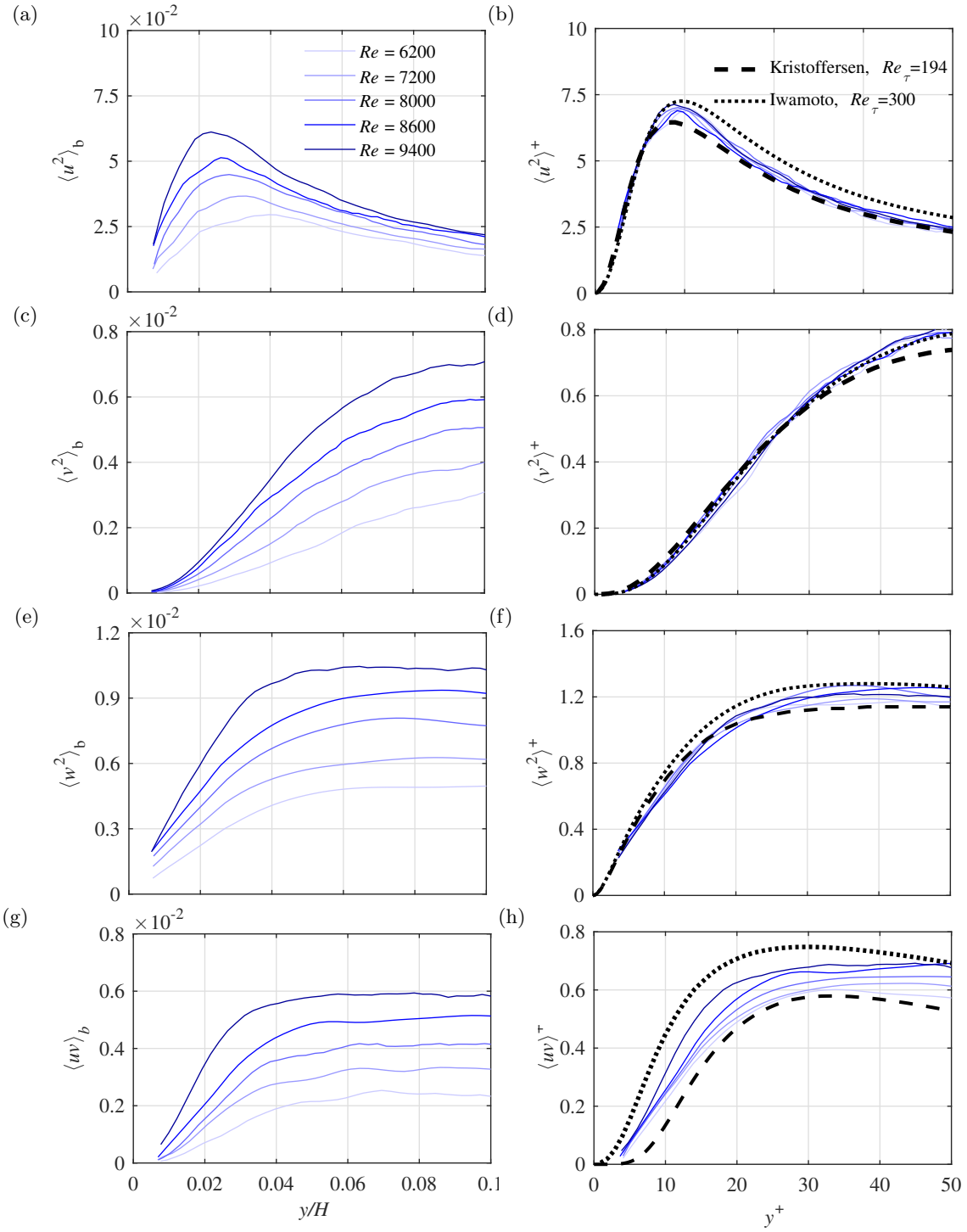

Figure 7.3: 3D-PTV measurement of $(a-b)$ streamwise, $(c-d)$ wall-normal, $(e-f)$ spanwise and $(g-h)$ shear Reynolds stresses over the no-slip smooth surface. The left side figures are normalized by U_b of the flow at the lowest Re and the channel height, while the right-side figure normalized by the inner scaling of the corresponding surface.

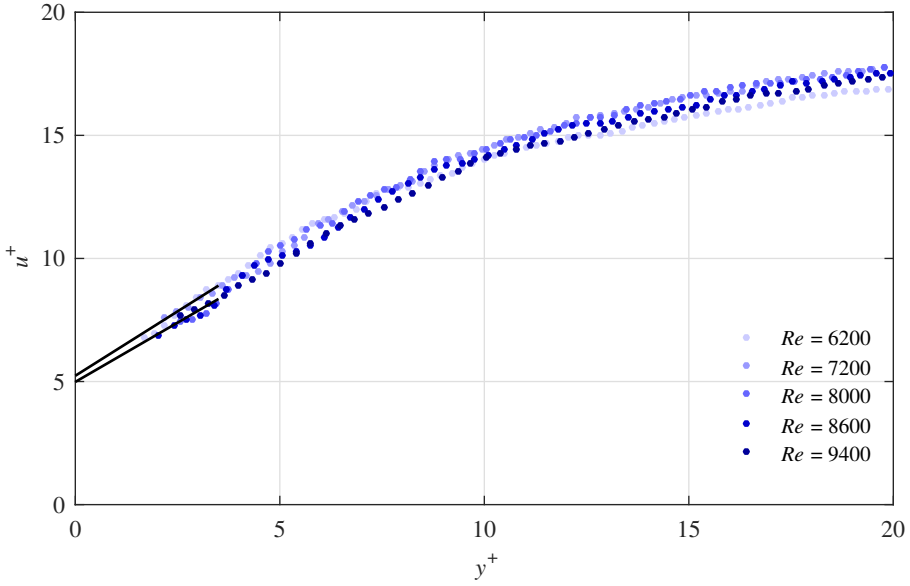

Figure 7.4: Mean streamwise velocity profile over the SHS at different Re normalized by the corresponding inner scaling. The fitted lines are only shown for $Re = 6200$ and $Re = 9400$ for clarity.

Re increases when it modelled the flow over the SHS with regions of slip and no-slip based on the surface structure. The effect of Re on u_s^+ is also plotted in Figure 7.5b. We noticed that u_s^+ over the current SHS remains relatively stable at ~ 5.0 at different Re. The DNS of Martell et al. (2010) reported a trend of a larger u_s^+ at higher Re when it modelled the flow over the SHS with the same method of Lee et al. (2015). They associated the increase of u_s^+ to the increase of the spacing between the microfeatures in wall units.

As shown in Table 7.2, U_s/U_b over the SHS is also relatively constant, varying from 26 to 23% with increasing Re. The DNS of Martell et al. (2010) also reported a constant U_s/U_b when they simulated the flow over an SHS at three Re_τ. Rastegari and Akhavan (2015) obtained an analytical equation for the DR of an SHS based on the original formulation of Fukagata et al. (2002). They decomposed the expression for DR into a term due to the direct effect of slip velocity, which is U_s/U_b, and a second term due to turbulence modification and secondary mean flows (for patterned surfaces). Therefore, the difference between DR and U_s/U_b percentage in Table 7.2 shows the contribution of turbulence attenuation to DR, which varies from 11 to 16% with increasing Re. Therefore, turbulence attenuation slightly

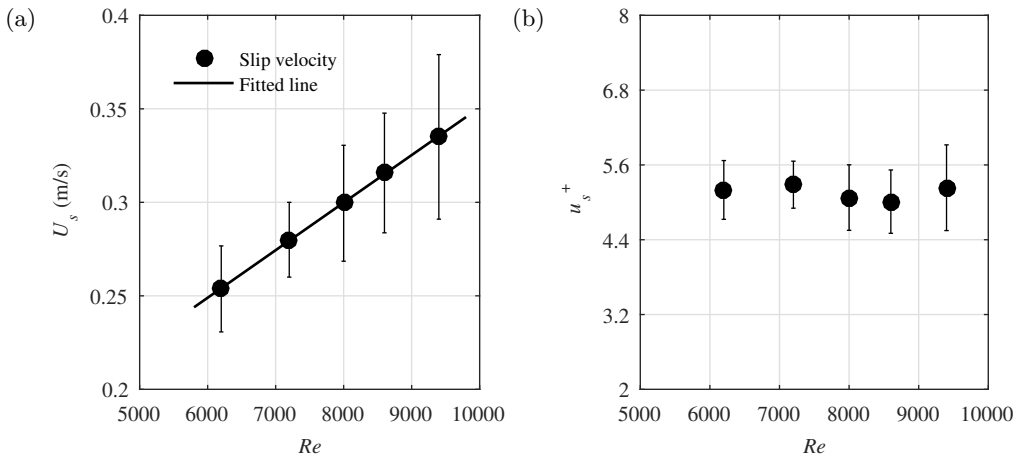

Figure 7.5: Effective slip velocity measurement over the SHS at different Re (a) in terms of m/s and (b) normalized by the corresponding inner scaling. The error bars represent the uncertainty in estimating the wall location from 2D-PTV.

increases at higher Re.

The change of l_s with Re is also investigated in Figure 7.6. Similar to Figure 7.5, the error bars in Figure 7.6 represent the uncertainty of estimating the wall location from 2D-PTV. As displayed in Figure 7.6a, l_s, decreases steadily from 97.5 μm at $Re = 6200$ to 69.6 μm at $Re = 9400$. This reduction is associated with a decrease of the air plastron thickness as the test-section pressure increases, and therefore, the solubility of air in water increases. As Dilip et al. (2014) observed, an increase in the solubility of water at higher pressure dissolves part of the air layer in water. Ling et al. (2017) carried out an experiment over a hierarchical SHS with stationary and moving water. In the under-saturated water case, they found the mass diffusion of the plastron over the SHS is negligible for the stationary flow during the test period (about 50 minutes), while in the moving flow case, a dramatic reduction of the air layer (fast diffusion of the plastron) resulted in a complete loss of the air layer after about 5.5 minutes. The shadowgraphy PTV of Reholon and Ghaemi (2018) showed that the higher Re can inherit the plastron depletion where they observed a full exposure of the SHS roughness elements at the highest tested $Re = 1.5 \times 10^6$. The impact of Re on $l_s^+ = l_s/\lambda$ over the current SHS is shown in Figure 7.6b. Similar to the trend of u_s^+ in Figure 7.5b, l_s^+ in Figure 7.6b remains comparable at different Re.

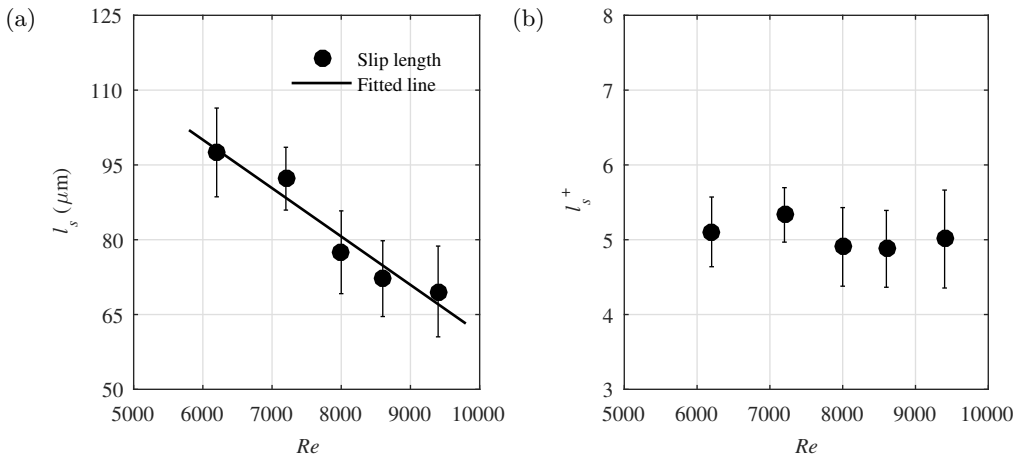

Figure 7.6: Slip length measurement over the SHS at each Re (a) in terms of m/s and (b) normalized by the corresponding inner scaling. The error bars represent the uncertainty in estimating the wall location from 2D-PTV.

In the current investigation, DR is estimated from the difference between the wall shear stress of the smooth surface and the SHS. The DR over the SHS increases from 37 to 42% as Re increases (see Table 7.2), which is roughly constant within the uncertainty of the measurement technique. The DR over the SHS was also directly measured using the pressure drop measurements. The DR from the pressure drop measurement is expressed as $DR_{dp} = 2.1 \times (dp_0 - dp)/dp_0$. Here, dp_0 and dp are the pressure drop measurements over the smooth and SHS, respectively. The factor 2.1 is included since the SHS covers 92% of the distance between the pressure ports and the pressure measurement only exists at the top wall of the channel. The uncertainty of DR_{dp} in Table 7.2 is estimated from the error propagation theory and the 2% uncertainty in pressure drop measurement, as discussed in Chapter 4 Section 4.5. As shown, DR_{dp} also increases with increasing Re, agreeing with the DR estimated from the difference in the wall shear stress. However, the pressure drop measurement underestimates the DR by $\sim 5\%$.

With increasing Re, the normalized root-mean-square of surface roughness, $k^+ = R/\lambda$, increases from 0.32λ to 0.46λ, as listed in Table 7.2. Bidkar et al. (2014) suggested that the optimum k^+ is equal to 0.5 where the SHS can provide the highest Re. The measurements of Ling et al. (2016) also agreed with this observation when they showed an increase of

DR from 9% to 36% as k^+ increases from 0.43 to 0.68, respectively. Beyond this range, for $k^+ > 0.68$, DR started to decline until reaching a drag increase over an SHS with $k^+ = 3.28$. Reholon and Ghaemi (2018) also examined the effect of the surface roughness on the DR. They observed an attenuation of DR as k^+ increased beyond 0.5.

The semi-logarithmic profiles of u^+ over the SHS from the 2D-PTV for different Re are presented in Figure 7.7a. As can be seen, there is an upward shift of u^+ over the SHS at all Re cases when compared with the law of the wall and the log law. This shift, which is due to the presence of slip velocity, was observed by Min and Kim (2004), using numerical simulation, and in the experiments of Ling et al. (2016), as well as Abu Rowin et al. (2017). It can also be concluded from Figure 7.7a that, when a similar DR is maintained, the change of Re has a negligible effect on the semi-logarithmic u^+ profiles, when a similar DR is maintained. Reholon and Ghaemi (2018) observed a significant increase of the semi-logarithmic profiles of u^+ over the SHS at different Re. The different trend of their investigation is due to the large change of the DR percentages, which varied from 23% to 1% at Re from 5.0×10^5 to 1.2×10^6. Figure 7.7b illustrates the semi-logarithmic profiles when the slip velocity is subtracted (i.e., $u^+ - u_s^+$). As can be seen, the profiles overlap with the law-of-the-wall and the log-law of a smooth wall. This trend was seen in the DNS of Min and Kim (2004) when they modelled the flow over an SHS with a non-zero streamwise slip and zero spanwise slip.

7.2.3 Reynolds stress over the SHS

All non-zero components of the Reynolds stress tensor, $\langle u_i u_j \rangle$, for turbulent flow over the SHS in the near-wall region of $y/H < 0.10$ are measured using 3D-PTV and shown in Figure 7.8. The profiles of Reynolds stresses over the SHS are normalized by U_b of the lowest Re in Figure 7.8(a, c, e, g), while in Figure 7.8(b, d, f, h), they are normalized by the inner scales of each case. For ease of comparison, Reynolds stress profiles for the smooth surface are also repeated in Figure 7.8.

In the near-wall region, where the effect of slip velocity is larger, $\langle u^2 \rangle_b$ of the SHS is larger than for the smooth surface, as seen in Figure 7.8a. The peak of $\langle u^2 \rangle_b$ over the SHS are

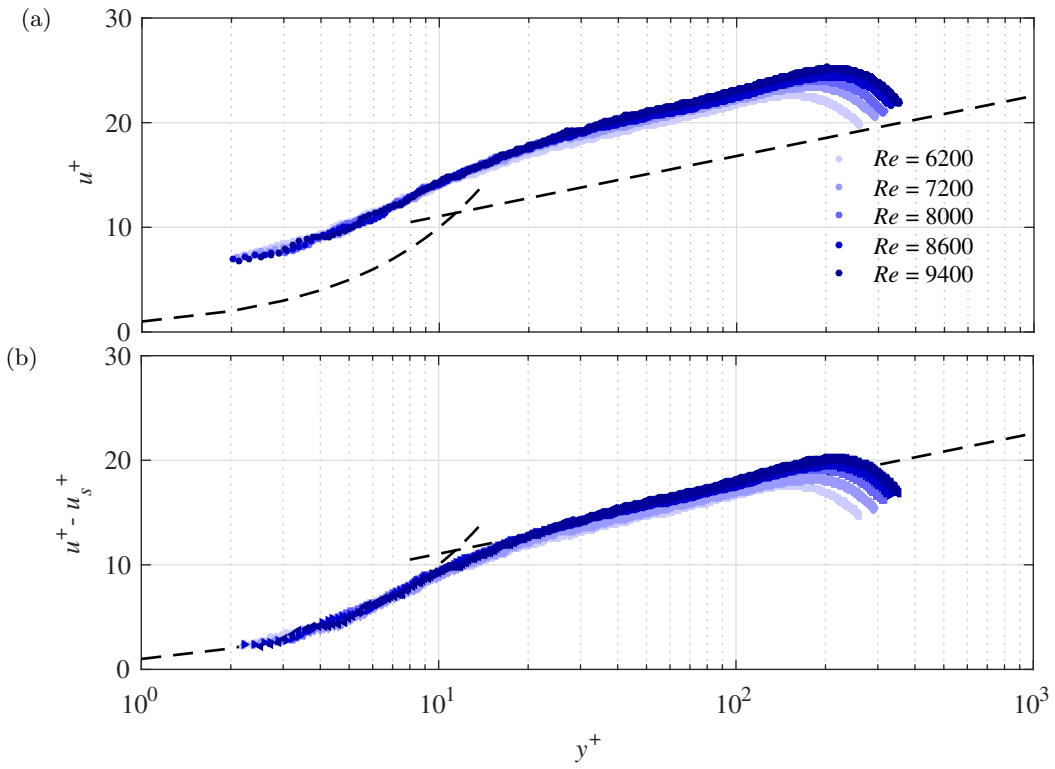

Figure 7.7: (a) Mean streamwise velocity profile over the SHS and (b) the profile of mean velocity with the slip velocity subtracted from it.

smaller than the peak of $\langle u^2 \rangle_b$ of the smooth surface. Away from the wall ($y/H > 0.06$), $\langle u^2 \rangle_b$ of the SHS is comparable with that over the smooth surface. This trend was also observed in the numerical simulations of Min and Kim (2004); Busse and Sandham (2012) and the experiments of Ling (2017); Abu Rowin and Ghaemi (2019a), when they normalized $\langle u^2 \rangle$ for both the SHS and the smooth surface using a common inner scaling of the smooth surface. The difference between $\langle u^2 \rangle$ for the smooth surface and for the SHS decreases with increasing Re close to the surface ($y = 0.05H$), as shown in Figure 7.8a. For instance, at $y \approx 0.01H$, $\langle u^2 \rangle$ over the SHS is larger than that over the smooth surface by $\sim 58\%$ at $Re = 6200$. However, at $Re = 9400$ (at the same wall-normal location), the difference between $\langle u^2 \rangle$ over the smooth and the SHS is reduced to $\sim 3\%$. The profiles of $\langle u^2 \rangle^+$ over the SHS in Figure 7.8b overlap with subtle inconsistencies at different Re. Regardless of Re, the profiles of $\langle u^2 \rangle^+$ over the SHS are larger than that of the smooth surface in the

near-wall region and they gradually approach $\langle u^2 \rangle^+$ of the smooth surface with increasing y^+. The numerical simulations of Rastegari and Akhavan (2015); Seo et al. (2018a) and the experiments of Ling (2017); Abu Rowin and Ghaemi (2019a) also observed a larger $\langle u^2 \rangle^+$ over the SHS near the wall, which gradually reduced and reached the smooth surface with an increase of wall-normal distance. The new observation here is the overlap of $\langle u^2 \rangle^+$ of the SHS for the investigated range of Re.

In Figure 7.8c, the SHS profiles of $\langle v^2 \rangle_b$ converge to zero at the wall, in a manner similar to the smooth surface. The profiles of $\langle v^2 \rangle_b$ of the SHS are smaller than the smooth surface away from the wall at $y > 0.09H$ and $y > 0.02H$ for the $Re = 6200$ and 9400, respectively. A similar trend is also seen in the DNS of Min and Kim (2004) over a flat surface with an imposed slip and the 2D-PTV measurement of Abu Rowin et al. (2017) over an SHS with low roughness of $k^+ = 0.11$. The experiment of Ling et al. (2016) reported a larger $\langle v^2 \rangle$ at the wall due to the large roughness for their tested surfaces. The increase of Re in Figure 7.8c results in a larger reduction of $\langle v^2 \rangle_b$ over the SHS relative to $\langle v^2 \rangle_b$ over the smooth surface. The simulation of Lee et al. (2015) showed that the difference between $\langle v^2 \rangle$ for the smooth and the SHS reduces with increasing Re, which agrees with the current investigation. The profiles of $\langle v^2 \rangle^+$ over the SHS in Figure 7.8d overlap for all Re cases and they are higher than those over the smooth surface throughout the measurement domain. The DNS of Rastegari and Akhavan (2015) and the experiment of Abu Rowin and Ghaemi (2019a) also reported a similar trend of larger $\langle v^2 \rangle^+$ over the SHS compared with $\langle v^2 \rangle^+$ over the smooth surface.

Compared with the smooth surface in the near wall in Figure 7.8e, the large $\langle w^2 \rangle_b$ over the SHS is similar to that observed for $\langle w^2 \rangle_b$, in Figure 7.8a. This increase of $\langle w^2 \rangle$ is due to the presence of the slip velocity in the $z-$direction (Min and Kim, 2004; Abu Rowin and Ghaemi, 2019a). Further away from the wall, at $y > 0.06H$, $\langle w^2 \rangle$ is smaller than $\langle w^2 \rangle$ of the smooth surface. The observed $\langle w^2 \rangle$ trend was seen previously in the numerical simulations of Min and Kim (2004); Busse and Sandham (2012), and the experiment of Abu Rowin and Ghaemi (2019a). The difference between $\langle w^2 \rangle$ for the SHS and for the smooth surface

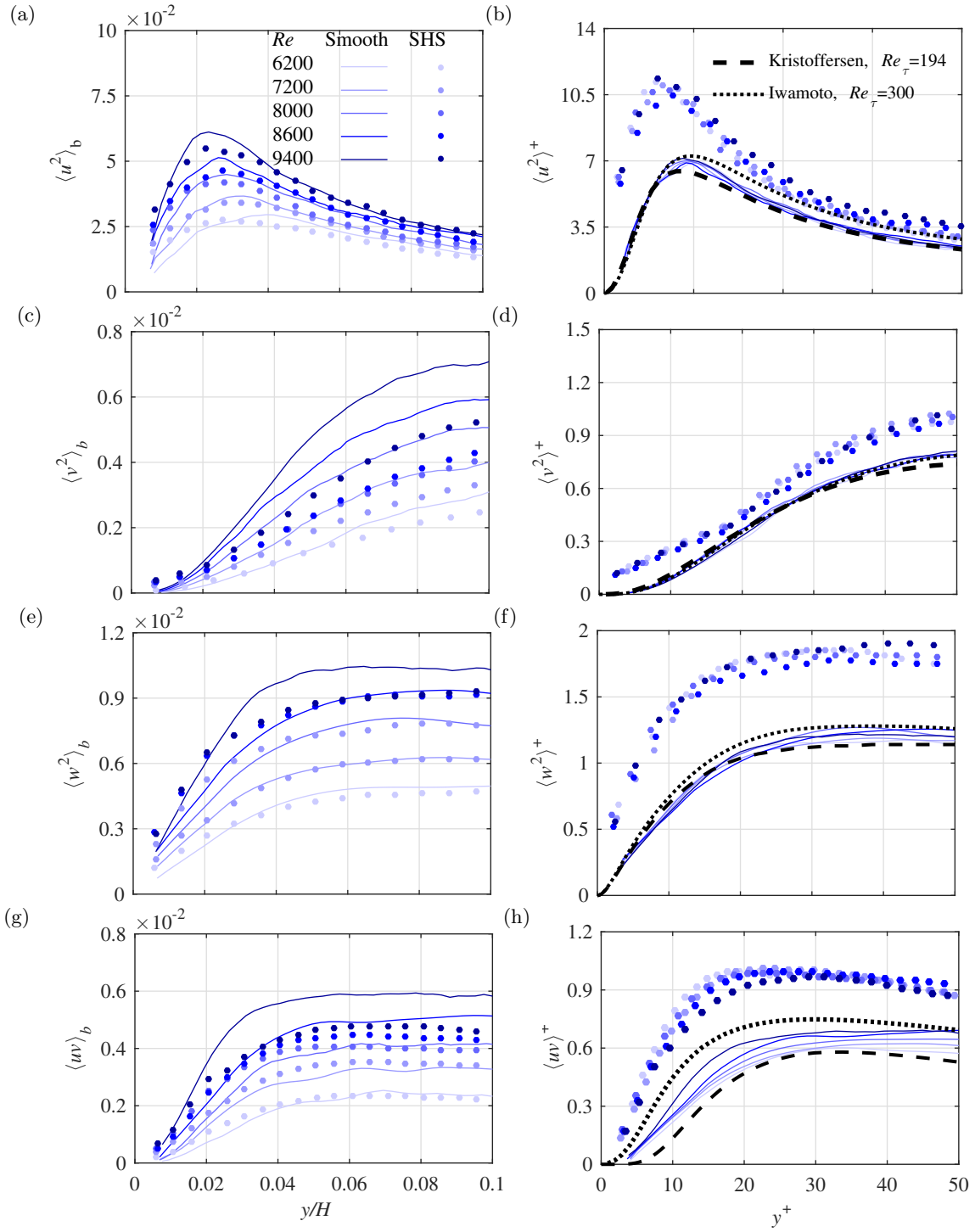

Figure 7.8: 3D-PTV measurement of $(a-b)$ streamwise, $(c-d)$ wall-normal, $(e-f)$ spanwise and $(g-h)$ shear Reynolds stresses over the smooth and SHS. The left side figures are normalized by U_b at the lowest Re and the channel height, while the right-side figure normalized by the inner scaling of the corresponding surface.

decreases with increasing Re close to the surface ($y < 0.02H$), as shown in Figure 7.8e. Figure 7.8e also shows that the increase of Re increases the difference between $\langle w^2 \rangle$ over the SHS and the smooth surface away from the wall. For instance, at $y = 0.09H$, $\langle w^2 \rangle$ over the SHS compared with that above the smooth surface is reduced from 5.6% to 15.3% for Re from 6200 to 9400, respectively. Similarly, the DNS of Lee et al. (2015) noted a significant reduction of $\langle w^2 \rangle$ peaks with respect to the corresponding smooth surface, which varied from 16% at $Re = 2800$ to 46% at $Re = 10975$. Profiles of $\langle w^2 \rangle^+$ over the SHS are larger than over the smooth surface at $y^+ < 50$. The DNS of Rastegari and Akhavan (2015) also noted a larger $\langle w^2 \rangle^+$ over the SHS compared with that over the smooth surface until $y^+ \approx 220$. The 3D-PTV measurement of Abu Rowin and Ghaemi (2019a) also showed a similar trend of larger $\langle w^2 \rangle^+$ over the SHS at $y^+ < 60$ compared with $\langle w^2 \rangle^+$ over the smooth surface when normalized by their own inner variables. The change in Re, as shown Figure 7.8f, has a negligible effect on $\langle w^2 \rangle^+$ over the SHS where all the profiles remain comparable.

At $y < 0.01H$ and for all Re cases, $\langle uv \rangle_b$ profiles over the SHS in Figure 7.8g are slightly larger than those above the smooth surface. At $y > 0.06H$, $\langle uv \rangle_b$ of the SHS is smaller than the smooth surface. Ling et al. (2017); Abu Rowin et al. (2017) have previously observed similar behavior. As reported previously by Abu Rowin et al. (2017) the increase of $\langle uv \rangle_b$ at the wall is a function of the surface roughness. The difference between $\langle uv \rangle_b$ for the smooth and the SHS increases with increasing Re. The DNS of Lee et al. (2015) also reported a weaker $\langle uv \rangle$ over the SHS compared with the smooth surface at larger Re.

The profiles of $\langle uv \rangle^+$ over the SHS are higher than the smooth surface everywhere in the measurement domain, see Figure 7.8h. The DHM of Ling et al. (2016) and the 3D-PTV of Abu Rowin and Ghaemi (2019a) also reported a larger $\langle uv \rangle^+$ over the SHS compared with $\langle uv \rangle^+$ over the smooth surface. The DNS of Rastegari and Akhavan (2015), however, reported smaller $\langle uv \rangle^+$ profile over the SHS compared with the smooth surfaces due to the flatness of the modelled SHS. The increase of Re has no effect on $\langle uv \rangle^+$ over the SHS where the profiles are comparable at different Re as shown in Figure 7.8h.

The maximum values of $\langle u_i u_j \rangle_b$ profiles for the SHS and the smooth surface are shown in

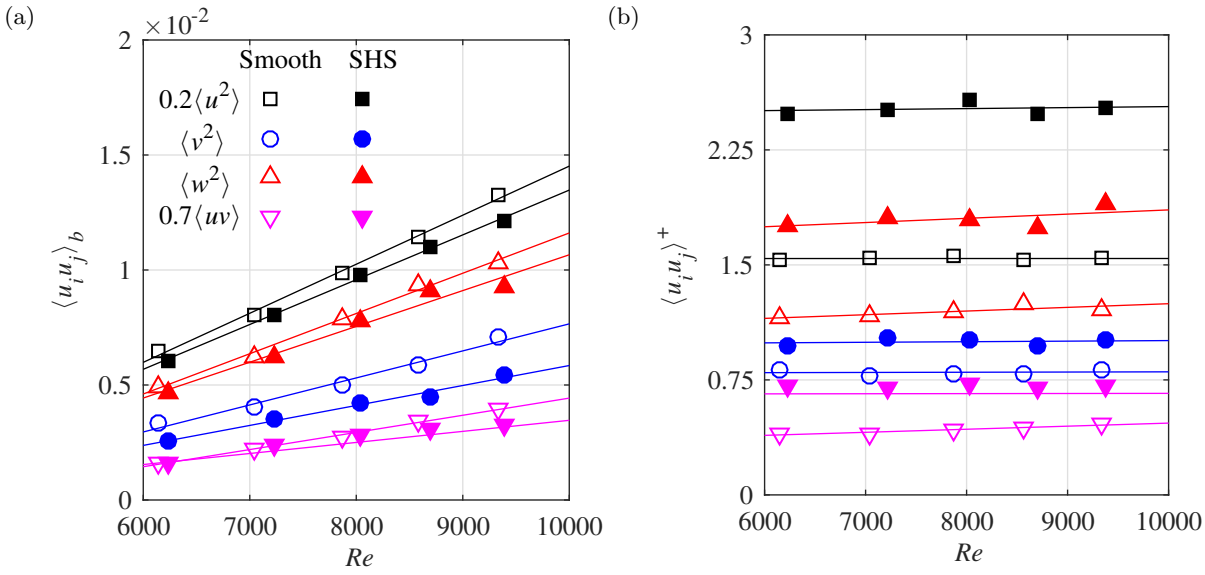

Figure 7.9: Maximum value of Reynolds stresses from 3D-PTV measurement over the smooth and the SHS obtained from Figure 7.8 non-dimensionalized by (a) U_b at the lowest Re and (b) the corresponding inner scaling. $\langle u^2\rangle$ and $\langle uv\rangle$ are normalized by 4.5 and 1.4, respectively, for clarity. The solid lines are fitted lines.

Figure 7.9a. As can be seen, $\langle u_i u_j\rangle_b$ of both surfaces increases linearly with increasing Re. However, the linear fit for the SHS has a smaller slope compared with the smooth surface, resulting in a widening gap between the smaller $\langle u_i u_j\rangle_b$ of SHS and the larger $\langle u_i u_j\rangle_b$ of the smooth surface with increasing Re. Therefore, at higher Re, the SHS has a larger effect on Reynolds stresses (in physical units). For further investigation of the change of Re on Reynolds stresses over the SHS, the peak values of $\langle u_i u_j\rangle^+$ are presented in Figure 7.9b. It is observed that all the peak values of normalized Reynolds stresses over the SHS are higher than those of the corresponding smooth surface.

To further scrutinize the effect of Re on Reynolds stresses over the SHS at the wall, the first reliable data point from the 3D-PTV at $y^+ \approx 4$ is plotted in Figure 7.10 for both U_b, and inner-scaling normalizations. As expected, $\langle u_i u_j\rangle_b$ over the smooth surface increased linearly with Re as shown in Figure 7.10a. Over the SHS, $\langle u_i u_j\rangle_b$ for all Reynolds stresses is larger than the smooth surface and follows a linear trend with increasing Re. In Figure 7.10b, $\langle u_i u_j\rangle^+$ remains relatively constant at different Re. For all Re cases, $\langle u_i u_j\rangle^+$ over the SHS is larger than the smooth surface.

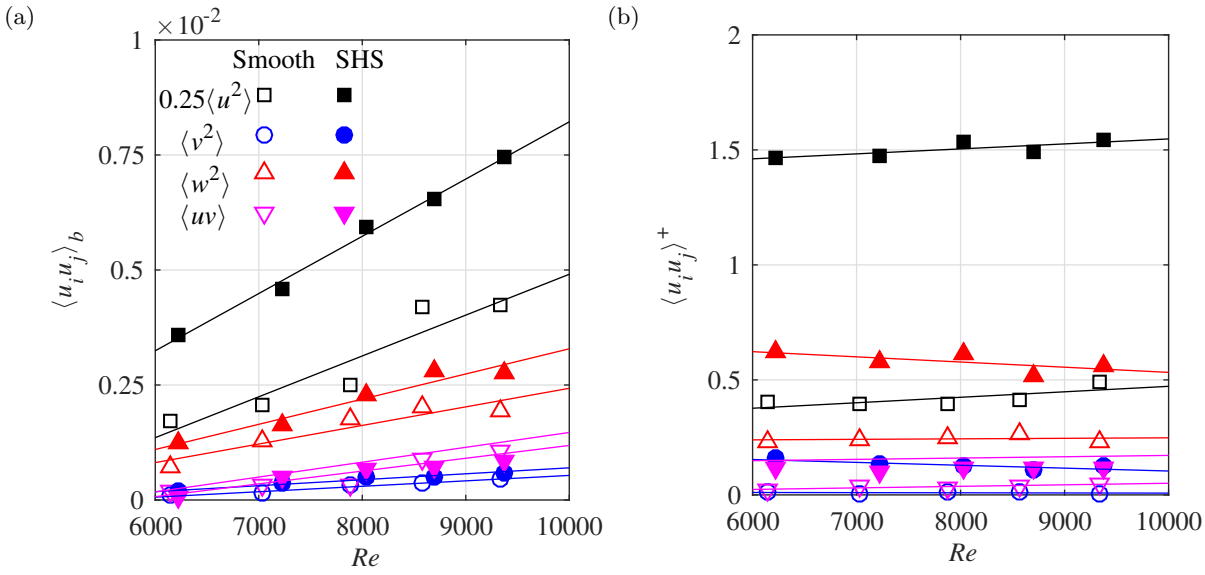

Figure 7.10: Reynolds stresses at $y^+ \approx 4$ from 3D-PTV measurement over the smooth and SHS (obtained from Figure 7.8) are non-dimensionalized by (*a*) U_b at the lowest Re and (*b*) the corresponding inner scaling. $\langle u^2\rangle$ is normalized by 4 for clarity. The solid lines are fitted lines.

7.3 Conclusion

An experimental investigation of the effect of the Reynolds number, Re, on the slip boundary condition and Reynolds stresses over a superhydrophobic surface (SHS) was carried out. The friction Reynolds number of the smooth surface varied from 200 to 283, based on the friction velocity and the half-channel height. The SHS had a random pattern generated by spray coating. The root-mean-square of surface roughness normalized by the wall-unit varied from 0.32 to 0.46. Two-dimensional particle tracking velocimetry (2D-PTV) was used to measure slip velocity, slip length, and the inner scaling of the turbulent flow over the SHS. Three-dimensional PTV (3D-PTV) was performed to investigate the effect of Re change on all Reynolds stress components of the SHS.

A non-zero velocity was detected at the SHS wall for all Re cases, which increased linearly from 0.25 to 0.34 m/s with increasing Re. The results also showed that the effective slip length of the SHS reduced from 97.5 to 69.6 μm with increasing Re. In contrast, it was found that the change of Re had a negligible effect on slip velocity and slip length, when

these parameters were normalized using inner scaling. The wall shear stress, estimated based on the velocity gradient at the wall, showed that the drag reduction of the SHS slightly increased from 38% to 42% with increasing Re.

When dimensional parameters in physical units are considered, the SHS increased the streamwise and spanwise Reynolds stresses in the immediate vicinity of the wall due to the slip velocity. In this region, the dimensional wall-normal and shear Reynolds stress of the SHS increased beyond that of the smooth surface, due to the surface roughness. However, farther away from the wall, dimensional Reynolds stresses were smaller than those of the smooth surface, indicating turbulence attenuation. With increasing Re, the effect of SHS on dimensional Reynolds stresses increased. However, when Reynolds stresses were normalized using friction velocity, all components of the Reynolds stresses for all Re overlapped. The overlapped profiles were also larger than the normalized Reynolds stresses of the smooth surface.

Chapter 8

Effect of surface roughness on slip boundary condition

The magnitude of the drag reduction (DR) obtained using superhydrophobic surfaces (SHSs) can be affected by several parameters such as Reynolds number, Re, (Gogte et al., 2005), hydrostatic pressure (Lei et al., 2009), and surface roughness (Bidkar et al., 2014). The previous experiments did not change the surface roughness to investigate the latter, but they varied the flow rate (i.e., Re) to alter the roughness in terms of wall units (Bidkar et al., 2014; Ling et al., 2016; Reholon and Ghaemi, 2018; Abu Rowin and Ghaemi, 2019b). The experiment of Bidkar et al. (2014) tested five different SHS topographies (i.e., surface geometries) in a water channel at a rage of Re varying from 1.0×10^6 to 9.0×10^6. They characterized the surfaces based on the root-mean-square of surface roughness normalized by the inner length scale of the turbulent flow, denoted by k^+. They estimated the DR from the difference of the load cell measurements of a no-slip surface and the SHS. They concluded that SHSs with $k^+ < 0.5$ reduce drag, while SHSs with larger k^+ increase drag. Ling et al. (2016) tested a wide range of SHSs roughness ($k^+ = 0.4 – 3.2$) and topographies at different Re (from 2.0×104 to 1.2×105). They estimated the DR from the change of the shear stresses between the no-slip smooth surface and the SHS. They observed that the increase of k^+ resulted in more rapid decay of the DR. Reholon and Ghaemi (2018) carried out DR measurement over an aft-section of an axisymmetric model coated with a superhydrophobic layer. They showed that the increase of k^+ from 0.40 to 0.97 (i.e., Re

from 5.0×10^5 to 1.2×10^6) diminished the DR from 23 to 1%, respectively. The recent 2D PTV measurement of Abu Rowin and Ghaemi (2019b) also varied Re over an SHS in a turbulent channel flow. Their measurement showed a slight increase of DR (from 34 to 40%) with increasing k^+ from 0.32 to 0.46 (or Re from 6.2×10^3 to 9.4×10^3). These investigations highlighted the potential correlation between the surface roughness and the DR over the SHSs. However, changing Re and the surface topography could also play a role in the change of DR over SHS (Gogte et al., 2005; Woolford et al., 2009b). Therefore, in the current study, different SHS roughness sizes for a similar surface topography are tested at a constant flow rate.

The direct numerical simulations (DNS) of Martell et al. (2009, 2010); Park et al. (2013) focused on the effect of the gas fraction or the microfeature spacing of an SHS on the DR. Martell et al. (2009) showed that increasing the texture spacing from 15 μm to 90 μm increases the DR from $\sim$ 12% to $\sim$ 30%, respectively. Martell et al. (2010) varied Re over an SHS with fixed texture spacing to alter the texture distance in terms of the wall unit. They reported a linear increase of the DR with increasing the microfeature spacing in wall units. Park et al. (2013) also showed that DR over the SHS increases with the texture spacing. The above-cited simulations assumed a flat air-liquid interface over the SHS without considering the interface stability. The DNS of Seo et al. (2015) investigated the effect of the pressure fluctuations on the stability of the air-liquid interface over an SHS with a range of texture sizes. They showed a predictable SHS performance (similar to a stable flat air-liquid interface) when the texture spacing is smaller than 10λ, λ here is the inner length scale of the turbulent flow. For larger texture spacing ($> 10\lambda$), the performance of the SHS differs from that with a stable flat air-liquid interface indicating an interface deformation. Experimentally, the stability of the air-liquid interface over the SHSs is more complex which is affected by the change of the air layer morphology due to the hydrostatic pressure over the surface (Lei et al., 2009), the solubility of air in water (Dilip et al., 2014), the water saturation level (Vajdi Hokmabad and Ghaemi, 2017), and surface topography (Seo et al., 2018a). Thus, experimental investigation of the effect of the

texture spacing on the air-liquid interface, which can be addressed by varying the surface roughness, is required.

The effect of k^+ on the slip boundary condition (slip velocity and slip length) over the SHSs is investigated numerically by (Martell et al., 2010; Park et al., 2013). The DNS of Martell et al. (2010) showed that the increase of the texture spanning results in larger slip velocity normalized by the friction velocity. The simulation of Park et al. (2013) also concluded that the increase of the gas fraction of an SHS increases the ratio of the slip velocity to the bulk velocity. This trend is expected for these simulations since they modeled the flow over the SHSs with alternating regions of slip and no-slip based on the texture spacing. The experiments of Ling et al. (2016); Reholon and Ghaemi (2018); Abu Rowin and Ghaemi (2019b) also investigated the impact of the change of k^+ on the slip boundary condition. Since these experiments increased k^+ by increasing Re, they reported a larger dimensional slip velocity at larger k^+. However, Reholon and Ghaemi (2018); Abu Rowin and Ghaemi (2019b) measured a smaller dimensional slip length at larger k^+. They associated this reduction with the depletion of the air layer at a larger Re. Proper investigation at a constant Re over SHSs with different surface roughness is required to understand the effect of k^+ on the slip boundary condition.

The current study investigates the effect of the SHS roughness on the slip boundary condition and DR by testing different surface roughness sizes with the same surface topography. The surfaces manufacturing procedure and characterization were introduced in Section 3.3.2. These surfaces are tested at a constant flow rate to avoid DR change due to Re. The channel is operated at Re = 8,400, based on the bulk velocity and full channel height. Time-resolved 3D-PTV based on the shake-the-box algorithm (Schanz et al., 2016), introduced in Section 4.3, is used for flow characterization. The measurements over the SHSs are compared with that over a no-slip smooth surface.

8.1 Results

All the experiments were carried out at a bulk velocity of $U_b = 1.37$ m/s. The Reynolds number at this bulk velocity is $Re = 8{,}400$, defined as $Re = U_b H/\nu$, with ν denoting the kinematic viscosity. The friction velocity over the no-slip surface is $u_{\tau 0} = 0.0775$ m/s and the wall unit $\lambda_0 = 12.7$ μm, which are evaluated by the slope of the measured velocity profile in the sublayer region within $2.5 < y^+ < 3.5$ and confirmed by Clauser's method (Clauser, 1956) as described in results section. The friction Reynolds number is $Re_\tau = 237$, defined as $Re_\tau = u_\tau H/2\nu$. A summary of the flow characterizations is listed in Table 8.1. In this investigation, the superscript + denotes parameters non-dimensionalized using wall-friction velocity, u_τ, and wall unit, λ, and the subscript 0 denotes parameters normalized using friction velocity, $u_{\tau 0}$, and wall unit, λ_0, of the no-slip smooth surface.

Parameter	Dimensions	Value
Channel dimensions ($H \times W \times L$)	mm	$6 \times 40 \times 1200$
U_b	m/s	1.37
Re	...	8400
$u_{\tau 0}$	m/s	0.0775
λ_0	μm	12.7
Re_τ	...	237

Table 8.1: Summary of the parameters of the turbulent channel flow with smooth wall.

In this section the effect of the SHS roughness on the mean velocity profile, turbulence intensities, and drag reduction will be considered. The test surfaces are placed on the top wall of the channel at $y = 0$ mm. Results of a no-slip smooth surface are also shown for reference. The mean velocity profiles and high-order turbulence statistics are obtained from a moving average of the individual particles' velocity over bins of 10 μm (0.79^+) and 60 μm (4.7^+) in the wall-normal (y) direction, respectively, with 75% overlap.

8.1.1 Mean velocity

The non-dimensionalized mean streamwise velocity profiles $u_0^+ = \langle U \rangle / u_{\tau 0}$ as a function of the wall-normal distance $y_0^+ = y/\lambda_0$ for the smooth and SHSs in the inner layer ($y^+ <$

80), appear in Figure 8.1a. Here $\langle\rangle$ denotes averaging in both time and space ($x-$ and $z-$directions). Over the smooth surface, u_0^+ follows the law-of-the-wall ($u^+ = y^+$) within $2.5 < y^+ < 3.5$ as shown in Figure 8.1a. Below this range ($y^+ < 2.5$), u_0^+ over the smooth surface diverges from the linear profile indicating the lower limit of the current measurement. Thus, the first reliable data point for this measurement system is at $y^+ = 2.5$. Over the three tested SHSs, u_0^+ is higher than that over the smooth surface for $y_0^+ < 20$. Further away from the wall, u_0^+ over the SHSs reduces below u_0^+ of the smooth surface to conserve the mass flow. This behavior of the velocity profile over the SHSs has been previously observed by the numerical investigations of Min and Kim (2004); Jelly et al. (2014), the theoretical work of Fukagata et al. (2006), and the experimental study of Abu Rowin et al. (2017).

Figure 8.1b shows a close-up view of the mean streamwise velocity profile normalized by the corresponding friction velocity, $u^+ = \langle U \rangle / u_\tau$, versus the wall-normal distance normalized by the corresponding wall unit, $y^+ = y/\lambda$. The extrapolation of the linear fit of the mean streamwise velocity over the smooth surface approaches a negligible magnitude (within measurement uncertainty) of $u^+ = 0.17$ (0.013 m/s) at the wall ($y^+ = 0$). The inner variables over the SHSs are also estimated from the velocity gradient within $2.5 < y^+ < 3.5$. The estimated friction velocity over the three SHSs, u_τ, is smaller than that for smooth surface. Over SHS-S, SHS-M, and SHS-L, u_τ is 0.067, 0.065, and 0.063 m/s, respectively. The extrapolation of the linear velocity fit over the SHSs shows a non-zero velocity at the wall confirming the existence of the slip velocity over the SHSs. The slip velocity, U_s, is 0.15, 0.25, and 0.27 m/s over SHS-S, SHS-M, and SHS-L, respectively. The ratio of U_s/U_b is increased by increasing the surface roughness. The normalized slip velocity by the corresponding friction velocity, $U_s^+ = U_s/u_\tau$, increased from 2.3 to 4.3 with increasing surface roughness. The effective slip length, l_s, is larger for larger roughness where $l_s = 33.9$ μm for SHS-S and $l_s = 66.8$ μm for SHS-L. This trend is also consistent with the normalized effective slip length, $l_s^+ = l_s/\lambda$, where l_s^+ increased with increasing the surfaces roughness. A summary of the flow parameters over the SHSs is shown in Table 8.2. The measurements

Surface	u_τ (m/s)	$\lambda(\mu m)$	Re_τ	k^+	U_s (m/s)	U_s/U_b	U_s^+	$l_s(\mu m)$	l_s^+
SHS-S	0.067	14.6	205	0.10	0.15	0.11	2.3	33.9	2.3
SHS-M	0.065	15.0	199	0.17	0.25	0.18	3.8	57.5	3.8
SHS-L	0.063	15.5	193	0.29	0.27	0.20	4.3	66.8	4.3

Table 8.2: Summary of the flow parameters over SHS-S, SHS-M, and SHS-L

of Ling et al. (2016) over SHSs with different topographies and roughness showed larger U_s over SHSs with larger k^+ agreeing with the current observation. However, it is worth noting that the measurements of Ling et al. (2016) were carried out at a range of Re varying from 2.0×10^4 to 1.2×10^5.

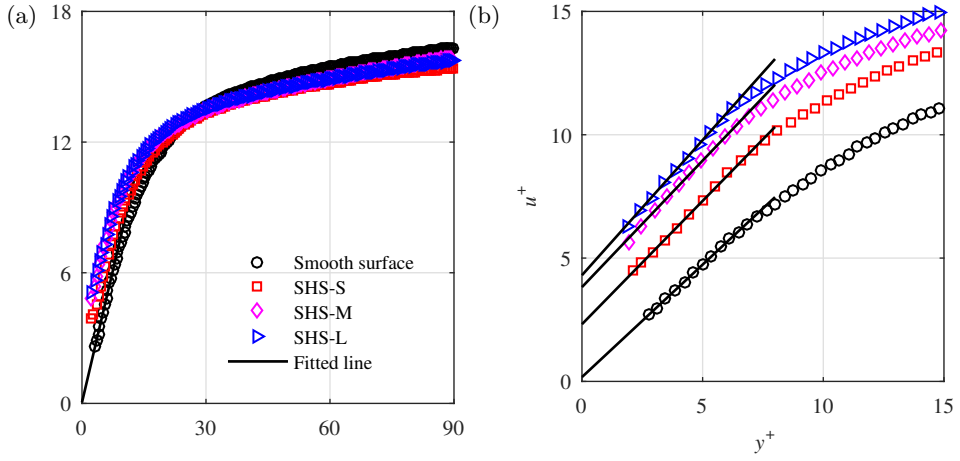

Figure 8.1: Mean streamwise velocity profiles over smooth and SHSs normalized by (a) the inner scaling of the smooth surface and (b) the corresponding inner scaling.

Semilogarithmic presentation of u_0^+ over the smooth and SHSs is plotted in Figure 8.2a. The linear sublayer is expressed as $u^+ = y^+$, while the log-law of the mean streamwise velocity is expressed as $u^+ = \frac{1}{\kappa} ln(y^+) + B$, where κ is the von Kármán constant and B is the intercept of the logarithmic profile. The inner scaling over the smooth surface here are estimated from Clauser's method (Clauser, 1956) by overlapping the u_0^+ with the log-law. The estimated friction velocity over the smooth surface from the Clauser's method is 0.074 m/s, which is $\sim 4.5\%$ smaller than that estimated from the velocity gradient. Over the smooth surface, u_0^+ agrees quite well with the linear sublayer and the log-law region

indicating fully developed channel flow. In contrast, u_0^+ over the SHSs is larger than the linear sublayer and smaller than the log-law. When u^+ over the SHSs are normalized with the corresponding inner scaling in Figure 8.2b, u^+ becomes larger than that over the smooth surface through out the measurement domain. The larger u^+ over the SHSs compared with the smooth surface has been numerically (Min and Kim, 2004; Türk et al., 2014; Jung et al., 2016; Seo et al., 2018a) and experimentally (Ling et al., 2016; Abu Rowin et al., 2017) proven as the direct effect of the slip velocity.

In Figure 8.2c, the normalized slip velocity is subtracted from the mean velocity ($u^+ - U_s^+$). The profiles over the SHSs approximately overlap with the smooth surface in the near wall. In the log layer, $u^+ - U_s^+$ over SHS-S is comparable with the smooth surface, while over SHS-M and SHS-L $u^+ - U_s^+$ are slightly smaller than the log law of the smooth surface. The DNS of Min and Kim (2004) observed an overlap of $u^+ - U_s^+$ over an SHS with the log law, when they imposed slip in the streamwise direction only. However, when they imposed slip lengths in the streamwise and spanwise directions, they reported a downward shift of $u^+ - U_s^+$ over an SHS compared with the log law of the smooth surface. This indicates streamwise and spanwise slip over SHS-M and SHS-L and negligible spanwise slip over SHS-S. The 3D-PTV measurement of Abu Rowin and Ghaemi (2019a) over an SHS with $k^+ = 0.35$ and $U_s = 0.27$ m/s reported an overlap of $(u^+ - U_s^+)$ of the smooth and SHS near the wall and slightly smaller $(u^+ - U_s^+)$ over the SHS with respect to the smooth surface away from the wall. This observation is consistent with that over SHS-M and SHS-L of the current study.

8.1.2 Reynolds stresses

Reynolds stresses over the smooth and SHSs in the inner layer ($y^+ < 50$) are shown in Figure 8.3. Reynolds stresses are normalized by the inner scaling of the smooth surface in Figure 8.3(a, c, e, g) and normalized by the inner scaling for each surface in Figure 8.3(b, d, f, h). Reynolds stresses from the DNS results of smooth channel flow at $Re_\tau = 195$ of Gilbert and Kleiser (1991) and at $Re_\tau = 300$ of Iwamoto et al. (2002) are included for comparison and

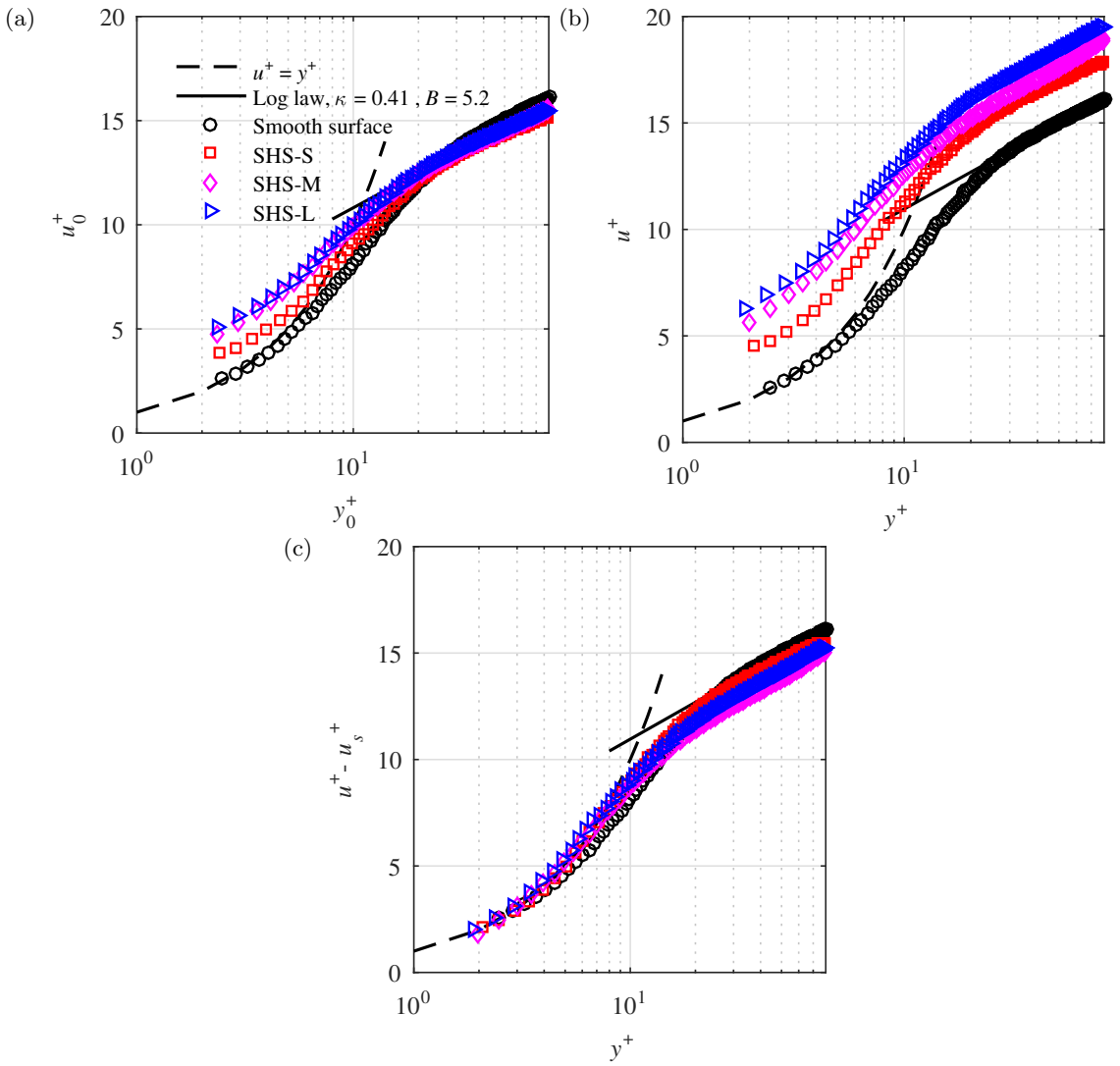

Figure 8.2: Mean streamwise velocity profiles over smooth and SHSs plotted using semi-logarithmic axes normalized by (a) the inner scaling of the smooth surface and (b) by the corresponding surface. (c) semi-logarithmic presentation of mean streamwise velocity subtracted by the normalized slip velocity.

uncertainty evaluation.

The streamwise component of Reynolds stress, $\langle u^2 \rangle_0^+$, over the smooth surface overlaps with the DNS profiles near the wall and falls within the two DNS profiles away from the wall in Figure 8.3a. Over the SHSs, $\langle u^2 \rangle_0^+$ is higher than the smooth surface for $y^+ < 8$ due to the slip velocity in the streamwise direction. For $y^+ > 8$, $\langle u^2 \rangle_0^+$ over the SHSs is smaller than the smooth surface. The peaks of $\langle u^2 \rangle_0^+$ over the SHSs are shifted toward the surface compared with that of the smooth surface. The effect of the SHSs on $\langle u^2 \rangle_0^+$ was seen before in the DNS of Min and Kim (2004) and Busse and Sandham (2012) and the experiments of Ling et al. (2016) and Abu Rowin and Ghaemi (2019a). In Figure 8.3a, the increase of the SHSs roughness results in larger $\langle u^2 \rangle_0^+$ near the wall with respect to the smooth surface, which is presumably due to the higher slip velocity at higher surface roughness as mentioned earlier. Larger attenuation of $\langle u^2 \rangle_0^+$ peaks is observed for larger surface roughness compared with the peaks of $\langle u^2 \rangle_0^+$ of the smooth surface. The peaks of $\langle u^2 \rangle_0^+$ reduced by 0.2, 3.1, and 10.8% over SHS-S, SHS-M, and SHS-L, respectively, compared to the smooth surface. For $y^+ > 20$, $\langle u^2 \rangle_0^+$ over SHS-S and SHS-M overlap and reach $\langle u^2 \rangle_0^+$ over the smooth surface at $y+ \approx 50$. Over SHS-L, $\langle u^2 \rangle_0^+$ remains smaller than $\langle u^2 \rangle_0^+$ of the smooth surface, SHS-S, and SHS-M for $y^+ > 8$. Figure 8.3b shows that $\langle u^2 \rangle^+$ over the SHSs are higher than the smooth surface for $y^+ < 20$. For $y^+ > 20$, $\langle u^2 \rangle^+$ over the SHSs approaches that over the smooth surface. This trend was observed in the simulations of Rastegari and Akhavan (2015); Seo et al. (2018a) and the experiments of Ling et al. (2016); Abu Rowin and Ghaemi (2019a). In the vicinity of the wall, larger $\langle u^2 \rangle^+$ is observed for larger roughness as shown in Figure 8.3b. Away from the wall ($y^+ > 20$), the change of the SHSs roughness has negligible effect on $\langle u^2 \rangle^+$ since all the profiles of $\langle u^2 \rangle^+$ overlap regardless of the surface roughness.

The wall-normal Reynolds stress, $\langle v^2 \rangle_0^+$, of the smooth surface overlaps with the DNS profiles, with subtle inconsistencies, as shown in Figure 8.3c. It can also be seen that $\langle v^2 \rangle_0^+$ over the SHSs overlaps with $\langle v^2 \rangle_0^+$ over the smooth surface for $y^+ < 20$. For $y^+ > 20$, $\langle v^2 \rangle_0^+$ over the SHSs is smaller than that of the smooth surface except for $\langle v^2 \rangle_0^+$ of SHS-S, which remains comparable to the smooth surface. The DNS of Min and Kim (2004) also reported

an overlap of $\langle v^2 \rangle_0^+$ over the smooth and an SHS with small l_s^+ ($l_s^+ = 0.35$) for $y^+ < 100$. However, for SHSs with larger $l_s^+ (> 1.61)$, they observed an overlap of $\langle v^2 \rangle_0^+$ over the smooth and SHS at $y^+ < 10$, and a smaller $\langle v^2 \rangle_0^+$ over the SHS compared with the smooth surface beyond this range. The 3D PTV measurement of Abu Rowin and Ghaemi (2019a) tested SHS with $k_0^+ = 0.35$ and $l_s^+ = 5.9$. They noticed a comparable $\langle v^2 \rangle_0^+$ over the smooth and SHS near the wall and smaller $\langle v^2 \rangle_0^+$ over the SHS compared with the smooth surface away from wall. This trend agrees with the current observation of $\langle v^2 \rangle_0^+$ over SHS-M and SHS-L. Figure 8.3c shows that the increase of the SHSs roughness has no effect on $\langle v^2 \rangle_0^+$ near the wall. Away from the wall stronger attenuation of $\langle v^2 \rangle_0^+$ is seen for surfaces with larger roughness. In Figure 8.3d, $\langle v^2 \rangle^+$ over the SHSs overlaps with $\langle v^2 \rangle^+$ of the smooth surface for $y^+ < 6$. Further away from the wall, regardless of the SHSs roughness, $\langle v^2 \rangle^+$ of the SHSs is larger than $\langle v^2 \rangle^+$ of the smooth surface. The DNS of Rastegari and Akhavan (2015) and the experiment of Abu Rowin and Ghaemi (2019a) also reported the same trend. The profiles of $\langle v^2 \rangle^+$ over the three tested SHSs overlap, see Figure 8.3d, indicating a negligible effect of the change of the SHSs roughness on $\langle v^2 \rangle^+$.

The spanwise component of Reynolds stress, $\langle w^2 \rangle_0^+$, over the smooth surface converges to zero at the wall and falls between the DNS profiles away from the wall in Figure 8.3e. Over the SHSs, $\langle w^2 \rangle_0^+$ follows a similar trend of $\langle u^2 \rangle_0^+$ in n Figure 8.3a, where $\langle w^2 \rangle_0^+$ over the SHSs is larger than $\langle w^2 \rangle_0^+$ of the smooth surface near the wall and smaller than $\langle w^2 \rangle_0^+$ of the smooth surface away from the wall. The DNS of Min and Kim (2004) and the experiment of Abu Rowin and Ghaemi (2019a) observed a similar trend. They related the increase of $\langle w^2 \rangle_0^+$ at the wall to the slip velocity in the spanwise direction. The surface roughness in Figure 8.3e appears to have the same effect in the streamwise direction, where larger surface roughness results in larger $\langle w^2 \rangle_0^+$ near the wall and smaller $\langle w^2 \rangle_0^+$ away from the wall. Figure 8.3f shows that $\langle w^2 \rangle^+$ over the SHSs is larger than that of the smooth surface across the measurement domain. A similar effect of the SHS on $\langle w^2 \rangle^+$ was observed by the simulations of Rastegari and Akhavan (2015); Seo et al. (2018a) and the experiments of Abu Rowin and Ghaemi (2019a,b). In the vicinity of the wall in Figure 8.3f, $\langle w^2 \rangle^+$ over the

SHSs increased gradually with increasing surface roughness. Away from the wall, however, all profiles of $\langle w^2 \rangle^+$ over the SHSs overlap regardless of the surface roughness.

The Reynolds shear stresses, $\langle uv \rangle_0^+$, over the smooth and SHSs are shown in Figure 8.3g. As expected, $\langle uv \rangle_0^+$ of the smooth surface falls between the profiles of the DNS, since Re_τ of the current measurement falls between Re_τ of Gilbert and Kleiser (1991) and Iwamoto et al. (2002) . Near the wall in Figure 8.3g, the profiles of $\langle uv \rangle_0^+$ over SHS-S and SH-M nearly overlap with that of the smooth surface, while $\langle uv \rangle_0^+$ over SHS-L is slightly higher than the smooth surface. This trend is expected since the increase of $\langle uv \rangle_0^+$ near the wall is linearly correlated with the increase of the surface roughness, as previously discussed by Abu Rowin et al. (2017). Away from the wall, the profiles of $\langle uv \rangle_0^+$ over the three SHSs are smaller than the $\langle uv \rangle_0^+$ profile of the smooth surface. In agreement with current observation, the experiments of Woolford et al. (2009a); Ling et al. (2016) reported an increase of $\langle uv \rangle_0^+$ in the immediate vicinity of the wall and a reduction of $\langle uv \rangle_0^+$ farther away from the wall when compared with $\langle uv \rangle_0^+$ of the smooth surface. The peaks of $\langle uv \rangle_0^+$ over the SHSs in Figure 8.3g are reduced with increasing the surface roughness. In Figure 8.3h, the profile of $\langle uv \rangle^+$ over SHS-S is comparable with the smooth surface near the wall and is larger than the smooth surface away from the wall. The profiles of $\langle uv \rangle^+$ of SHS-M and SHS-L are larger than $\langle uv \rangle^+$ of the smooth surface everywhere in the measurement domain. The DNS of Rastegari and Akhavan (2015) showed an overlap of $\langle uv \rangle^+$ of the smooth and SHS across the simulation domain ($y^+ < 220$) for SHS with DR $< 23\%$. For SHSs with larger DR ($> 32\%$), they reported a comparable $\langle uv \rangle^+$ of the smooth and SHS near the wall and smaller $\langle uv \rangle^+$ of the SHS away from the wall. The overlap of $\langle uv \rangle^+$ over the SHS in their simulation is presumably due to the flat surface assumption of the modeled SHSs. The increase of the surface roughness in Figure 8.3h results in larger $\langle uv \rangle^+$ for $y^+ < 20$. Further away from the surface, the change of the SHSs roughness has no effect since $\langle uv \rangle^+$ profiles over the three tested SHSs overlap.

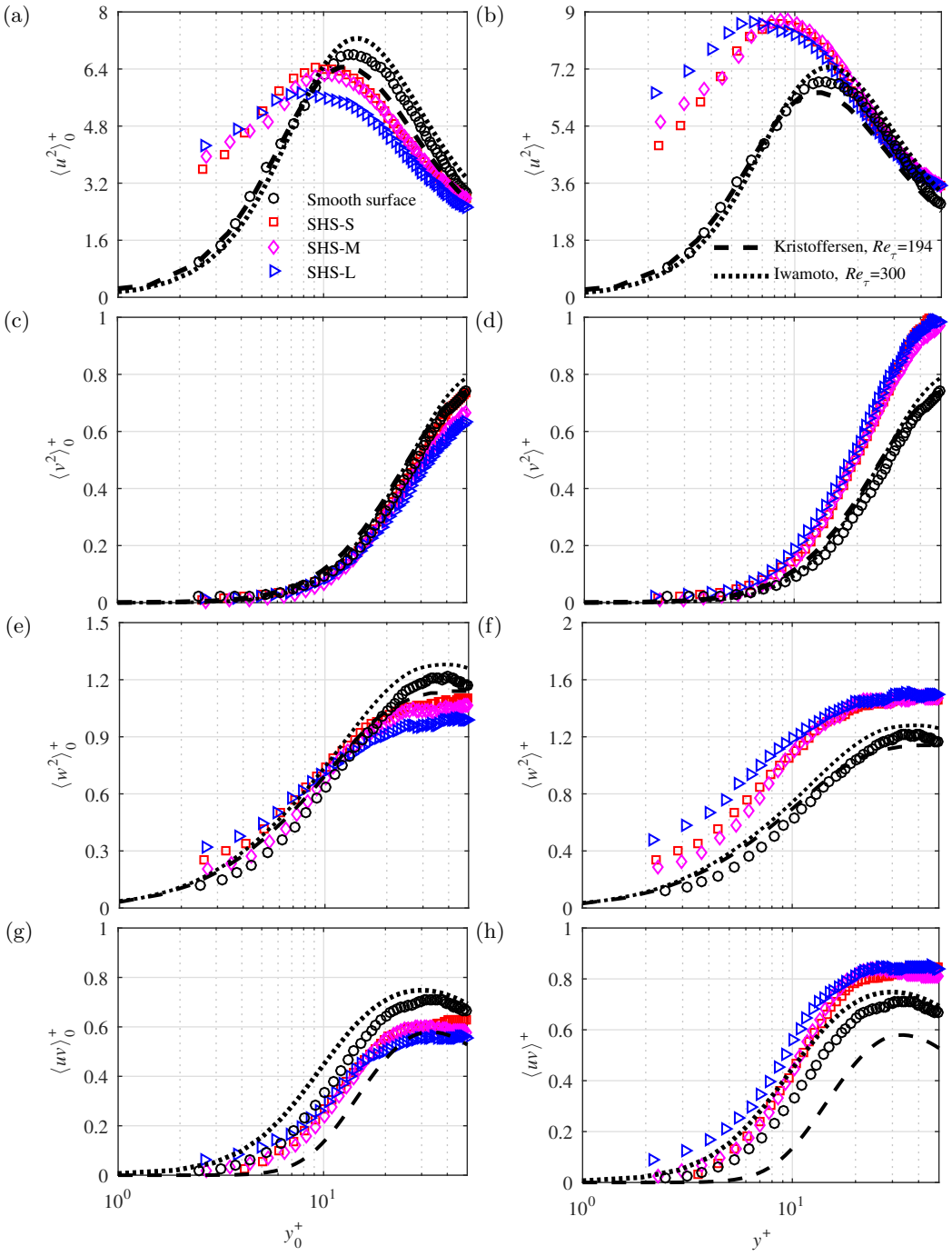

Figure 8.3: 3D-PTV measurement of $(a-b)$ streamwise, $(c-d)$ wall-normal, $(e-f)$ spanwise and $(g-h)$ shear Reynolds stresses over the smooth and SHSs. The left side figures are normalized by inner scaling of the smooth surface, while the right-side figure normalized by the inner scaling of the corresponding surface.

8.1.3 Drag reduction

The drag reaction (DR) over the SHSs is estimated from the difference between the wall shear stress of the smooth surface, $\tau_{w0} = \rho u_{\tau 0}^2$, and the SHS, $\tau_w = \rho u_\tau^2$, as DR $= (\tau_{w0} - \tau_w)/\tau_{w0}$. The DR percentages as a function of k^+ are shown in Figure 8.4. The DR over the SHSs increased linearly with increasing the SHSs roughness as DR $= 44.4k^+ + 21$. The DR over SHS-S, SHS-M, and SHS-L is 25.5, 28.6, and 33.9%, respectively. The DR is also estimated from the analytical expression of Rastegari and Akhavan (2015) for comparison. The expression states that DR over the SHS is a combination of the contribution of the slip velocity at the wall, DR_L, and the modification of the Reynolds shear stress, DR_T, as following

$$DR = DR_L + DR_T = \frac{U_s}{U_b} + \left(1 - \frac{U_s}{U_b}\right)\left(\frac{3\varepsilon}{1 - 3I^+}\right). \tag{8.1}$$

Here $\varepsilon = I_0^+ - I^+$ is the weighted integral difference of $\langle uv \rangle^+$ of the smooth and SHS estimated from

$$I^+ = \int_0^1 (1 - \delta)\langle uv \rangle^+ d\delta, \tag{8.2}$$

where δ is the normalized wall-normal coordinate, $\delta = 2y/H$. The integration in Equation 8.2 is carried out within the limits of the current 3D-PTV measurement ($2.5 < y^+ < 90$). The estimated DR from Equation 8.1 over SHS-S, SHS-M, and SHS-L is 24, 30, and 32%, respectively. As can be noticed, the DR from Equation 8.1 increases with increasing SHS roughness, similar to trend of that estimated from the shear stress difference. However, Equation 8.1 underestimates the DR by $\sim 2\%$ compared with the other method. The load cell measurement of the skin friction by Bidkar et al. (2014) over SHSs coated with Teflon and fluorosilane at $Re = 1 \times 10^6$ and 9×10^6 are also included in Figure 8.4. At $Re = 1 \times 10^6$, DR over the SHSs with Teflon coating diminished from 29% for $k^+ = 0.06$ to 15% for $k^+ = 0.35$. However, DR over SHSs with fluorosilane coating improved from 22% for $k^+ = 0.06$ to 47% for $k^+ = 0.84$. They associated the different trends of DR to the different coating without detailed specification. At $Re = 9 \times 10^6$, DR over SHSs with Teflon coating decayed with increasing surface roughness. Similarly, the drag over SHSs with fluorosilane coating

reduced by 7.7% at $k^+ = 0.45$ and increased 40% at $k^+ = 5.83$. The DHM measurement of Ling et al. (2016) is also included in Figure 8.4 for porous and non-porous SHSs. Unlike the current observation, Ling et al. (2016) reported a smaller DR with increasing the surface roughness for the porous and non-porous SHSs.

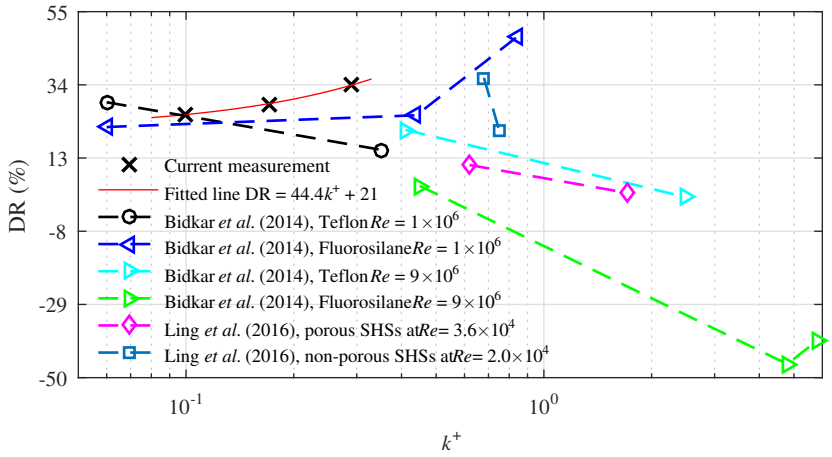

Figure 8.4: Drag reduction as a function of the surface roughness of the current measurement. Results of Bidkar et al. (2014) and Ling et al. (2016) are also included for comparison. Drag reduction measurements of Reholon and Ghaemi (2018); Abu Rowin and Ghaemi (2019b) are not included here since both varied Re to change k^+.

8.2 Conclusion

The effect of the SHS roughness on the slip boundary condition, Reynolds stresses, and drag reduction are investigated in this study. For this purpose, three SHSs with different roughness sizes and the same topography are used. The three surfaces have a random pattern with an average root-mean-square height of 1.44, 2.58, and 4.5 μm denoted as SHS-S, SHS-M, and SHS-L, respectively. The three-dimensional particle tracking velocimetry (3D-PTV) measurement of the mean velocity showed that the slip velocity over the SHSs increased with increasing the surface roughness. The normalized slip velocity by the corresponding inner scaling also increased with the surface roughness. This observation contradicts the observation of Abu Rowin and Ghaemi (2019b). They reported a constant normalized slip velocity with increasing the surface roughness, when they varied the surface roughness in

terms of wall units by varying the flow rate. It was also noted in the current measurement that the increase of the surface roughness increases the dimensional effective slip length. This trend also does not agree with experiments that increased the normalized surface roughness by increasing Re (Ling et al., 2016; Reholon and Ghaemi, 2018; Abu Rowin and Ghaemi, 2019b). These studies reported a smaller dimensional slip velocity for larger surface roughness due to the depletion of the air plastron at a higher Re.

The effect of the SHS roughness on all components of Reynolds stresses is also investigated in this study. The streamwise and spanwise Reynolds stresses over the SHS, normalized by the inner scaling of the smooth surface, were higher than that over the smooth surface near the wall. This increase is associated with the slip velocity in the streamwise and spanwise directions (Min and Kim, 2004; Abu Rowin and Ghaemi, 2019a). The magnitude of the streamwise and spanwise Reynolds stresses at the wall over the SHS increased with increasing surface roughness. The wall-normal Reynolds stress, normalized by inner scaling of the smooth surface, over the SHS was comparable with that over the smooth surface near the wall regardless of the surface roughness. Further away from the wall, the streamwise, spanwise, and wall-normal Reynolds stresses, normalized by smooth inner scaling, were smaller than that over the smooth surface. The larger surface roughness results in a smaller Reynolds stress component away from the wall. When the streamwise, spanwise, and wall-normal Reynolds stresses were normalized by the inner scaling of each case, the streamwise Reynolds stress over the SHS was larger than that over smooth surface near the wall, and approached the smooth surface away from the wall. The spanwise Reynolds stress over the SHS was higher than the smooth across the measurement domain. The wall-normal Reynolds stress over the SHS was similar to that over the smooth surface near the wall and larger further away from the wall. The increase of the surface roughness only affected the streamwise and spanwise Reynolds stresses near the wall, where larger roughness resulted in larger streamwise and spanwise Reynolds stress magnitude. The change of the surface roughness has a negligible impact of the wall-normal Reynolds stress across the measurement domain since all the profile overlapped.

Reynolds shear stresses over the three tested SHSs is also investigated in this work. Reynolds shear stress at $y \approx 2.5\lambda$ normalized by the inner scaling of the smooth surface and each surface are shown in Figure 8.5a and 8.5b, respectively. Data from the digital holographic microscopy of Ling et al. (2016) for SHSs with $k^+ = 0.43$, 0.62, 1.71, and 3.28 at $y \approx 2.5\lambda$ are also included in Figure 8.5. Here k^+ is the surface roughness normalized by the inner length scale. As shown, Reynolds shear stress over the SHS increases with increasing surface roughness in the vicinity of the wall. The experiment of Abu Rowin and Ghaemi (2019a) observed that the different between Reynolds shear stress over the SHS and the corresponding smooth surface increases linearly with increasing surface roughness. Unlike these observations, the simulations of Martell et al. (2009, 2010); Rastegari and Akhavan (2015) reported a zero Reynolds shear stress over the SHS at the wall due to the flat surface assumption. The simulation of Alamé and Mahesh (2019) modelled a rough SHS obtained from sand- blasted surface. They carried the simulation over three air-layer heights of 0, 1.6, and 6.5λ. They observed a zero Reynolds shear stress at the wall when the air-layer height is 0 and 1.6λ and a non-zero Reynolds shear stress for SHS with 6.5λ air-layer height.

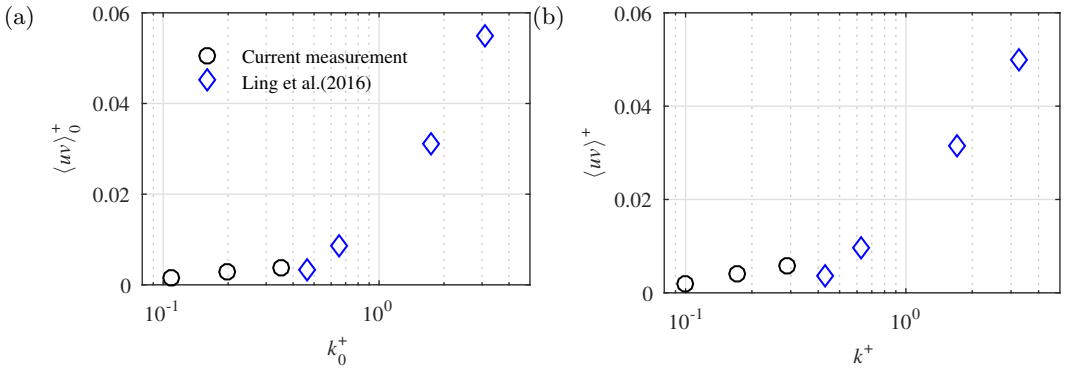

Figure 8.5: Reynolds shear stress in the vicinity of the wall normalized by the inner scaling of (a) smooth surface and (b) each surface.

To advance understanding the effect of the SHSs roughness on the DR, the ratio of DR_T to DR_L is shown in Figure 8.6. As can be seen, DR_T/DR_L over SHS-S, SHS-M, and SHS-L is 1.21, 0.68, and 0.60, respectively. This trend indicates that the increase of the

surface roughness has more effect on DR due to the slip velocity than on the modification of Reynolds shear stress.

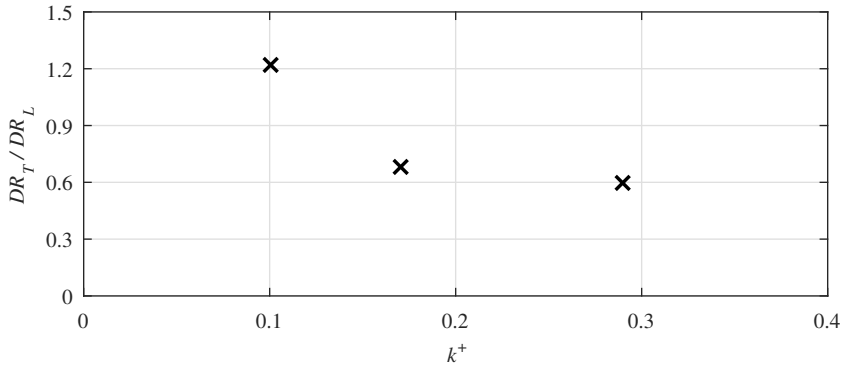

Figure 8.6: The ratio of the DR due to the slip velocity at the wall to DR due to the modification of Reynolds shear stress plotted as a function of the surface roughness.

Chapter 9

Conclusions and recommendations

Reduction of skin-friction using a thin layer of air between liquid flow and a solid surface has been a topic of active research in the last decade. The bio-inspired superhydrophobic surface (SHS) is one of the ways to enhance this air layer. The mechanism of skin-friction reduction over an SHS has been investigated experimentally in this thesis. This thesis also scrutinizes the parameters that can limit the skin-friction reduction of an SHS. This chapter presents the conclusion derived from the findings of this thesis. Additionally, this chapter offers recommendations and guidance to conduct further research related to a similar field.

9.1 Conclusion

First, the magnitude of streamwise slip velocity and its effect on the mean velocity profile were investigated using simultaneous long-range microscopic particle tracking velocimetry (micro-PTV) and macroscopic particle image velocimetry (PIV). For this investigation, the tested SHS had a random texture with a root-mean-square roughness of 10.2 μm (0.11λ), here λ was the viscous length scale. The micro-PTV results showed a slip velocity of 0.023 m/s over the SHS (13% of the bulk velocity) at a friction Reynolds number of $Re_\tau = 140$ which corresponds to a 200 μm effective slip length. Away from the wall, the mean velocity of the SHS was smaller than that of a no-slip surface at the same flow rate. The drag was reduced by 19% based on the slope of the linear viscous sublayer and 22% based on the analytical expression of Rastegari and Akhavan (2015).

A three-dimensional Lagrangian PTV (3D-PTV) based on the shake-the-box (STB) method was used for measurement of the slip velocity in the spanwise direction and to study the effect of the SHS on all components of the Reynolds stresses. For this measurement, a randomly textured SHS was generated using spray coating with a root-mean-square roughness of $4.9\,\mu$m (0.29λ). The 3D-PTV measurements confirmed an isotropic slip with a streamwise effective slip length of 5.9λ and a spanwise effective slip length of 5.9λ. As a result, both the near-wall mean streamwise and spanwise velocity profiles over the SHS were higher than the smooth surface. The streamwise and spanwise slip velocities over the SHS were $0.27\,$m/s and $0.018\,$m/s, respectively. Farther away from the SHS, the effect of the slip velocity diminished and smaller streamwise and spanwise velocities were observed compared with the smooth surface. When dimensional Reynolds stresses over the smooth surface and SHS were compared at the same flow rate, the streamwise and spanwise Reynolds stresses were larger in the near-wall region of the SHS. This indicates the presence of both streamwise and spanwise slip. The peaks of the streamwise and spanwise Reynolds stresses, when normalized by the smooth and the corresponding inner scaling, were also shifted closer to the wall due to the thinner inner layer over the SHS. The wall-normal Reynolds stress over the SHS remained comparable to the smooth surface in the near-wall region due to the non-permeable boundary condition of both surfaces. In the immediate vicinity of the wall, the Reynolds shear stress over the SHS was slightly larger than that of the smooth surface. All components of the Reynolds stress tensor were smaller over the SHS farther away from the surface. However, when the Reynolds stresses were non-dimensionalized using the corresponding inner scaling of each surface, they had a larger value with respect to the smooth surface across the inner layer. This indicates that normalization of Reynolds stresses using inner scaling does not result in overlap of the Reynolds stress profiles when slip velocity is present.

The patterns of the shear-free regions were also investigated over the SHS using contours of near-wall mean streamwise velocity in a streamwise/spanwise plane at $y = 3\lambda$. The results showed streamwise-elongated patches of high streamwise velocity over the SHS,

which represent the morphology of the air layer underneath. The high-speed regions were up to $800\lambda \times 300\lambda$ (13.6 mm $\times$ 5.1 mm) in the streamwise and spanwise directions, respectively. The scanning electron microscopy images and the profilometer measurements also showed that the largest roughness features with $\sim$ 20 mm height occur at a mean distance of approximately 12 mm, similar to the streamwise length of the largest shear-free regions. Therefore the smaller roughness peaks do not disrupt the shear-free regions as the plastron is pinned between the highest peaks. The drag reduction (DR) over the current SHS was estimated and evaluated using various techniques. The results indicated a DR of approximately 30% – 38% over the investigated SHS.

Previous experiments in turbulent flows have demonstrated a large variation in SHS drag with respect to a reference no-slip smooth surface. The variation in drag has been associated with the superhydrophobicity of the surface, the relative size of the surface asperities with respect to the length scale of the turbulent flow, and water solubility. The effect of the change of Reynolds number (Re) on the DR over the SHSs remains poorly understood. Two possible trends have been observed. The first is the DR over the SHSs degrades with increasing Re. The second is DR over the SHS improves with increasing Re. Thus, in this thesis the effect of Re on the slip boundary condition and the Reynolds stresses over an SHS in a turbulent channel flow were experimentally investigated. The Re was varied from 6,000 to 10,000, based on full channel height, which is equivalent to $Re_\tau = 200$ to 280, based on friction velocity and half-channel height. The SHS had a random pattern generated by spray coating, with root-mean-square of wall roughness which varied from 0.32λ to 0.46λ. Flow statistics above a no-slip smooth surface were included for comparison. Two-dimensional PTV (2D-PTV) was employed to measure the slip velocity and length over the SHS due to the use of small tracers in this measurement. The increase of Re over the SHS raised the slip velocity linearly from 0.25 to 0.34 m/s. In contrast, it was found that the change of Re has a negligible effect on the slip velocity, normalized by the corresponding inner scaling. The results also showed that the effective slip length over the SHS reduced from 97.5 to 69.6 μm with increasing of Re. The latter was associated with the increase of the hydrostatic

pressure inside the test section, which enhanced the solubility of air in water, reducing the plastron thickness. The non-dimensionalized effective slip length by the corresponding inner scaling remained constant, regardless of Re. The wall shear stress, based on the velocity gradient, showed that the drag reduction of the SHS increased from 38 to 42% with increasing Re.

Three-dimensional PTV (3D-PTV) was also performed to provide detailed results about the effect of the change of Re on all components of Reynolds stresses over the SHS. In the near-wall region, the increase of Re reduced the differences between the dimensional streamwise Reynolds stress over the smooth and SHS. A similar observation was seen for the dimensional spanwise Reynolds stress. Away from the wall, the increase of Re increased the differences between each component of the dimensional Reynolds stresses over the smooth and the SHS. The maximum values of all components of the dimensional Reynolds stresses over the SHS were smaller than those over the smooth surface and increased linearly with increasing Re. When Reynolds stresses were normalized by the inner scaling of each case, the results showed that Reynolds stresses over the SHS were larger than those of the smooth surface. The change of Re did not affect the normalized Reynolds stresses over the SHS where the normalized profiles at different Re overlapped.

The DR over the SHSs was also affected by the surface roughness. All the previous studies have investigated this point by varying the flow rate (i.e., Re) to change the surface roughness in terms of the wall unit. In this thesis, the surface roughness of SHSs was varied and tested at a constant Re. The tested SHSs were fabricated by a sandblasting process with varying the particles sizes and sandblasting speed. The average root-mean-square height of the SHSs roughness were 1.44, 2.58, 4.5 μm. These surfaces are denoted as SHS-S, SHS-M, and SHS-L for small, medium, and large surface roughness, respectively. The surfaces were tested in a turbulent channel flow operated at $Re = 8{,}400$, based on the bulk velocity and full channel height. The flow over these surfaces was characterized using 3D-PTV. The results showed that the surface roughness increased the slip velocity. The slip velocity was 0.15, 0.25, and 0.27 m/s over SHS-S, SHS-M, and SHS-L. The effective slip length normalized

by the friction velocity of each case increased with increasing the surface roughness. The dimensional effective slip length also increased with the surface roughness as 33.9, 57.5, and 66.8 μm for SHS-S, SHS-M, and SHS-L, respectively. This increase of the effective slip length indicates the higher air layer thickness for higher roughness. The consistent increase of the effective slip length magnitude also indicates the stability of the air plastron with changing surface roughness. This observation is a unique feature of the current study since the previous experiments of Reholon and Ghaemi (2018) and Abu Rowin and Ghaemi (2019b) reported a smaller effective slip length with increasing the surface roughness owing to the depletion of the air-layer. The effect of the SHS on Reynolds stresses intensified with the surface roughness. The DR, estimated from the change of the wall shear stress of the no-slip and SHSs, increased linearly with the surface roughness. The increase of surface roughness resulted in larger contribution of the slip velocity in reducing drag than the modification of Reynolds shear stress.

9.2 Recommendations

The current thesis advanced the understanding of DR over SHS and the parameters that could affect the DR over the SHS. The development of the SHS lacks several key features as given below.

Relation between the surface pattern and the slip velocity

In this thesis, SHSs with random texture were only used due to manufacturing simplicity and scalability. The organized pattern SHSs can provide larger DR and slip velocity compared with the random textures SHSs (Seo and Mani, 2018b). The exact advantages of the SHS structure (surface morphology) on the surface performance, and on the slip boundary conditions are still unclear. The experiment of Woolford et al. (2009a) tested two SHSs with ribs oriented longitudinally and transversely to the flow in a turbulent channel flow. They performed a pressure drop measurement over the test surfaces for DR analysis. Their results showed that the SHS with longitudinal patterns reduces the skin friction while SHS with

transverse pattern yielded to an increase of the skin friction. Without direct measurement of the slip velocity, Woolford et al. (2009a) attributed the DR over the streamwise ribs to the high streamwise slip velocity, while the increase in drag over the spanwise ribs to the predominant spanwise slip velocity. Measurement of slip velocity in the streamwise and spanwise directions for organized pattern SHSs is necessary to confirm this trend.

Isotropic slip length over large roughness SHSs

In this thesis, a homogeneous isotropic slip over a low roughness SHS is observed. However, the simulation of Seo and Mani (2016) reported an inhomogeneous slip length (streamwise effective slip length is not equal to the spanwise effective slip length) over randomly textured SHSs with large roughness. It is recommended to carry out measurement over large roughness randomly texture SHSs to scrutinize the relationship between the surface roughness and the slip length.

Air-layer stability as a function of the surface roughness

The previous simulations of Martell et al. (2009, 2010); Park et al. (2013) suggested that the increase of the gas fraction or the spacing between the micro-features of an SHS increases the slip velocity and DR. However, in these simulations, the air-liquid interface was modeled as a stable flat shear free interface which did not account for the stability of the interface. The simulation of Seo et al. (2015) varied the texture spacing of the SHS which including the interface stability. They showed that the shear free interface becomes unstable for larger texture spacing. Therefore, visualization of the air-layer over an SHS could help to understand the relationship between the gas fraction and the air-layer stability.

References

W. Abu Rowin and S. Ghaemi. Streamwise and spanwise slip over a superhydrophobic surface. *Journal of Fluid Mechanics*, 870:1127–1157, 2019a.

W. Abu Rowin and S. Ghaemi. The effect of reynolds number on turbulence structures over a superhydrophobic surface. *Experiments in Fluids*, 2019b.

W. Abu Rowin, J. Hou, and S. Ghaemi. Inner and outer layer turbulence over a superhydrophobic surface with low roughness level at low reynolds number. *Physics of Fluids*, 29(9):095106, 2017.

W. Abu Rowin, J. Hou, and S. Ghaemi. Turbulent channel flow over riblets with superhydrophobic coating. *Experimental Thermal and Fluid Science*, 94:192–204, 2018.

K. Alamé and K. Mahesh. Wall-bounded flow over a realistically rough superhydrophobic surface. *Journal of Fluid Mechanics*, 873:977–1019, 2019.

E. Aljallis, M. A. Sarshar, R. Datla, V. Sikka, and A. Jone. Streamwise and spanwise turbulence structures over superhydrophobic surfaces. *Journal of Fluid Mechanics*, 25: 025103, 2013.

A. Balasubramanian, A. Miller, and O. Rediniotis. Microstructured hydrophobic skin for hydrodynamic drag reduction. *AIAA journal*, 42(2):411–414, 2004.

D. Bechert, M. Bruse, W. v. Hage, J. T. Van der Hoeven, and G. Hoppe. Experiments on drag-reducing surfaces and their optimization with an adjustable geometry. *Journal of Fluid Mechanics*, 338:59–87, 1997.

P. S. Bernard and J. M. Wallace. *Turbulent flow: analysis, measurement, and prediction*. John Wiley & Sons, 2002.

R. A. Bidkar, L. Leblanc, A. J. Kulkarni, V. Bahadur, S. L. Ceccio, and M. Perlin. Skin-friction drag reduction in the turbulent regime using random-textured hydrophobic surfaces. *Physics of Fluids*, 26(8):085108, 2014.

A. Busse and N. D. Sandham. Influence of an anisotropic slip-length boundary condition on turbulent channel flow. *Physics of Fluids*, 24:055111, 2012.

A. B. D. Cassie and S. Baxter. On the criteria for reverse transition in a two-dimensional boundary layer flow. *Transactions of the Faraday Society*, 1944.

Y. Çencel and J. Cimbala. *Fluid mechanics–fundamentals and applications*. McGraw-Hill Internat. Ed., 2006.

C.-H. Choi, U. Ulmanella, J. Kim, C.-M. Ho, and C.-J. Kim. Effective slip and friction reduction in nanograted superhydrophobic microchannels. *Physics of Fluids*, 18(8):087105, 2006.

H. Choi, W. P. Jeon, and J. Kim. Control of flow over a bluff body. *Annual Review of Fluid Mechanics*, 40:113–139, 2008.

F. H. Clauser. The turbulent boundary layer. 4:1–51, 1956.

J. M. Coulson, J. F. Richardson, J. R. Backhurst, and J. H. Harker. *Fluid flow, Heat Transfer and Mass Transfer*. Butterworth-Heinemann, 1999.

R. Daniello, N. Waterhouse, and J. Rothstein. Drag reduction in turbulent flows over superhydrophobic surfaces. *Physics of Fluids*, 21(8):085103, 2009.

R. B. Dean. Reynolds number dependence of skin friction and other bulk flow variables in two-dimensional rectangular duct flow. *Journal of Fluids Engineering*, 100(2):215–223, 1978.

D. Dilip, N. K. Jha, R. N. Govardhan, and M. Bobji. Controlling air solubility to maintain "cassie" state for sustained drag reduction. *Colloids and Surfaces A: Physicochemical and Engineering Aspects*, 459:217–224, 2014.

B. R. Elbing, M. Perlin, D. R. Dowling, and S. L. Ceccio. Modification of the mean near-wall velocity profile of a high-reynolds number turbulent boundary layer with the injection of drag-reducing polymer solutions. *Physics of Fluids*, 25(8):085103, 2013.

D. Elger, B. Williams, C. Crowe, and J. Roberson. Engineering fluid mechanics. *Energy*, 2: 03–01, 2013.

F. F. Farshad and T. C. Pesacreta. Coated pipe interior surface roughness as measured by three scanning probe instruments. *Anti-Corrosion Methods and Materials*, 50(1):6–16, 2003.

K. Fukagata, K. Iwamoto, and N. Kasagi. Contribution of reynolds stress distribution to the skin friction in wall-bounded flows. *Physics of Fluids*, 14(11):L73–L76, 2002.

K. Fukagata, N. Kasagi, and P. Koumoutsakos. A theoretical prediction of friction drag reduction in turbulent flow by superhydrophobic surfaces. *Physics of Fluids*, 18(5):051703, 2006.

M. Gad-el Hak. *Flow Control: Passive, Active, and Reactive Flow Management*. Cambridge university press, 2000.

W. K. George. Lectures in turbulence for the 21st century. *Chalmers University of Technology*, 2013.

S. Gesemann, S. Huhn, F. Schanz, R. Geisler, and A. Schröder. From noisy particle tracks to velocity, acceleration and pressure fields using b-splines and penalties. In *18th International Symposiumon the Applications of Laser and Imaging Techniques to Fluid Mechanics*, 2016.

N. Gilbert and L. Kleiser. Turbulence model testing with the aid of direct numerical simulation results. In *8th Symposium on Turbulent Shear Flows*, volume 2, pages 26–1, 1991.

S. Gogte, P. Vorobieff, R. Truesdell, A. Mammoli, F. Van Swol, P. Shah, and C. Brinker. Tomographic particle image velocimetry. *Experiments in Fluids*, 17(5):051701, 2005.

J. W. Gose, K. Golovin, M. Boban, J. M. Mabry, A. Tuteja, M. Perlin, and S. L. Ceccio. Characterization of superhydrophobic surfaces for drag reduction in turbulent flow. *Journal of Fluid Mechanics*, 845:560–580, 2018.

R. Gupta, V. Vaikuntanathan, and D. Sivakumar. Superhydrophobic qualities of an aluminum surface coated with hydrophobic solution neverwet. *Colloids and Surfaces A: Physicochemical and Engineering Aspects 500*, 500:45–53, 2016.

J. Hou, B. Vajdi Hokmabad, and S. Ghaemi. Three-dimensional measurement of turbulent flow over a riblet surface. *Experimental Thermal and Fluid Science*, 85:229–239, 2017.

I. Hughes and T. Hase. *Measurements and their uncertainties: a practical guide to modern error analysis*. Oxford University Press, 2010.

International Trade Administration, 2017. URL `https://www.trade.gov/steel/countries/pdfs/imports-Canada.pdf`. [Online; accessed 4-April-2019].

K. Iwamoto, Y. Suzuki, and N. Kasagi. Reynolds number effect on wall turbulence: toward effective feedback control. *International Journal of Heat and Fluid Flow*, 23(5):678–689, 2002.

T. Jelly, S. Jung, and T. Zaki. Turbulence and skin friction modification in channel flow with streamwise-aligned superhydrophobic surface texture. *Physics of Fluids*, 26(9):095102, 2014.

P. Joseph, C. Cottin-Bizonne, J.-M. Benoit, C. Ybert, C. Journet, P. Tabeling, and L. Bocquet. Slippage of water past superhydrophobic carbon nanotube forests in microchannels. *Physical Review Letters*, 97(15):156104, 2006.

T. Jung, H. Choi, and J. Kim. Effects of the air layer of an idealized superhydrophobic surface on the slip length and skin-friction drag. *Journal of Fluid Mechanics*, 790, 2016.

Y. Jung and B. Bhushan. Biomimetic structures for fluid drag reduction in laminar and turbulent flows. *Journal of Physics: condensed matter*, 22(3):035104, 2009.

C. Kähler, U. Scholz, and J. Ortmanns. Wall-shear-stress and near-wall turbulence measurements up to single pixel resolution by means of long-distance micro-piv. *Experiments in Fluids*, 41(2):327–341, 2006.

C. J. Kähler, S. Scharnowski, and C. Cierpka. On the uncertainty of digital piv and ptv near walls. *Experiments in Fluids*, 52(6):1641–1656, 2012.

J. Kim, P. Moin, and R. Moser. Turbulence statistics in fully developed channel flow at low reynolds number. *Journal of fluid mechanics*, 177:133–166, 1987.

R. Kristoffersen and I. Andersson, H. Direct simulations of low-reynolds-number turbulent flow in a rotating channel. *Journal of Fluid Mechanics*, 256:163–196, 1993.

J. Lee, T. Jelly, and T. Zaki. Effect of reynolds number on turbulent drag reduction by superhydrophobic surface textures. *Flow, Turbulence and Combustion*, 95(2-3):277–300, 2015.

L. Lei, H. Li, J. SHi, and Y. Chen. Diffraction patterns of a water-submerged superhydrophobic grating under pressure. *Langmuir*, 26(5):3666–3669, 2009.

H. Ling. Experimental investigation of friction drag reduction in turbulent boundary layer by super-hydrophobic surfaces (doctoral dissertation). Master's thesis, Johns Hopkins University, July 2017.

H. Ling, Srinivasan, S., K. Golovin, G. McKinley, A. Tuteja, and J. Katz. High-resolution velocity measurement in the inner part of turbulent boundary layers over super-hydrophobic surfaces. *Journal of Fluid Mechanics*, 801:670–703, 2016.

H. Ling, J. Katz, M. Fu, and M. Hultmark. Effect of reynolds number and saturation level on gas diffusion in and out of a superhydrophobic surface. *Physical Review Fluids*, 2(12): 124005, 2017.

C. Liu, Liao, S.C., J. Song, X. Mauk, M.G. abd Li, G. Wu, D. Ge, S. Greenberg, R.M.and Yang, and H. Bau. A high-efficiency superhydrophobic plasma separator. *Lab on a chip*, 16(3):553–560, 2016.

M. B. Martell, J. B. Perot, and J. P. Rothstein. Direct numerical simulations of turbulent flows over superhydrophobic surfaces. *Journal of Fluid Mechanics*, 620:31–41, 2009.

M. B. Martell, J. P. Rothstein, and J. B. Perot. An analysis of superhydrophobic turbulent drag reduction mechanisms using direct numerical simulation. *Physics of Fluids*, 22: 065102, 2010.

C. D. Meinhart, S. T. Wereley, and J. G. Santiago. A PIV algorithm for estimating time-averaged velocity fields. *Journal of Fluids Engineering*, 122(2):285–289, 2000.

T. Min and J. Kim. Effects of hydrophobic surface on skin-friction drag. *Physics of Fluids*, 16:L50–L58, 2004.

C. Navier. Mémoire sur les lois du mouvement des fluides. *Mem. Acad. Sci. Inst. Fr*, 6 (1823):389–416, 1823.

M. Novara, D. Schanz, N. Reuther, C. J. Kähler, and A. Schröder. Lagrangian 3d particle tracking in high-speed flows: Shake-the-box for multi-pulse systems. *Experiments in Fluids*, 57(8):128, 2016.

J. Ou, B. Perot, and J. Rothstein. Laminar drag reduction in microchannels using hydrophobic surfaces. *Physics of Fluids*, 16(12):4635–4643, 2004.

H. Park, H. Park, and J. Kim. A numerical study of the effects of superhydrophobic surface on skin-friction drag in turbulent channel flow. *Physics of Fluids*, 25(11):110815, 2013.

J. Park, A. Derrandji-Aouat, B. Wu, S. Nishio, and E. Jacquin. Uncertainty analysis: particle imaging velocimetry. In *International Towing Tank Conference, Recommended Procedures and Guidelines, Fukuoka, Japan, Sept*, pages 14–20, 2008.

M. Raffel, C. E. Willert, S. T. Wereley, and J. Kompenhans. *Particle Image Velocimetry: A Practical Guide*. Springer, Berlin, Germany, 2007.

A. Rastegari and R. Akhavan. On the mechanism of turbulent drag reduction with superhydrophobic surfaces. *Journal of Fluid Mechanics*, 773, 2015.

A. Rastegari and R. Akhavan. On drag reduction scaling and sustainability bounds of superhydrophobic surfaces in high reynolds number turbulent flows. *Journal of Fluid Mechanics*, 864:327–347, 2019.

D. Reholon and S. Ghaemi. Plastron morphology and drag of a superhydrophobic surface in turbulent regime. *Physical Review Fluids*, 3(10):104003, 2018.

M. Righetti and G. P. Romano. Particle–fluid interactions in a plane near-wall turbulent flow. *Journal of Fluid Mechanics*, 505:93–121, 2004.

J. Rothstein. Slip on superhydrophobic surfaces. *Annual Review of Fluid Mechanics*, 42(1): 89–109, 2010.

M. A. Samaha, H. V. Tafreshi, and M. Gad-el Hak. Influence of flow on longevity of superhydrophobic coatings. *Langmuir*, 28(25):9759–9766, 2012.

F. Scarano. Tomographic piv: principles and practice. *Measurement Science and Technology*, 24(1):012001, 2012.

D. Schanz, S. Gesemann, A. Schröder, B. Wieneke, and M. Novara. Non-uniform optical transfer functions in particle imaging: calibration and application to tomographic reconstruction. *Measurement Science and Technology*, 24(2):024009, 2012.

D. Schanz, S. Gesemann, and A. Schröder. Shake-the-box: Lagrangian particle tracking at high particle image densities. *Experiments in Fluids*, 57(5):70, 2016.

A. Schröder, D. Schanz, R. Geisler, S. Gesemann, and C. Willert. Near-wall turbulence characterization using 4d-ptv shake-the-box. In *11th International Symposium on Particle Image Velocimetry (PIV15)*, 2015.

J. Seo and A. Mani. On the scaling of the slip velocity in turbulent flows over superhydrophobic surfaces. *Physics of Fluids*, 28(2):025110, 2016.

J. Seo and A. Mani. Effect of texture randomization on the slip and interfacial robustness in turbulent flows over superhydrophobic surfaces. *Physical Review Fluids*, 3(4):044601, 2018b.

J. Seo, R. García-Mayoral, and A. Mani. Pressure fluctuations and interfacial robustness in turbulent flows over superhydrophobic surfaces. *Journal of Fluid Mechanics*, 783:448–473, 2015.

J. Seo, R. García-Mayoral, and A. Mani. Turbulent flows over superhydrophobic surfaces: flow-induced capillary waves, and robustness of air–water interfaces. *Journal of Fluid Mechanics*, 835:45–85, 2018a.

S. Srinivasan, J. A. Kleingartner, J. B. Gilbert, R. E. Cohen, A. J. Milne, and G. H. McKinley. Sustainable drag reduction in turbulent taylor-couette flows by depositing sprayable superhydrophobic surfaces. *Physical Review Letters*, 114(1):014501, 2015.

M. Stanislas, L. Perret, and J.-M. Foucaut. Vortical structures in the turbulent boundary layer: a possible route to a universal representation. *Journal of Fluid Mechanics*, 602: 327–382, 2008.

R. Theunissen, F. Scarano, and M. Riethmuller. On improvement of piv image interrogation near stationary interfaces. *Experiments in Fluids*, 45(4):557–572, 2008.

Trading Economics, 2019. URL `https://tradingeconomics.com/canada/imports`. [Online; accessed 4-April-2019].

T. Tsukahara, Y. Seki, H. Kawamura, and D. Tochio. Dns of turbulent channel flow at very low reynolds numbers. In *Turbulence and Shear Flow Phenomena (TSFP) Digital Library Online*. Begel House Inc., 2005.

S. Türk, G. Daschiel, A. Stroh, Y. Hasegawa, and B. Frohnapfel. Turbulent flow over superhydrophobic surfaces with streamwise grooves. *Journal of Fluid Mechanics*, 747: 186–217, 2014.

B. Vajdi Hokmabad and S. Ghaemi. Turbulent flow over wetted and non-wetted superhydrophobic counterparts with random structure. *Physics of Fluids*, 28(1):015112, 2016.

B. Vajdi Hokmabad and S. Ghaemi. Effect of flow and particle-plastron collision on the longevity of superhydrophobicity. *Scientific reports*, 7:41448, 2017.

O. I. Vinogradova. Slippage of water over hydrophobic surfaces. *International journal of mineral processing*, 56(1-4):31–60, 1999.

R. Vinuesa, A. Noorani, A. Lozano-Durán, G. K. E. Khoury, P. Schlatter, P. F. Fischer, and H. M. Nagib. Aspect ratio effects in turbulent duct flows studied through direct numerical simulation. *Journal of Turbulence*, 15(10):677–706, 2014.

G. A. Voth, A. la Porta, A. M. Crawford, J. Alexander, and E. Bodenschatz. Measurement of particle accelerations in fully developed turbulence. *Journal of Fluid Mechanics*, 469: 121–160, 2002.

K. Watanabe, Y. Udagawa, and H. Udagawa. Drag reduction of newtonian fluid in a circular pipe with a highly water-repellent wall. *Journal of Fluid Mechanics*, 381:225–238, 1999.

R. N. Wenzel. Resistance of solid surfaces to wetting by water. *Industrial & Engineering Chemistry*, 28(8):988–994, 1936.

J. Westerweel and F. Scarano. Universal outlier detection for PIV data. *Experiments in Fluids*, 39(6):1096–110, 2005.

C. White, Y. Dubief, and J. Klewicki. Re-examining the logarithmic dependence of the mean velocity distribution in polymer drag reduced wall-bounded flow. *Physics of Fluids*, 24 (2):021701, 2012.

B. Wieneke. Volume self-calibration for 3d particle image velocimetry. *Experiments in Fluids*, 45(4):549–556, 2008.

B. Wieneke. Iterative reconstruction of volumetric particle distribution. *Measurement Science and Technology*, 24(2):024008, 2012.

B. Woolford, J. Prince, D. Maynes, and B. W. Webb. Particle image velocimetry characterization of turbulent channel flow with rib patterned superhydrophobic walls. *Physics of Fluids*, 21(8):085106, 2009a.

B. Woolford, D. Maynes, and B. W. Webb. Liquid flow through microchannels with grooved walls under wetting and superhydrophobic conditions. *Microfluidics and Nanofluidics*, 7 (1):121–135, 2009b.

I. Young, R. Zagers, L. Van Vliet, J. Mullikin, F. Boddeke, and H. Netten. Depth-of-focus in microscopy. In *8th Scandinavian Conference on Image Analysis, Tromso, Norway.* Citeseer, 1993.

T. Young. Iii. an essay on the cohesion of fluids. *Philosophical transactions of the royal society of London*, 95:65–87, 1805.

J. Zhang, H. Tian, Z. Yao, P. Hao, and N. Jiang. Mechanisms of drag reduction of superhydrophobic surfaces in a turbulent boundary layer flow. *Experiments in Fluids*, 56(9): 179, 2015.

Appendices

A Front Panel

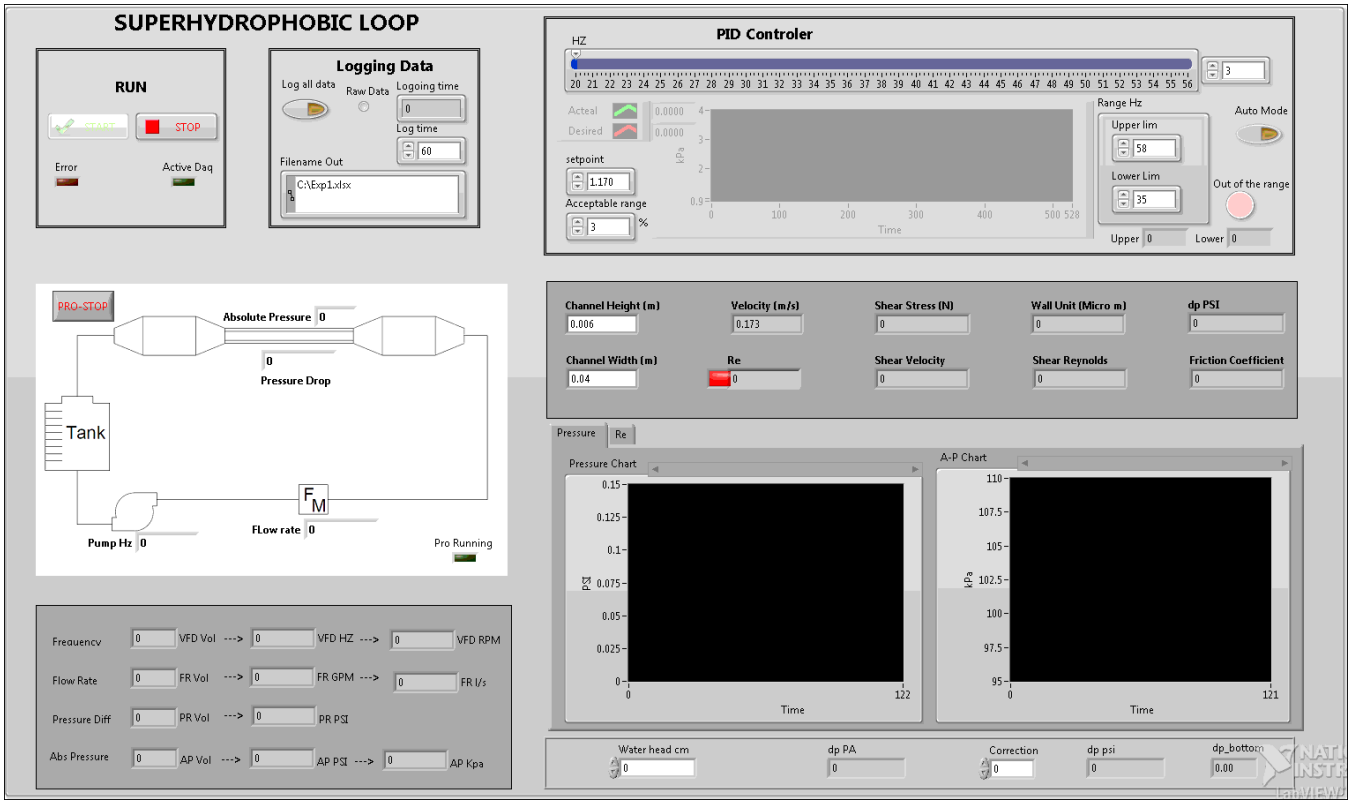

Figure A.1: Front panel for the LabVIEW code

B Block diagram

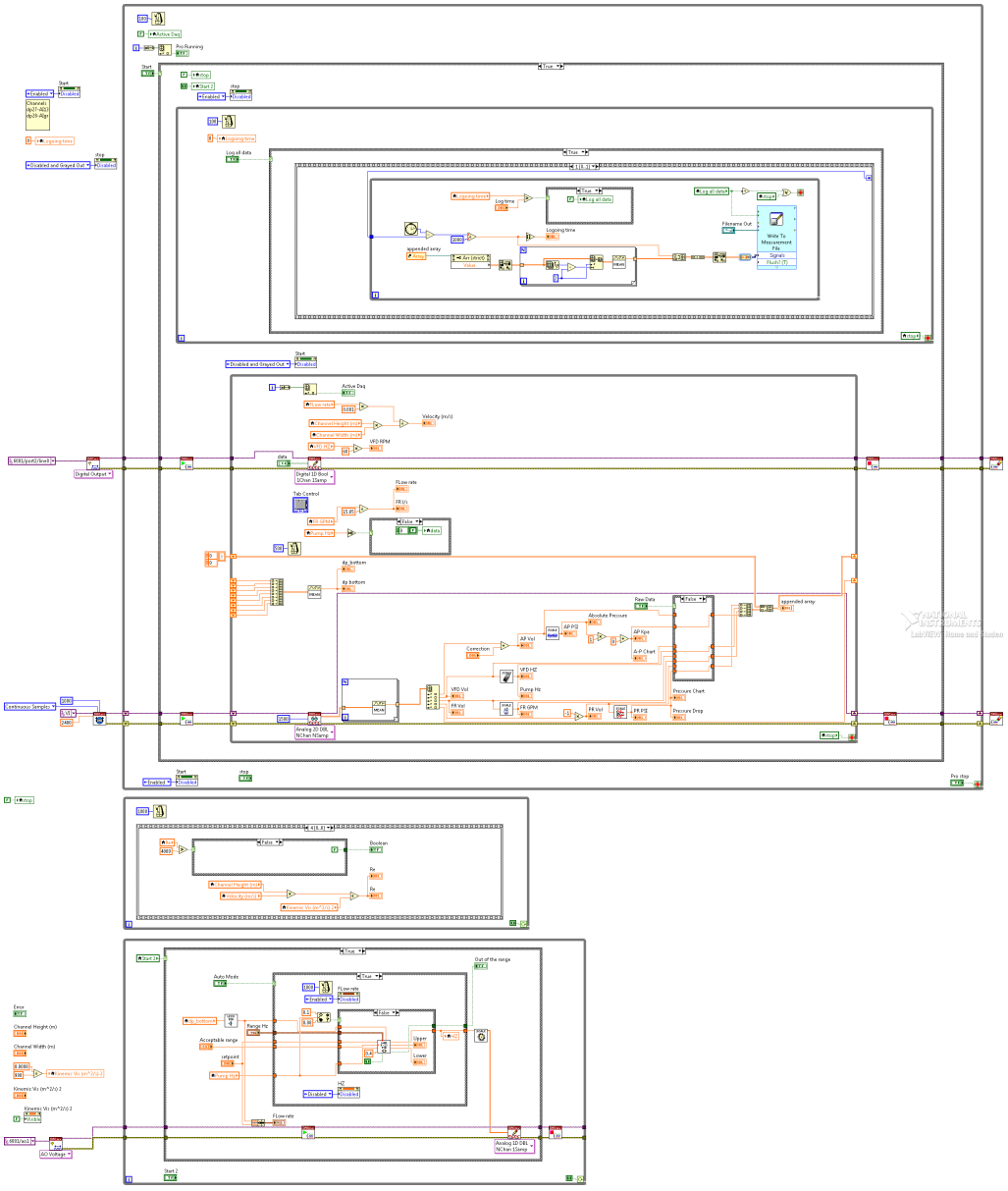

Figure B.2: Block diagram for the LabVIEW code